UNIVERSITY OF COPENHAGEN
FACULTY OF SCIENCE

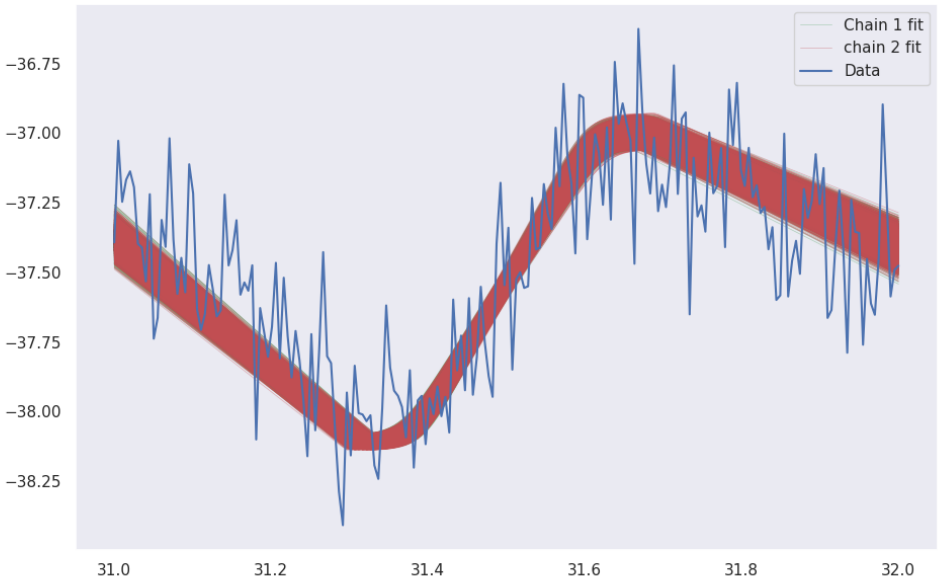

M.Sc. Thesis

Anatomy of Abrupt Climate Change

Dating Dansgaard-Oeschger Events using the Monte Carlo Method

Niels Schøtt Hvidberg

Supervisors: Sune Olander Rasmussen & Aslak Grinsted

Submitted: 30. May, 2023

Name of department:	Niels Bohr Institute, Physics of Ice Climate and Earth
Author:	Niels Schøtt Hvidberg
Title and subtitle	Anatomy of abrupt climate change - dating Dansgaard-Oeschger events using the Monte Carlo method
Keywords:	Monte Carlo inference, time series analysis, paleoclimatic records from ice cores and speleothems, Dansgaard-Oeschger events.
Description:	M.Sc. Thesis in Physics Specialization in Computational Physics 60 ECTS
Supervisors:	Associate Professor Sune Olander Rasmussen Associate Professor Aslak Grinsted

Submitted 30 May 2023

Front page illustration: An example of a Dansgaard-Oeschger transition in surrogate data (blue) together with the proposed lines for the signal (red)

Abstract

In this thesis, the Improved Ramp Fitting Method has been developed, tested, and applied to paleoclimatic records from ice cores and speleothems in order to investigate abrupt Dansgaard-Oeschger transitions during the last glacial period. The method is used to characterize the age and timing of a series of 15 Dansgaard-Oeschger events (27-60 ka BP) in records from the NorthGRIP and NEEM ice cores from Greenland, and from speleothems from the Hulu cave in Southeast China. The study investigate the phasing and anatomy of the Dansgaard-Oeschger events across different proxy records from ice cores ($\delta^{18}O$, Ca^{2+}, Na^{+}, D-excess). A lead of 20 years and 10 years to $\delta^{18}O$ are found for D-excess and Ca^{2+} respectively. The study also compares the timing of Dansgaard-Oeschger events between ice core and speleothem records, and concludes that they happen synchronously or within a lead-lag of 10 years.

Acknowledgements

First of all, I would like to thank my supervisors Sune Olander Rasmussen and Aslak Grinsted for their support and guidance throughout this project. In particular I wish to thank Sune for his inspiration and patience during the process as well as many great discussions along the way. I also wish to thank Aslak for sharing his insights when developing the Monte Carlo model and the noise model.

I wish to thank Jørgen Peder Steffensen and Dorte Dahl Jensen for giving me the opportunity to participate in the 2021 and 2022 field season for the EastGRIP project. It was a fantastic experience that I will never forget!

Thank you to everybody at Physics of Ice, Climate and Earth for many funny discussions and coffee breaks, and to the stratigraphy group for their useful comments during the group meetings.

I wish to thank my friends and family for their support. Finally, I wish to make a special thanks to Josephine, for encouraging me along the way.

Contents

Chapter 1

Introduction

During the last glacial period, the climate was not as stable as it has been during the last ten thousand years in the Holocene period. Instead, it was affected by a series of abrupt changes which drastically changed the climate with up to 16 °C in Greenland (Dansgaard et al., 1993). The abrupt changes were first discovered in stable isotope records obtained from ice cores drilled on the Greenland ice sheet (figure 1.1) (Dansgaard et al., 1982; Dansgaard et al., 1993; Johnsen et al., 1992). The isotope records measured the fractional concentration of ^{18}O referred to as $\delta^{18}O$. The abrupt changes are commonly referred to as Dansgaard-Oeschger events (DO events). The stable isotope records from Greenland reveal more than 25 dramatic events during the last glacial period (Rasmussen et al., 2014). The events are characterised by fluctuations between a cold full-glacial state and a more mild state, and the states vary in duration from a few hundred years to a several thousand years (Rasmussen et al., 2014). Cold and mild periods are referred to as Greenland Stadials (GS) and Greenland Interstadials (GI).

DO events are believed to be a result of oscillations between two quasi-stable states of the climate system (Dansgaard et al., 1993). A recent study suggested that the oscillations are determined by the CO_2 level and the transitions are induced by a stochastic element related to internal climate variability (Vettoretti et al., 2022). However, the precise mechanisms behind these abrupt changes are still being discussed as well as what the global impact on the coupled atmosphere and ocean system of DO events is (Lohmann & Svensson, 2022; Pedro et al., 2022; Pedro et al., 2018; Vettoretti et al., 2022).

Greenlandic Ice cores offer a multitude of parameters to measure, with each parameter representing a proxy for different climate system processes. In all of the measured parameters DO events can be seen. Furthermore, DO events are also recorded in other paleoclimatic archives across the globe, such as marine sediment cores and speleothem cores. Combining archives around the globe offers a spatial coverage of DO events and their impact. It is essential that the records are precisely dated in order to successfully compare the timing of DO events between different records. This is often problematic across archives dated with various methods (Adolphi et al., 2018; Buizert et al., 2015; Corrick et al., 2020). Ultimately, the goal is to map the changes temporally and spatially in the climate system, to understand the mechanisms an causalities.

Ice-core and speleothem records does not share the same dating method. Greenlandic ice cores are dated with annual layer counting, and provide annual to multi-annual resolution (K. K. Andersen et al., 2006; Rasmussen et al., 2006; Sinnl et al., 2022; Svensson et al., 2006). Speleothem records are dated using the ratio of U/Th isotopes, and offers decadal resolution (Cheng et al., 2016; Wang et al., 2001). The specific timing of paleoclimatic records is essential for understanding the causes and mechanisms of DO events as phasing difference between records could suggest phasing differences in the global impact of the events, or could be due to cross-dating uncertainties between the records (Blunier et al., 1998).

Unfortunately dating methods and thus timescales are, as everything else, subject to errors and uncertainties. Ice core records can be synchronized precisely via reference horizons such as volcanic eruptions. In the case of ice cores from Antarctica and Greenland, peaks in methane records can be used as methane is subject to a fast global mixing in the atmosphere (Blunier & Brook, 2001; Buizert et al., 2015).

Both speleothems and ice cores record climate changes in the $\delta^{18}O$ records. The only shared features are the climate transitions associated with the DO events and the glacial cycles. The Ramp Fitting Method (RFM) was developed to offer an unbiased estimate for the age of the transitions, and can then be used to synchronise the two types of records.

The aim of this thesis is to test the robustness of a Markov Chain Monte Carlo (MCMC) inference method that fits a ramp model to data. Familiarity in terms of

strength and weaknesses of the method is key to effectively interpret the results. The motivation to investigate the Ramp Fitting Method, arose from the results of four papers (Buizert et al., 2015; Capron et al., 2021; Corrick et al., 2020; Erhardt et al., 2019). These studies measured the age and properties of DO events during the last glacial. Together they raise three questions:

Question 1: When measuring ice core parameters such as $\delta^{18}O$, Na^{+}, Ca^{2+}, D-excess, does there exist a lead or lag relationship between these parameters with regards to the onset of Dansgaard-Oeschger events?

Question 2: Does there exist a time difference between Dansgaard-Oeschger events measured in ice cores and speleothems? If yes, is this difference related to dating errors of the time series or is the event non-coincidental globally?

Question 3: Can the Ramp Fitting Method, which is used on ice cores, be used on speleothem records given their limitations?

To answer the questions, the need for more thorough testing of the limits of the RFM is required.

This is done here, first by developing the model to include more parameters that better represents the signal. Then the model is investigated in a test environment, testing the method on surrogate data with known properties, to find the accuracy and limitations of ramp fitting. Finally, the method is applied to the data from the four papers, firstly on two ice cores from Greenland, secondly on speleothem data from the Hulu Cave.

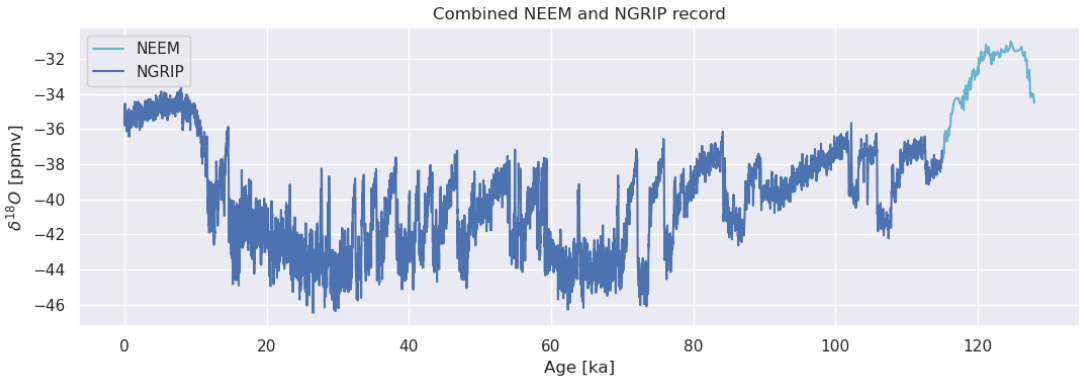

Figure 1.1: The figure shows a combination of the NEEM and NGRIP $\delta^{18}O$ ice core records from Greenland (Andersen et al., 2004; Dahl-Jensen et al., 2013). The Dansgaard-Oeschger events are clearly visible as fast fluctuations during the last Glacial time period. The climate was relatively stable during the Eemian (130 - 115 thousand years BP) and Holocene interglacial time periods (0-11.7 years BP).

Chapter 2

Background

In this chapter, the background for the thesis is described. An introduction of the climate system and the relevant processes is presented, as well as the paleoclimatic archives used in the thesis. Finally, Dansgaard-Oeschger events are introduced together with previous studies and a short explanation of how this study differs.

2.1 The Climate System

The Earth's climate system includes five components: the atmosphere, the ocean, the cryosphere, the biosphere and the lithosphere. In each component, complex processes act and interact. They change dynamically with each other into what we know as the climate (Ruddiman, 2014). Previously, climate was defined as the thirty year mean of precipitation and surface temperature, which is a useful indication of the climate, although a very crude representation. Present day, this definition is expanded to include the variations and extremes which gives a more precise representation of what the climate is and how it changes (Gulev et al., 2021; IPCC, 2021; Ruddiman, 2014).

Climate change occurs as a response to external forcings on the climate system. External forcings are changes in plate tectonics, Earth's orbit, the insolation, and anthropogenic changes. The external forcing influence the current climate system directly and may initiate a response from internal mechanisms in the climate system, that leads to changes over a range of timescales. Feedback mechanisms

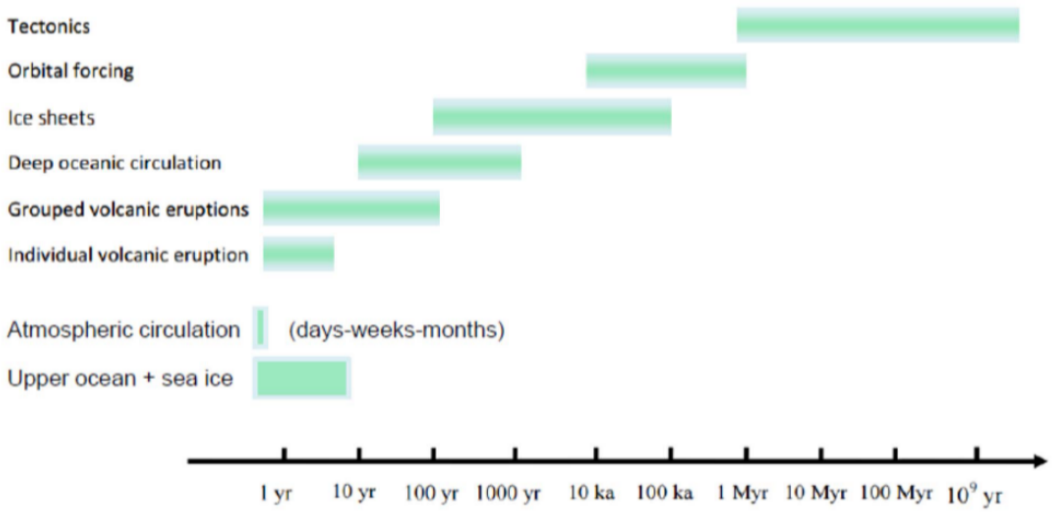

Figure 2.1: The plot shows the typical response times of different components of the climate system. This illustrates at what time scale each component is most dominant (figure from Goosse (2015))

refers to mechanisms that either amplify or counteracts the initial forcing and are said to be positive or negative, respectively (Ruddiman, 2014). They are a key feature of the climate system, and essentially define the stability of the climate. Positive feedback mechanisms creates unstable states, in which a change will propel the climate into a new state. On the contrary, negative feedback mechanisms counteracts this and act to maintain the climate in a stable state.

When the climate system responds to a forcing, not all components will respond equally fast. The different mechanisms may vary in response time, or feedback mechanisms may slow down or speed up the response. Consequently this means, when working with climate data, that the timescale at which you operate will define what mechanisms are relevant. The atmosphere is a very dynamic system which can change on a daily basis. Compared to the cycles of orbital forcing, which acts on tens to hundred thousands of years or changes in the deep ocean circulation which changes over a range of decades to millennia, the atmospheric circulation can change in less than a year, which is a much faster time scale (see figure 2.1).

Climate change can also originate from internal variations within the climate sys-

tem. This type of change is the result of natural variability and feedbacks between components of the climate system. The climate in the North Atlantic is mainly controlled by the Gulf stream and its northern extension, the North Atlantic Current. These two ocean currents transport warm waters from low latitudes to the North Atlantic region. As the water reaches the Arctic ocean southeast of Greenland the water density increases due to cooling and increased salinity from sea ice formation, and sinks to the bottom and flows back towards Antarctica as cold deep water. These currents together are called the Atlantic Meridional Overturning Circulation (AMOC) and constitutes the northern part of the Thermohaline Circulation which is an important part of the global meridional heat transport (Ruddiman, 2014). Several numerical and observational studies of the AMOC suggests three possible stable modes for the system. A warm mode resembling the current state in the Holocene period and GI, a cold mode related to a weakening of the AMOC which is associated with GS, and a shutdown where the North Atlantic circulation is disrupted (Boers, 2021; Dima et al., 2022; Hawkins et al., 2011; Rahmstorf, 2002). The third state for AMOC where it shuts down is believed to be associated with Heinrich events. During Heinrich events, the Laurentide ice cap is believed to collapse resulting in extreme amounts of added fresh water in the North Atlantic (Bond et al., 1992).

If temperatures continue to rise, it would lead to increased freshwater fluxes from the Greenland ice sheet into surface waters from the Arctic ocean. This would affect the salinity of the surface waters, and could reduce the AMOC and eventually push it towards a tipping point. Passing the tipping point would change the current mode, further weakening the circulation, or in extreme cases, shutting it down (Boers, 2021). A change of this magnitude would abruptly and drastically change the climate around the North Atlantic region. Recent studies suggests that the AMOC is currently weakening (Boers, 2021), which could suggest that the climate is moving towards such a tipping point.

2.2 Paleoclimatic Records

The climate leaves a footprint in nature, which can be stored for million of years. The information of previous temperature, atmosphere, sea level, etc. are sealed

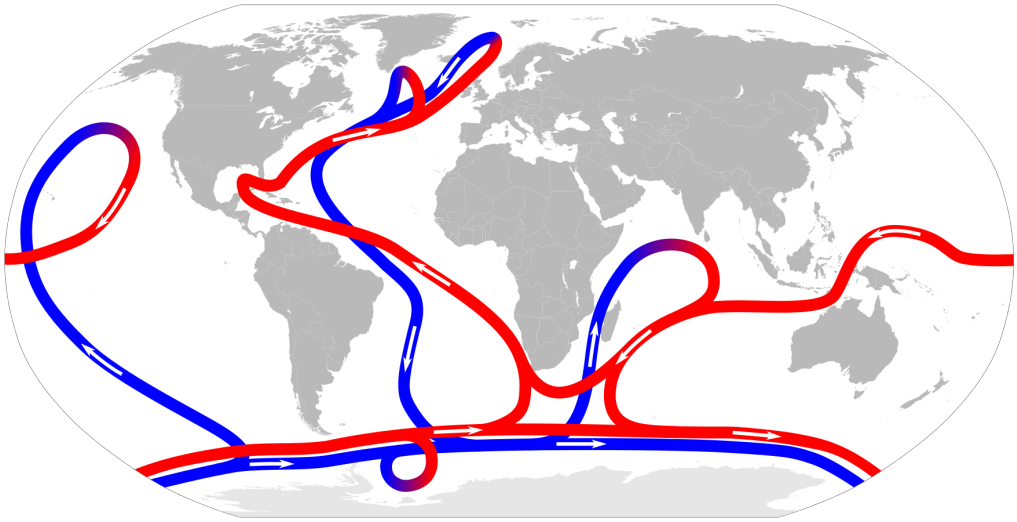

Figure 2.2: The figure shows a graphical representation of the thermohaline circulation. The blue lines represents bottom currents, whereas the red lines represents surface currents (figure from https://encounteredu.com)

in nature in paleoclimatic archives. The most commonly known climate archive is trees. Trees contains information in the tree rings which together with their width, shows a representation of the past climate. Similarly several other archives hold information about the past, such as ice cores, corals, speleothems, sea-floor sediments, etc. A climate proxy refers to a physical property that indirectly represents the climate. This is contrast to air bubbles in ice cores that, when measured, is a direct measurement of the past atmosphere. For climate proxies, further knowledge of the deposition process is needed to interpret the measured parameter. This means, that proxies from climate archives has to both be well understood, as well as precisely measured before they can be used as a climate proxy to infer the past climate.

2.2.1 Greenland Ice Core Records

The Greenland ice sheets contains information of the climate throughout the last glacial cycle (approximately 130 kyrs ago) (Andersen et al., 2004; Dahl-Jensen et al., 2013). Due to high evaporation of water vapor at low latitudes and the general atmospheric circulation, water vapor is transported poleward towards Greenland.

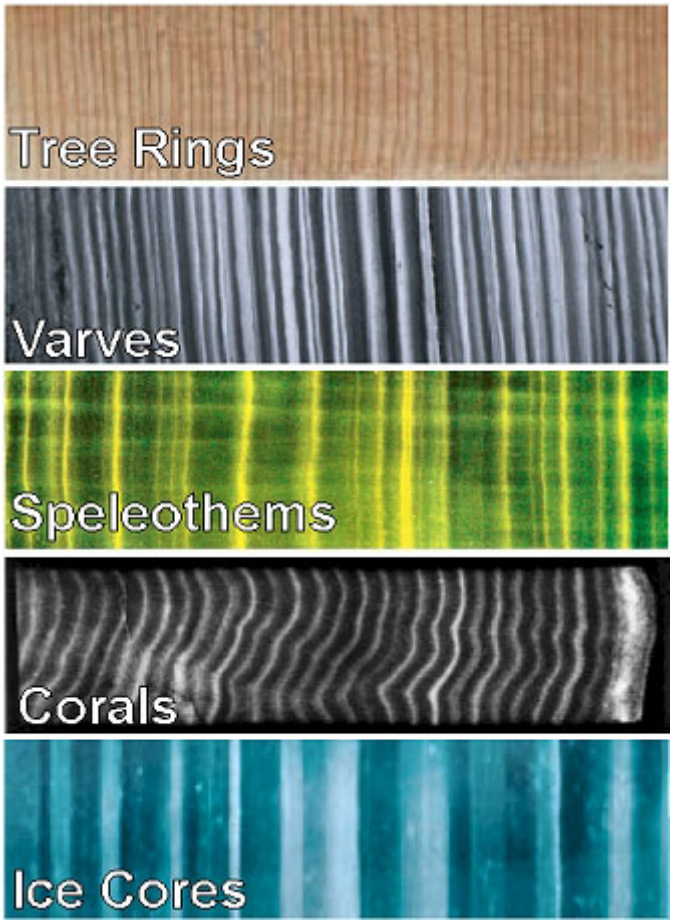

Figure 2.3: The plot shows different paleoclimatic archives, here tree rings, ice cores, speleothems, varves, corals. In some archives, the creation of one layer follows an annual cycle, which allows for detection of seasonal variations and dating via layer counting. However, for speleothems, one layer can span several years (figure from Schmittner (2021)).

During this transport, water molecules containing heavy isotopes of hydrogen and oxygen, such as $H_2^{18}O$ and $HD^{16}O$, condenses with a higher rate than the lighter water molecules $H_2^{16}O$ due to differences in the water vapor pressure of the two isotopic components. When the snow falls on Greenland, the fraction of $H_2^{18}O$ and HDO isotopes in the snow are then lower than it was initially in the subtropical ocean water where the water vapor originated from (Cuffey & Paterson, 2010). The condensation rate is affected by the temperature, and this creates an annual signal in the stable isotope concentration, thus making the relative concentration of

$H_2^{18}O$ and HDO a proxy for the past temperature. This is traditionally calculated as:

$$\delta = \frac{R - R_{SMOW}}{R_{SMOW}}, \quad R = \frac{[^{18}O]}{[^{16}O]} \text{ or } R = \frac{[D]}{[H]} \tag{2.1}$$

Where R is the relative concentration for a sample, and R_{SMOW} is for standard mean ocean water (SMOW) (Dansgaard, 1964). The δ value can be calculated for both of the heavy isotopes, i.e. $\delta^{18}O$ and δD. The deuterium excess is defined from both delta values as:

$$D\text{-excess} = \delta D - 8\delta^{18}O \tag{2.2}$$

D-excess is a second-order stable water isotope parameter that is sensitive to conditions during evaporation of water from the ocean, and has been used in paleoclimatic research to inform of changes in the moisture source region (Dansgaard, 1964; Rasmussen et al., 2014). Willi Dansgaard was the first scientist to measure the signal in Greenland ice cores, after his initial discovery of this phenomenon in rain water over Denmark (Dansgaard, 1964). In order to use $\delta^{18}O$ concentrations as a proxy for temperature, it is necessary to know the temperature difference to the evaporation source as well as the isotopic composition (Dansgaard, 1964).

In addition to snow, ice cores also contain impurities from various aerosols. In this study two aerosol records will be investigated: The Na^+ record which originates from seasalt ($NaCl$) formed by sea spray and is influenced by sea ice, and the Ca^{2+} records which originates from continental dust ($CaCO_3$) from Asia and is influenced by storminess and atmospheric circulation Erhardt et al., 2019. Both of these records have an annual cycle.

Greenland ice cores are usually drilled vertically on the highest local point on the ice sheet. This ensures minimal impacts of horizontal ice flow, keeping the snow layers in chronological order (figure 2.4). The annual layers form from snowfall at the central surface of an ice sheet. As the snow builds up in the middle, ice flows downward and towards the margins of the ice sheet. When the snow sinks down into the ice, the layers are stretched and thinned by ice flow, and the annual layer thickness decrease over depth 2.4. The figure shows how the layer thickness and ice age changes with depth in a simple model (Cuffey & Paterson, 2010). Towards

the bottom, the age of the ice increase exponentially due to the layer thickness approaching zero.

At the time of writing, the current drill project EastGRIP is located in the North East Greenland Ice Stream (NEGIS) (eastgrip.org). This provides an opportunity to investigate ice stream flow, which in turn will help understand the link between ice mass loss and ocean circulation in the North Atlantic.

To summarize, the climate proxies used in this thesis from ice cores are:

- $\delta^{18}O$: a proxy for temperature.
- λ: annual layer thickness, a proxy for precipitation.
- D-excess: A proxy for the water vapor source conditions.
- Ca^{2+}: A proxy for atmospheric circulation and storminess.
- Na^{+}: A proxy affected by the sea-ice extent.

Ice cores are particularly well dated, due to the seasonal signal, as well as the annual or multi-annual resolution. Many processes and parameters also has a seasonal signal, which is measurable with the high resolutions. Greenlandic ice cores are dated by counting the annual layers in the ice core from multiple records.

Volcanic eruptions create a significant peak in sulphuric acids and sometimes tephra layers can be found. The volcanic layers can be identified as reference horizons between different ice cores, which enables a precise synchronization between the cores (Seierstad et al., 2014). Additionally, the dating is calculated in relation to depth, which means that all tracers measured from the ice share equal age and age uncertainty for the same depth. The shared age-depth relationship together with the high resolution is an important feature of ice core proxies, which provide an excellent basis for multi tracer studies, that is, studying all the ice core parameters in a comparison (Cuffey & Paterson, 2010).

The NEEM and NorthGRIP ice core records used in this thesis are dated according to the the Greenland Ice Core Chronology 2005 (GICC05). GICCO5 was constructed from layer counting in the NorthGRIP ice core from Greenland back

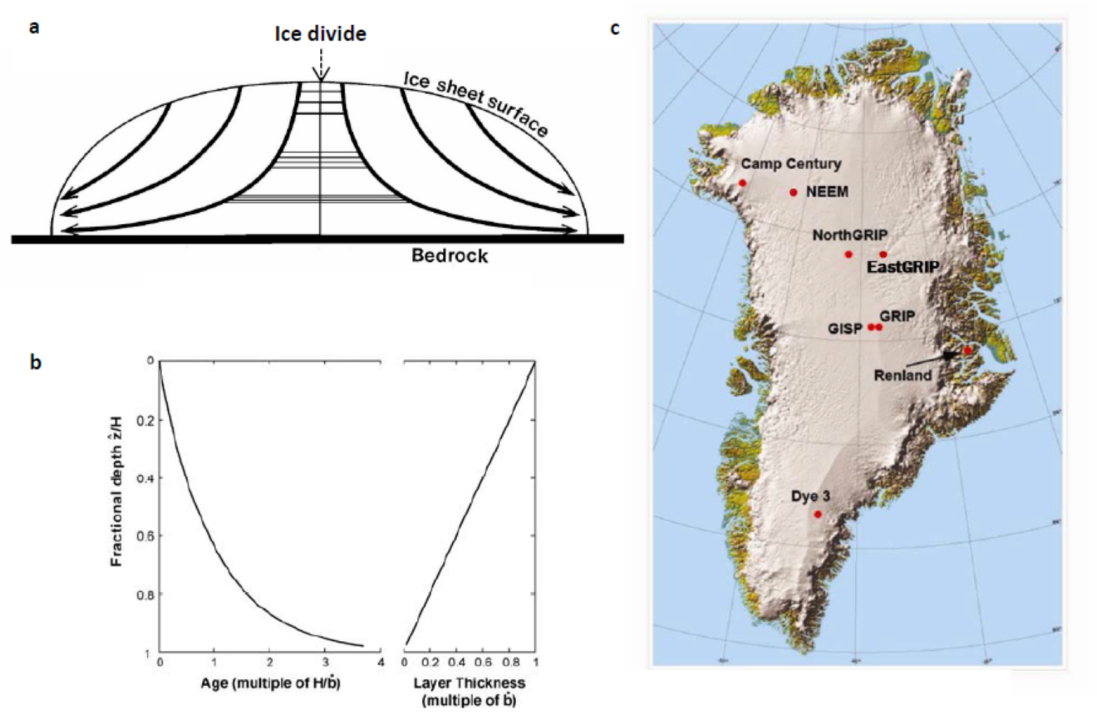

Figure 2.4: **a:** An idealized ice-sheet model (figure adopted from Dansgaard et al., 1969), illustrating how annual layers thin with depth throughout the ice column due to ice flow. **b:** The two graphs shows age and layer thickness with respect to fractional depth according to a simple ice-flow model (the Nye model) (figure from Cuffey and Paterson, 2010). It illustrates together with **a** how the layers are thinned towards the bottom and as a result how the age gradient increases. **c:** This panel shows Greenland and the location of previous deep ice core drill sites. The ongoing ice-core project is located on the NEGIS at the EastGRIP marker.

to 60 thousand years BP K. K. Andersen et al., 2006; Svensson et al., 2008; Svensson et al., 2006, and extended back to 104 thousand years BP by volcanic reference horizons and modelling (Seierstad et al., 2014). The NEEM ice core is dated via matchpoints with the NorthGRIP ice core (Dahl-Jensen et al., 2013). The dating uncertainty arises from cumulative counting uncertainty, commonly referred to as the counting error (K. K. Andersen et al., 2006; Svensson et al., 2008; Svensson et al., 2006). The counting error grows from $\approx$ 100 years to $\approx$ 2500 years during the last glacial (Rasmussen et al., 2014).

2.2.2 Speleothem Records

While ice cores are excellent records in the polar regions, they do not offer much around the tropical or subtropical regions for the last glacial period. Instead, speleothem formations in caves also acts as climate archives. Like ice cores, the formation of speleothems also depends on precipitation as they form from rainwater that drains through the ground and wash out calcite ($CaCO_3$), that essentially becomes speleothems.

As previously mentioned, the isotopic composition of the rainfall depends on local temperature, precipitation, and changes in the vapor source region (Dansgaard, 1964). These changes are reflected in the $\delta^{18}O$ values in the speleothem and many of these records capture the stadial-interstadial oscillations related to DO events (Cheng et al., 2016; Corrick et al., 2020). The climatic interpretation of the $\delta^{18}O$ proxies in speleothems is more complicated than for ice cores and varies depending on the geographical location of the speleothem. For the Asian Summer Monsoon region and South American Monsoon region the $\delta^{18}O$ records are a proxy for precipitation (monsoon strength), and for the Europe-Mediterranean region it is a proxy for temperature (Cheng et al., 2016; Corrick et al., 2020). Figure 2.5 shows the location of speleothem caves that records evidence of DO events.

Due to the geographical variation in speleothem cave locations, speleothem records combined with ice-core records offer global coverage of the temperature and climate system. However, compared to ice-core records, speleothems records often has severely reduced resolution. Furthermore, the complex process of their formation can lead to lag and mixing during seepage to the subsurface cave which can affect the resolution of the records.

Dating of speleothem records can not be done by layer counting as they generally do not possess an annual signal. Instead, the speleothems are dated using radioactive dating methods. ^{230}Th disequilibrium dating is common dating method for paleoclimatic data that usually spans a time period of 600.000 years, which is the maximum limit for the method. The dating method is used on speleothems, and corals among others (Brauer et al., 2014). The radioactive decay series beginning with ^{238}U, omitting the fast reaction, is shown here:

$$^{238}U \rightarrow ^{234}U \rightarrow ^{230}Th \tag{2.3}$$

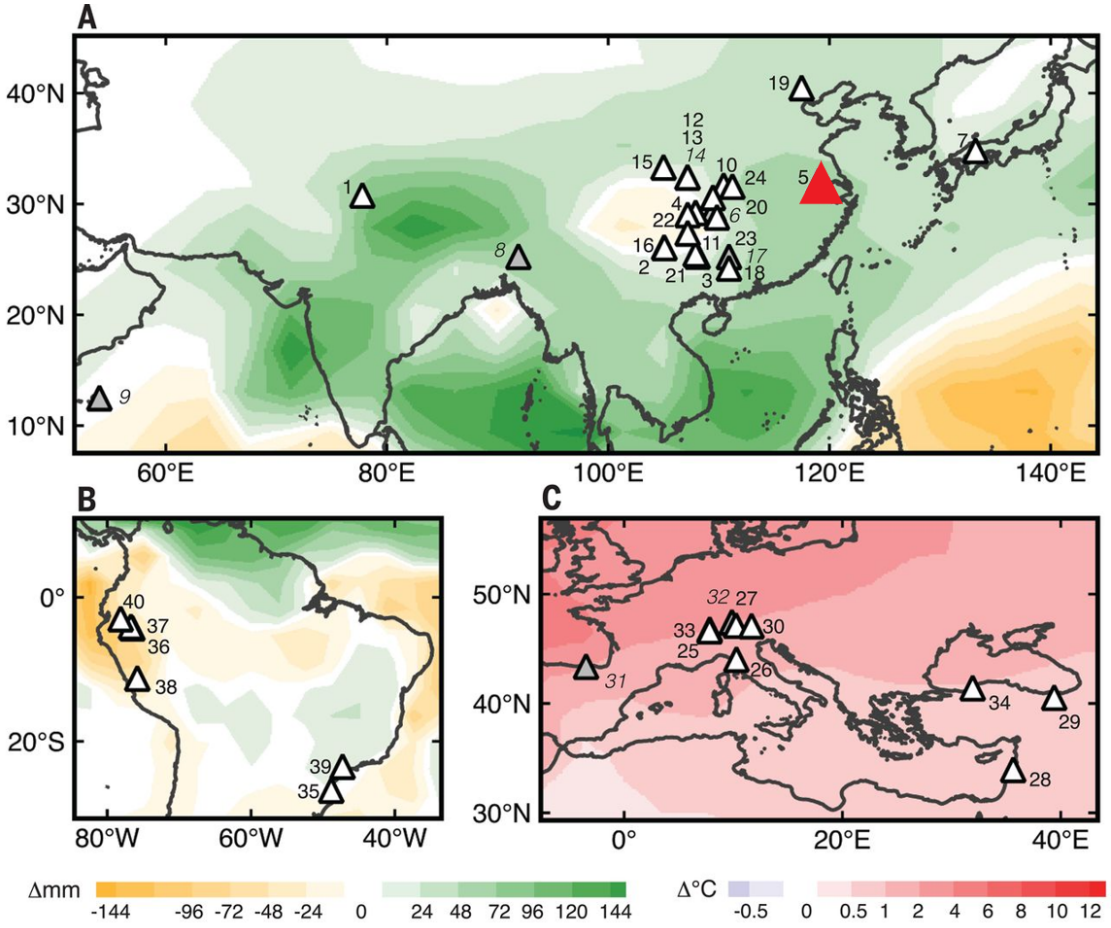

Figure 2.5: This figure is adopted from Corrick et al. (2020) and shows the location of 63 different speleothem records , which all recorded the DO transitions. The red triangle shows the location of the Hulu cave used in this study. The three regions are (A) Asian Summer Monsoon region, (B) South American Monsoon region, (C) Europe-Mediterranean region. The color gradient for each plot show anomalies of annual mean precipitation for (A) and (B) and surface air temperature for (C) between interstadial and stadial states based on climate model experiments of DO events (Corrick et al., 2020).

The dating method compares the concentration of Uran and Thorium, and can then estimate the age based on the decay chain between the two. The method provides independent, accurate and precise chronologies of speleothems. (Brauer et al., 2014). However, samples are not collected continously and this can lead to gaps in the chronology for the record. Between these gaps, the dating relies on

Figure 2.6: The figure on the left shows a picture of a speleothem, cut in half to show the layers. On the right the figure shows a picture of speleothems in a cave. (figure from the INTIMATE project website by Brauer et al. (2014))

modelling of the growth rate for the speleothem (Cheng et al., 2016).

2.3 Dansgaard-Oeschger Events

In ice cores, we can observe periods in the past with more and less variations in the climate. The glacial and interglacial cycles during the last 800,000 years (Jouzel et al., 2007) show that the climate oscillates between glacial and interglacial periods. During the glacials, there is much higher variations compared to the interglacial periods, and we see several events of abrupt climate happening during the glacials (see figure 1.1) (Andersen et al., 2004).

The events are referred to as the already mentioned Dansgaard-Oeschger events after Willi Dansgaard and Hans Oeschger, who first discovered the abrupt events in ice core records from Greenland (Dansgaard et al., 1982). The DO events only occurs during glacial periods and have not been observed in neither the Holocene or in previous interglacial periods (see e.g. figure 1.1). The events are characterized by a sharp transition in to a warm period (Greenland Interstadial or GI), then followed by a cold period (Greenland Stadial or GS) as illustrated on figure 2.3. Usually, the isotope concentration in GIs will be gradually decreasing, until an abrupt transition down into the GS.

The duration of a Greenland stadial or interstadial are within a hundred to several

thousand years (Rasmussen et al., 2014), and the temperature difference is 10-16 degrees (Dansgaard et al., 1993). The transitions are abrupt and spans a few decades. Previously, it was proposed that DO events could be a result of external forcing of the climate system from the sun, and it was believed that DO events were periodic (Rahmstorf, 2002). However, the idea has been rejected (or debated) after ice core time scales have been improved (Svensson et al., 2006).

Another view of DO events, which is gaining support, is that they are originating from internal variations in the climate system (Vettoretti et al., 2022). That is, natural variations reaching a tipping point pushing the climate into a new state. It is unknown what specific processes are causing DO events (Vettoretti et al., 2022). The impact of DO events is observed globally in Greenland, Asia and Antarctica among others (Pedro et al., 2018). A phenomenon called the thermal bipolar seesaw describes a connection between the North Atlantic and the Antarctic region via ocean currents (Stocker & Johnsen, 2003). Studies of Antarctic stable isotope records show cooling coinciding with warm conditions in Greenland and the opposite for warming in Antarctica. The thermal bipolar seesaw was proposed as 'the simplest possible model' to explain the relationship between DO events in Greenland and isotope variations in Antarctic records (Stocker & Johnsen, 2003), but recent studies support the view that DO events are part of an oscillatory climate mode that does not rely on a systematic trigger (Pedro et al., 2022; Vettoretti et al., 2022).

As mentioned, DO events are also reflected in speleothem records. On figure 5.2 an isotope record from Hulu cave is shown, together with the NorthGRIP (NGRIP) isotope record. It is clearly visible that both records contain evidence of DO events. As DO events are visible in the Hulu record, it reveals that the Asian Monsoon and weather system was affected by the events, witch suggests that DO events had global-scale impact (Corrick et al., 2020; Markle et al., 2017).

2.3.1 Anatomy of Dansgaard-Oeschger Events

DO events are diverse, and no two appears completely identical (Capron et al., 2021). The anatomy of DO events refers to the parameters used to describe the initial warming of the event. This is the transition length, the magnitude of the warming for each proxy, and any leads or lags between these. Several studies have

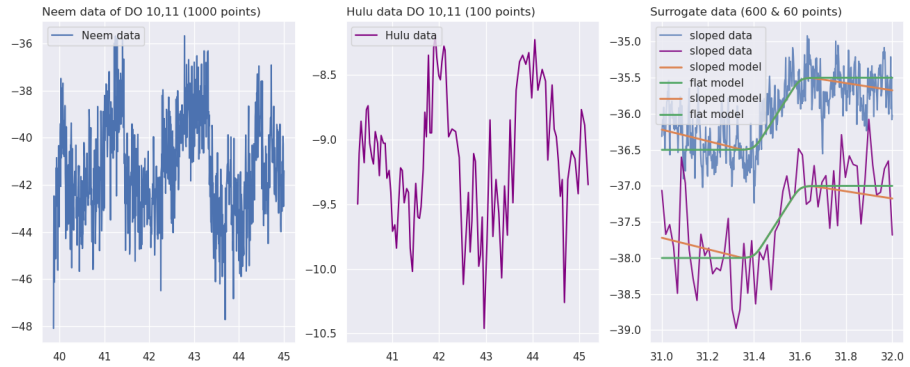

Figure 2.7: The plots shows shows DO event 10 and 11 in the NEEM and Hulu $\delta^{18}O$ record. The last panel shows two surrogate datasets together with the corresponding flat and sloped signal models (see chapter chapter 4). The number of points for each data set is shown above the plots.

been conducted on ice cores, investigating causal relationships and variations in the anatomy of DO events (Adolphi et al., 2018; Capron et al., 2021; Corrick et al., 2020; Erhardt et al., 2019).

The methods used to determine the age of the transitions vary substantially across studies of DO events. Furthermore, the dating methods of speleothems and ice cores display different challenges and uncertainties. Speleothems have a precise absolute dating by U/Th at the dated samples, and ice cores have precise relative dating, but a relatively large error of the absolute age (Buizert et al., 2015) and several studies investigates the difference from the U/Th scale to GICC05 (**buizert**; Adolphi et al., 2018). The discrepancies between the two methods, can then be discussed as differences in response time or dating errors.

In the papers by Erhardt et al. (2019), Adolphi et al. (2018) and Capron et al. (2021), they investigate ice-core data using an "unbiased" objective method building on Bayesian sampling. In the paper by Corrick et al. (2020), a more subjective approach is used due to data quality, and in Buizert et al. (2015) a third method is used. The methods and results of the papers are presented below to illustrate what differences exists.

2.3.2 Multi-tracer Studies on Ice Cores

As already mentioned, ice cores offers a plethora of measurements on gas and isotopes among others. Multi-tracer studies refers to when several records from the same ice core record are studied together, e.g. $\delta^{18}O$ and Na^{+}. Multi-tracer analysis is interesting, because all tracers are measured in parallel, meaning each measurement have the same age, and there is no relative dating uncertainty between the records. Previous studies have used a multi-tracer approach, analyzing the ice-core library. In Capron et al. (2021) and Erhardt et al. (2019), they search for causal relationships between the five records, Ca^{2+}, Na^{+}, λ, $\Delta^{18}O$, and D-excess with respect to their timing of DO events. Erhardt et al. (2019) and Capron et al. (2021) use records from the two deep ice cores from NorthGRIP and NEEM. Both ice cores originates from Greenland.

The paper by Erhardt et al. (2019) argues that all DO events are realisations of the same process or mechanism. Because of this, when calculating the lead and lag relationship between the different tracers, the time difference is obtained from a combination of the statistical distribution across all the DO events for each individual tracer. The resulting conclusion is that on average, the local accumulation and terrestrial dust aerosol concentrations has a lead of about one decade compared to sea-salt aerosol concentrations and local temperature. This suggests that the DO events impacted the Asian monsoon system as well as the moisture transportation to Greenland, while AMOC simultaneously changed to its strong state. If this is true, it might prove that a collapse in the sea-ice cover was not the initial trigger of the DO warming.

The method used in this thesis are based on the method used in Erhardt et al. (2019) - a Bayesian inference of a ramp model assuming a linear transition between two constant levels. The model in Erhardt et al. (2019) was programmed in python. The sampler was run for 60 000 iterations with 60 different ensembles and a posterior of 6000 samples.

The paper by Capron et al. (2021) states two goals, the first being investigating the geographical representativeness of an ice-core record, searching for differences in the timings of DO event transitions between the NGRIP and NEEM ice cores. The second goal is to compare the results from the ice core analysis with simulations

from the Community Climate System Model version 4 (CCSM4) to further discuss which mechanisms are involved in DO events.

Capron et al. (2021) finds high correlations between the anatomy of DO events across the two cores, and that the different DO events has a different anatomy. They argue that the observed transitions could be different realizations of the same underlying processes meaning the different anatomy between DO events might then stem from internal climate variability. This imposes a new problematic that if any sequence exists in the onsets of the different tracers, it itself would be sensitive to internal climatic variability. However, the lack of a unique sequence in the tracers might also suggests that the different anatomy of DO events stems from different external forcings or different expressions of unforced internal oscillations. Examples of these could be fluctuations in salinity or stochastic atmospheric instability, respectively. Nevertheless, the observed abrupt climate change, for both alternatives, features large variations in sea-ice, atmospheric circulation, and temperature anomalies.

The method used in Capron et al. (2021) is essentially the same method as the one used in Erhardt et al. (2019), but in a different implementation. However, the priors vary slightly, in particular for τ. The sampler is written in MATLAB and draw 10^6 samples over an ensemble of 3 with a posterior of 7×10^4.

2.3.3 Synchronization between Ice Cores and Speleothems

Ice cores are dated via layer counting following the GICC05 timescale (K. K. Andersen et al., 2006; Svensson et al., 2008; Svensson et al., 2006)) while speleothems records are dated via radioactive dating with the U/Th method (Brauer et al., 2014; Cheng et al., 2016). Several studies have reported a difference in the calculated ages in ice cores and speleothems, e.g. Adolphi et al. (2018) and Buizert et al. (2015). This poses a new problem of whether differences in the timing of DO events are real or due to issues with the timescales, which can also be investigated using the RFM.

The paper by Adolphi et al. (2018) attempts to account for the dating error between GICC05 and the U/Th chronology using cosmogenic radionuclides and link-

ing them between speleothems and ice cores. The paper reports a time difference of 118 to 549 years between the two timescales calculated as $U/Th - GICC05$ during the period 45 000 to 15 000 years B.P. After correcting for this error, the average time difference between the speleothem records and NGRIP is found to be within 1σ uncertainty of the age (Adolphi et al., 2018), for all but one record. Thus, the differences are not large enough to reject the hypothesis of synchronous DO events in Greenland and low latitude speleothem records.

The paper use the exact same method as in Erhardt et al. (2019) on both the ice core data and speleothem data. The paper analyse transitions in selected speleothem records that are measured in high resolution with distinct features.

The paper by Buizert et al. (2015) attempts to match DO events across ice core records from Greenland and Antarctica, and a speleothem record from the Hulu cave. The ice core data is methane (CH_4) records, which mix fast globally making them optimal for synchronization. The paper finds an average age difference between the U/Th timescale and GICC05 of 0.63% meaning that on average that the U/Th scale is $1.0063 \times GICC05$ older than the ice core record. The difference is believed to originate from ice-core annual-layer counting errors.

This paper uses a more subjective method for determining the timing of DO events. Here the midpoint is calculated as:

$$t_{mid} = \left\{ t \mid y(t) = \frac{y_{post} - y_{pre}}{2} \right\} \tag{2.4}$$

with y_{pre} and y_{post} calculated as a 150 and 50 year mean respectively over intervals on the levels just before and after the transition. Some DO events are excluded due to indistinct features or suboptimal data quality.

The paper by Corrick et al. (2020) investigated a collection of speleothem records from three regions, each location representing the European-Mediterranean region, the South American Monsoon and the Asian Monsoon respectively. The ages of DO events in the speleothems are compared to ages in the NGRIP ice core. The paper finds that DO events are recorded synchronous across each region, as well as less than 100 years of lag between the three regions. Based on the results, they reject the scaling difference between GICCO5 and U/Th timescales proposed in Buizert et al., 2015, as well as the time scale correction of up to 549 years proposed

in Adolphi et al., 2018. The paper uses a method similar to the dating method for DO events in ice cores, which is applied in Rasmussen et al., 2014. The age of the DO event is determined following '*the age of the first data point, which exceeds the maximum value recorded in the preceding stadial period*'. For transitions that exhibit a negative ramp, the method instead applies to the minimum value of the preceding stadial period. For cases where the data point position on the speleothem ramp did not match the location in the NGRIP ice core (i.e. onset vs endpoint or similarly), the data point was switched to the apropriate adjacent points. The method classifies as a more subjective method mostly due to the tuning of the age location.

2.4 How this study differs

This study differs from the previous studies in 3 different ways. Firstly and most importantly, an improved model for the abrupt transition has been developed building on the method from Capron et al., 2021. The improved model introduces two new parameters that describes the slope before and after a transition, which better reflect the typical evolution of a DO event. The improved model is programmed in python utilizing the package $PyMC3$ that improves the computational strain and run time of the program. Secondly, the model is tested more thoroughly on surrogate data to see how well it can find known parameters, while testing various setups for model parameters, data resolution and noise amplitude. Finally, this method will be applied identically on two ice cores, as well as the Hulu speleothem core, thereby eliminating any bias associated with a specific method. This will provide a consistent and comparable dating of the abrupt events across different paleoclimatic datasets, improved with a more complex model.

Chapter 3

Data

This chapter presents the data used in this study. This includes the geographical location, the type of paleoclimatic archive, the specific record used in this study and the timescale. The presentation gives a short summary of the interpretation of the records. The timescale includes information about the measuring method, the resolution and the uncertainty.

3.1 NEEM and NGRIP records

3.1.1 NGRIP

Geographical location: The NorthGRIP (NGRIP) ice core was drilled in Northwest Greenland at (75.1 $°N$, 42.3 $°W$), see figure 2.4. The location was chosen in order to find graphically undisturbed ice dating back into the previous interglacial, the Eemian (130-110 kyears BP). However, basal melting at the site had removed the oldest layers, so only the transition from the Eemian into the last glacial period was preserved. Due to the basal melting, the NorthGRIP core had an exceptional high resolution in the glacial period (Andersen et al., 2004).

Source: The ice core is a deep ice core drilled in the interior of the Greenlandic ice sheet, meaning it covers the entire depth at the NorthGRIP drill site of $3,085$ m, reaching a maximum age of $\sim 123,000$ years (Andersen et al., 2004). The stratigraphic framework includes the transition into the Holocene as well as all GIs and GSs back to GS-26 and the start of the Holocene period (Rasmussen et al., 2014).

In this study, only the period from 27,000 to 61,000 years will be studied, which includes DO-3 to DO-17.2.

Records: In this study, the following records from NorthGRIP were used: $\delta^{18}O$ and D-excess (Andersen et al., 2004; Gkinis et al., 2014) and Ca^{2+} (Erhardt et al., 2019). Together these records allow for the investigation of local temperature and precipitation in Greenland, atmospheric circulation and transportation of dust from e.g. the central Asian deserts.

Measuring Method and resolution: The $\delta^{18}O$ parameter is measured via mass spectroscopy on 5 cm (depth) cut samples of the ice core, resulting in a four to seven years resolution in the depth range studied here (Andersen et al., 2004; Gkinis et al., 2014). The aerosol record (Ca^{2+}) are measured via Continuous Flow Analysis (CFA), where the ice is melted, and the meltwater is measured with spectroscopy. With CFA the meltwater liquid is measured continuously across 8 bags (containing 55cmm pieces) or $\sim 4.4\ m$, with simultaneous registration across all aerosol records down to approximately 1-2 cm scale resolution. Depending on the layer thickness this corresponds to a sub-annual to multi-annual resolution (Erhardt et al., 2019).

Dating: The NorthGRIP ice core is dated according to GICCO5 timescale (see subsection 2.2.1). Uncertainties are determined from the maximum counting error (MCE) (K. K. Andersen et al., 2006; Svensson et al., 2008; Svensson et al., 2006).

3.1.2 NEEM

Geographical location: The NEEM ice core was drilled further North in the central North part of the Greenland ice sheet at (77.45 $^{\circ}N$, 51.06 $^{\circ}W$), see figure 2.4. The NEEM ice core was drilled to the bedrock with a length of $2,540\ m$. The location was chosen with the goal of finding ice, covering the entire previous interglacial, the Eemian period. The NEEM ice core did contain Eemian ice, but the stratigraphy was disturbed in the lower layers (Dahl-Jensen et al., 2013).

Source: This ice core is also a deep ice core, spanning the entire depth of the ice sheet at the NEEM drill site. The first $2,206.7\ m$ of the ice core can be matched to the NGRIP GICC05 timescale. The last $\sim 300\ m$ of the ice core is distorted and folded due to non-vanishing ice flow close to the bottom, so the dating was

done by using several ice core records and linking to Antarctic records, by which the Eemian section could be reconstructed (Dahl-Jensen et al., 2013).

Records: In this study, the following records from the NEEM ice core was used: $\Delta^{18}O$ and D-excess (Vasileios et al., 2020), Ca^{2+} and Na^{+} (Erhardt et al., 2019). These records allow for the investigation of local temperature and precipitation in Greenland, sea ice, atmospheric circulation and transportation of dust from the central Asian deserts.

Measuring method and resolution: The $\delta^{18}O$ and D-excess parameters are measured on the NEEM ice core covering the period 8 - 129 kyears b2k. The depth resolution of the record is 0.05 m. The analysis has been performed using Cavity Ring Down Spectroscopy with an average precision for the whole record equal to 0.05 and 0.3 ‰ for $\delta^{18}O$ and δD, respectively (Vasileios et al., 2020). The measuring methods for Na^{+} and Ca^{2+} was identical to that of the NGRIP ice core (Erhardt et al., 2019).

Dating: The NEEM ice core is also dated according to the GICCO5 timescale by mathcing reference horizons to the NorthGRIP ice core (Dahl-Jensen et al., 2013). The uncertainties are transferred from the NorthGRIP timescale (see subsection 2.2.1).

3.2 Hulu record

Geographical location: The Hulu speleothem is named after the Hulu cave in Southeast China where it was obtained ($32°30'N$, $119°10'E$), see figure 2.5. The mean annual precipitation and temperature at Hulu Cave are 1015 mm and 15.4 °C. The annual precipitation is mainly from the summer monsoon (80%, June to September) (Wang et al., 2001).

Source: The record originates from a group of five speleothems obtained from stalagmite calcite deposits formed from drip water in the Hulu Cave (Wang et al., 2001). The speleothems were obtained from 35 m depth in Hulu Cave, and one was 35 cm long (Southon et al., 2012; Wang et al., 2001). It is unknown if the length is representative for all the speleothems.

Records: In this study, the $\delta^{18}O$ record was used (Buizert et al., 2015). The record is a proxy for monsoon strength in Southeast China (Wang et al., 2001).

Measuring method and resolution: The $\delta^{18}O$ parameter is measured via mass spectroscopy with a resolution of approximately 130-140 years per samle (Wang et al., 2001).

Dating: The Hulu record is dated using radioactive dating methods based on U/Th dating (see subsection 2.2.2). The U/Th age uncertainty range from $\pm$ 150 years at 10 kyears to $\pm$ 400 years at 60 kyears (Wang et al., 2001). Between measured dates, uncertainties are related to the age modelling and assumptions of stalagmite growth rate (Southon et al., 2012).

Chapter 4

Methods

DO events are modelled as a transition between two stable states. There are several possible functions to choose for the transition. There is a large variety in the transition anatomy, that is the duration of an event and the difference between isotope concentrations in GS and GI. Transitions spanning only a few years exists (Steffensen et al., 2008). For these transitions, the transition duration rivals the resolution of ice cores, which limits information of the details of the transition. The original Ramp Fitting Method assumes a linear transition between states. In ice cores, the signal is subject to smoothing due to diffusion in the ice. For the NGRIP ice core, the diffusion length is $5 - 10cm$ during the last glacial for the isotope records.

This chapter will first introduce Bayesian inference as well as some basic mathematical background. Then the chapter describes the Ramp Fitting Method (RFM) and the Improved Ramp Fitting Method (IRFM) in detail. Finally, the chapter will describe the implementation in Python, with an example of the main code.

4.1 Bayesian Inference

The Ramp Fitting Method developed here is based on the theory of Bayesian inference. Bayesian inference is a branch of probability theory that describes the approximation of uncertainties and probabilities obtained through empirical measurements. The formalism used for this chapter are defined in table 4.1.

Notation	Description
θ	Model parameter(s) to be inferred
t	Input (time)
y	Observed data
$\hat{y}$	True signal (no noise)
$m(t, \theta)$	The model taking input t and θ
p	Auxiliary momentum
π	Canonical distribution
$P(\theta)$	Prior probability of θ
$P(\theta\|y)$	Posterior probability of θ given y
$P(y\|\theta)$	Likelihood of y given θ
$P(y)$	Marginal probability of y

4.1.1 Stochastic Variables

Formulating the ramp fitting model in more general mathematical terms, the data consists of N pairs of (t_i, y_i) with $y = \{y_i\}$ denoting the observed data ($\delta^{18}O$, aerosols, etc.). $t = \{t_i\}$ is then the model input variable (age) and θ is a set of 4 (or 6) model parameters for the prediction model $\hat{y} = m(t, \theta)$. The goal of Bayesian inference is to find a set of model parameters, θ, that best predicts the observed data y. For this study a model can be formulated as:

$$y = \hat{y} + \epsilon = m(t, \theta) + \epsilon \tag{4.1}$$

The model consists of a deterministic part $m(t, \theta) = \hat{y}$ and a stochastic part with the stochastic or random variable ϵ. A stochastic variable is used to describe quantities that behave randomly. Compared to deterministic variables that take a fixed value, stochastic variables are associated with some probability distribution that describes the range of values it can take. Random variables are fundamental for probabilistic modelling and are in these cases often associated with the noise parameter.

For a stochastic variable X_i at time i, it can take a value x_i that is drawn from the distribution of X_i. A stochastic process is then a time series of a stochastic variable. When modelling white or Gaussian noise, each value that is drawn is independent of the previous values and drawn from the same distribution $X_i = X$ for all times. If on the other hand the noise is correlated, then the distribution

for the stochastic value changes with time. The noise ϵ in this case is a stochastic process described by an AR(1) process meaning an auto-regressive process. The general formula for an AR(p) process is written:

$$\epsilon_i = \sum_{k=1}^{p} \phi_k \epsilon_{i-k} + \mu \tag{4.2}$$

Where μ is white noise, p denotes the order of the process, and ϕ_k is the correlation parameters of the AR(p) process and determines how much the preceding points influences the next point. Further details of the error model will be elaborated in section 4.2.

4.1.2 Probability

Stochastic variables and probabilities goes hand in hand as one is used to describe the other. Stochastic variables are defined by a probability distribution that describes how likely it is to get a certain outcome. The outcome of a stochastic variable integrated over all possible outcomes has to sum to one: $\int_{-\inf}^{\inf} p(X = x)dx = 1$. It should be mentioned that this study will only cover continuous probability distributions. The probability to get a specific outcome is written $P(X = x) = P(x)$.

Conditional probabilities refers to when the outcome of one event affects the outcome of another event. It is written as $P(X = x|Y = y)$ and describe what the probability to get x when when the outcome $Y = y$ has happened. Joint probability is a little different and refers to the probability to get both outcomes $X = x$ and $Y = y$ before knowing any of them. It is written $P(X = x, Y = y)$ and can be calculated by multiplying the probabilities together or with the conditional probability:

$$P(X = x, Y = y) = P(X = x) \cdot P(Y = y) \qquad or \tag{4.3}$$

$$P(X = x, Y = y) = P(X = x|Y = y) \cdot P(Y = y) \tag{4.4}$$

$$= P(Y = y|X = x) \cdot P(X = x) \tag{4.5}$$

The last concept that needs to be mentioned is Marginalisation. Marginal probability is calculated by marginalising out one of the two variables in a joint probability,

i.e. marginalising $P(X = x, Y = y)$ for X is done by summing over all possible values of Y:

$$P(X = x) = \sum_{all\ y} P(X = x, Y = y) \tag{4.6}$$

The introduced stochastic variables and probability covers the basics for understanding Bayesian inference. The next step is to understand the main equation Bayes Theorem.

4.1.3 Bayes Theorem

The goal of Bayesian inference is to find a probability distribution for the model parameters given the observed data. This can be done in the classical way by a trial and error approach, in which the set of best fit parameters are found. With the Bayesian approach, the probability distribution of the model parameters are found empirically. Prior knowledge of the model parameters is used to delimit and sample the parameter space. Thereby, any prior knowledge of the model parameters is systematically integrated through prior probability $p(\theta)$. The parameter space is sampled to find all sets of model parameters that fit the observed data which results in an empirically determined posterior probability distribution $P(\theta|y)$ for the model. This set of probability distributions are the result of the analysis.

Bayes Theorem describes how the probability distribution is updated with each new guess of model parameters. The equation is found from combining equation (4.4) and (4.5), and inserting the variables from the model (4.1) Bayes Theorem is written as:

$$P(\theta|y) = \frac{P(y|\theta)}{P(y)} \cdot P(\theta) \tag{4.7}$$

This equation is a fundamental part of the Monte Carlo method and machine learning and is a mathematical analogy to how learning and knowledge is obtained. The different components of the theorem represents probabilities and likelihood for the data and parameters.

Prior probability $p(\theta)$ The prior probability or just prior is the initial guess for a distribution for the model parameters. In Bayesian inference, the prior is

used to define where to search for θ in the parameter space. The wider the prior is, the more general the search for the optimal set of model parameters can be. However, if the prior is very narrow the opposite is true and it can take longer to converge. The prior should then be balanced between generality and effectiveness.

Likelihood $P(y|\theta)$ The likelihood tells how likely it is to observe the data y for a specific set of model parameters θ and it can be used as an evaluation of the model parameters. The likelihood is not a probability distribution and therefore it does not follow a normalization of 1. In terms of equation 4.7, The likelihood is high when the observed data y is close to the model $m(t, theta)$ with the proposed set of model parameters θ.

Marginal likelihood $P(y)$ The marginal probability or likelihood act as a normalization that makes sure the posterior distribution $p(\theta|y)$ is a properly normalized probability density. It is calculated from marginalising out θ from the joint probability $P(y) = \int_\theta P(y, \theta)d\theta = \int_\theta P(y|\theta)P(\theta)d\theta$. The last form of the marginal likelihood can be recognised as the integral over the Likelihood and the Prior multiplied. The marginal likelihood is often very difficult to calculate for high dimensional problems, or the integral is impossible to calculate and must be approximated or disregarded in some other way.

Posterior probability $p(\theta|y)$ The posterior probability combines the knowledge prior to any observations with the knowledge gained from testing. The posterior, for short, is the final goal in Bayesian inference and describes a probability distribution for the parameters θ based on the initial guess or prior knowledge ($P(\theta)$ and the observed data ($P(y|\theta)$). In Bayesian inference Bayes theorem has to be applied several times in order to calculate the final posterior distribution.

For some cases of prior and likelihood, the posterior distribution will be the same as the prior. These cases are referred to as conjugate prior-likelihood pairs. However, in the case for this model, the many priors vary a lot between each model parameter resulting in a complex posterior distribution with a non-conjugate prior-likelihood pair. Although conjugate priors are easier to work with and offer analytical solutions, with the current mathematical and computational resources available, the choice of prior should rather represent a modelling perspective (physical or logical) instead of mathematical convenience (Rogers, 2017).

In Bayesian inference, the model parameters are treated as random variables with associated probability distributions. A set of values are drawn from their respective prior distributions and rejected or accepted depending on the likelihood. If the values are rejected with too low a likelihood a new set of values for *theta* are drawn. If the drawn values are accepted, the resulting posterior becomes the new updated prior and the sampling continues.

4.1.4 MCMC Sampling

The Monte Carlo method covers a broad group of random sampling methods and have many uses in physics and mathematics. The Monte Carlo Method uses randomly drawn samples to estimate numerical results. Usually the basic Monte Carlo sampling method uses a subset of possible outcomes to calculate an estimate of the desired numerical value. There exists many different versions of the Monte Carlo Method that varies in simplicity and effectiveness. The Monte Carlo method used for Bayesian Inference is typically a Markov Chain Monte Carlo (MCMC) method.

Markov chains refers to a state model where the probability for the "next" state is only dependant on the previous state. As mentioned before, the Monte Carlo method uses random sampling to infer or approximate a result. With Markov Chain Monte Carlo theory, instead the probability distribution for each value is dependant on the previous drawn value, instead of being a stationary distribution.

Figure 4.1 illustrates a simple state model of 5 possible states. The black token represents the current state. Assume that the token has to jump to one of the adjacent states with probaility p and $p - 1$. The probability to be in one of the five states at any step would only depend on the current position of the token as the two adjacent states would have probability p and $p - 1$ and all other states would be impossible outcomes resulting in probability zero. As the probability only depends on the previous position this system is an example of a Markov Chain or a Markovian system. This system provides a useful analogy for the Markov Chain Monte Carlo Method, which is similar to a random walk.

An example of a random walk simulation, is where each value is drawn from a normal distribution with constant σ and mean value equal to the previous position. The sampled points are thus also prone to auto correlation as each step will be

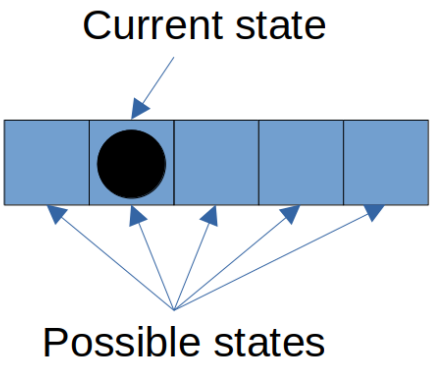

Figure 4.1: This figure illustrates a simple state model of 5 possible states. The black token represents the current state. Assuming the token can only move to adjacent states with probability p and $p-1$, this system exhibits Markovian properties.

near the previous position and the posterior should therefore only contain i.e. every fifth iteration. Compared to white noise each position has no correlation with the previous position and will be drawn randomly.

A random walk simulation and a sampling from a stationary normal distribution will both continue to have an expected value of the the initial position if run infinitely. In Bayesian inference, the probability distributions are constantly updated changing the properties of the distribution until a steady state is reached.

Metropolis-Hastings Markov-Chain Monte Carlo models follows a random walk to draw samples and walk through the parameter space of θ. For each sample drawn the likelihood is evaluated in order to decide whether or not to discard the value. If the value is accepted the probability densities are updated to be centered around the current value. The variance of the distribution can however also be updated depending on the likelihood. That is if there is a high probability density for the currently sampled parameters, small steps should be taken. If the opposite is true larger steps should be taken in order to more efficiently search the parameter space. Usually Monte Carlo samplers are trying to tune sampling parameters such as the step size to have an acceptance rate of $\approx 60-80\%$ of the proposed samples.

A random-walk search is easy to code and works well for low dimensional problems. However, in this case the model parameters θ is 8 dimensional. Then algorithms

such as Metropolis-Hastings functions badly with very slow convergence rates. Instead the more advanced Hamiltonian Monte Carlo model works better.

4.1.5 HMC sampling

Hamiltonian Monte Carlo (HMC) sampling is a special case of MCMC. HMC is a more efficient sampling method compared to random walk sampling as it uses gradient evaluation of the posterior together with Hamiltonian Mechanics Betancourt, 2017. In HMC the problem changes from a sampling problem to be a modelling problem. Recall that the goal is to sample from the posterior probability $P(\theta|y)$ given some data $y = \{y_i\}$. To do this in HMC, the number of model parameters are doubled by introducing a momentum variable for each parameter:

$$\theta_n \rightarrow (\theta_n, p_n) \tag{4.8}$$

Here $\theta = \{\theta_n\}$ is a vector of the model parameters and $p = \{p_n\}$ is the new auxiliary momentum parameters (Betancourt, 2017). The prior distribution now becomes a joint distribution between the momentum and the true model parameters called the canonical probability density π:

$$\pi(\theta, p) = \pi(p|\theta)\pi(\theta) \tag{4.9}$$

This makes sure that marginalising out the momentum variable p brings back the prior distribution $\pi(\theta) = \int_p \pi(p|\theta)\pi(\theta)d\theta$. The density π is a probability density but denoted π as to not be confused with the momentum p.

The canonical density $\pi(\theta, p)$ can be written in terms of an invariant Hamiltonian:

$$\pi(\theta, p) = e^{-}H(\theta, p) \tag{4.10}$$

The Hamiltonian can be used to describe the invariant probabilistic structure of the phase space distribution ($\pi(\theta, p)$), as it is independent on the parameterization Betancourt, 2017. Taking the logarithm of the canonical density and utilizing

equation (4.4) gives:

$$H(\theta, p) = -\log \pi(\theta, p) \tag{4.11}$$
$$= -\log \pi(p|\theta) - \log \pi(\theta) \tag{4.12}$$
$$\equiv K(\theta, p) + V(\theta) \tag{4.13}$$

Here K are defined as the kinetic energy and V is the potential energy following the analogy of celestial mechanics. Then from the Hamiltonian equations trajectories are calculated through the posterior distribution, which equates to sampling the posterior:

$$\frac{d\theta}{dt} = +\frac{\partial H}{\partial p} = \frac{\partial K}{\partial p} \tag{4.14}$$
$$\frac{dp}{dt} = -\frac{\partial H}{\partial \theta} = -\frac{\partial K}{\partial \theta} - \frac{\partial V}{\partial \theta} \tag{4.15}$$

In order to fully explore the posterior distribution random momentum p are sampled and integrated over L time steps of size T in the parameter space and then the new position is used as the next sample, and the process starts over. The integration time T, which is equivalent to path length, and the number of integration steps taken L before testing the sampled value, are two sampling parameters that needs to be tuned for the sampling.

The No-U-Turns sampler (NUTS) (Hoffman & Gelman, 2014) is used together with HMC as it eliminates the need to tune L and T. If the steps are too small the sampler will be similar to a random walk with values grouped together. If the steps are too large the steps can trace back looping around the potential. The name "No-U-Turns" also refers to avoiding this behaviour.

Now understanding the Bayesian Inference of Markov-Chain Monte Carlo sampling, the specific model is introduced in detail.

4.2 The Ramp Fitting Model

Having introduced the mathematical background the ramp fitting model used in Capron et al. (2021) and Erhardt et al. (2019) can now be introduced. The model

assumes that the warming of a DO event can be described as a linear transition between two stable states, and uses four parameters to describes this anatomy: y_0 the initial state, Δy the difference between the two states, Δt the length of the transition, and t_0 the initial onset of the transition. While all parameters are relevant, timing the onset of the transition is the key factor to determine any lead-lag relationship between different time series. The model used in Erhardt et al., 2019 is defined as:

$$y_i = \hat{y}_i + \epsilon_i, \quad \text{for } i > 0 \tag{4.16}$$

with y_i being the measured signal, $\hat{y}_i$ is the true underlying true signal without noise, and ϵ_i is a stochastic variable that represents the noise. The model for the true signal $\hat{y}_i$ is formulated as:

$$\hat{y}_i(t_i) = \begin{cases} y_0 & t_i \leq t_0 \\ y_0 + \Delta y \frac{t_i - t_0}{\Delta t} & t_0 < t_i < t_0 + \Delta t \\ y_0 + \Delta y & t_{mid} + \frac{dt}{2} \leq t_i \end{cases} \tag{4.17}$$

with Δt as the duration of the transition, and t_0 being the onset of the transition. y_0 is the initial level of a GS and Δy is the height of the ramp or the change in concentration level. Note that Δy can both be negative and positive depending on the data studied. The noise ϵ_i is modeled as a red-noise or an $AR(1)$ process as described in section subsection 4.1.1. Red-noise is similar to Brownian noise, described by the following equations:

$$p(\epsilon_i|\epsilon_{i-1}, t_i, t_{i-1}, \tau, \sigma) = \mathcal{N}\left(\epsilon_{i-1} \cdot e^{-\delta t_i/\tau}, \sigma_\epsilon^2\right) \quad \textit{and} \tag{4.18}$$

$$p(\epsilon_{i=0}|\sigma^2) = \mathcal{N}(0, \sigma^2) \quad \textit{with} \tag{4.19}$$

$$\sigma_\epsilon^2 = \sigma^2 \cdot \left(1 - e^{-2\delta t_i/\tau}\right) \tag{4.20}$$

$$\delta t_i = t_i - t_{i-1} \tag{4.21}$$

Here, σ is the actual standard deviation of the resulting red-noise, and σ_ϵ is the standard deviation for an underlying white noise. τ is the correlation time of the

system and can be used to calculate the red-noise coefficient $AR1$ which represents the auto-correlation in the system together with δt_i. δt_i is the i'th time step or the resolution of the data set.

Equation 4.18 can be rewritten in terms of the red-noise coefficient:

$$p(\epsilon_i) = (1 - AR1^2) \cdot \mathcal{N}\left(0, \sigma^2\right) + \epsilon_{i-1} \cdot AR1 \qquad with \tag{4.22}$$

$$AR1 = e^{-\delta t_i/\tau} \tag{4.23}$$

This shows how the noise is constructed from an underlying white noise with standard deviation σ. The standard deviation and the mean of the red-noise is scaled so that for last time steps the noise becomes uncorrelated and independent of the previous value. The formula for the red-noise coefficient can be recognised as the Poisson distribution. On figure 4.2 to the left this model is illustrated together with the improved model to the right.

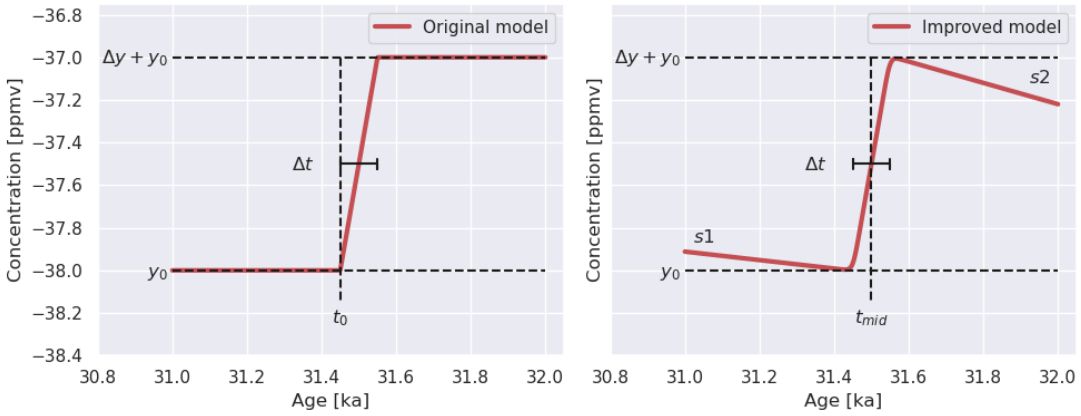

Figure 4.2: **Left:** Shows the original ramp model used in Capron et al., 2021 and Erhardt et al., 2019. **Right:** Shows the improved ramp model developed in this thesis. It features two new parameters $s1$ and $s2$ as well as a redefinition of t_0 to t_{mid}. If $s1 = s2 = 0$, the two models are essentially the same, except for the fact that the improved model is smoothed, making it differentiable.

The prior probabilities used by Erhardt et al. (2019) are shown here:

$$p(t_0) = \mathcal{N}(0.0, 50.0^2) \tag{4.24}$$
$$p(\delta t) = \Gamma(2.0, 0.02) \tag{4.25}$$
$$p(y_0) = 1.0 \tag{4.26}$$
$$p(\tau) = \gamma(2.5, 0.15) \tag{4.27}$$
$$p(\sigma) \propto \frac{1}{\sigma}; \sigma < 10 \tag{4.28}$$

Where $\mathcal{N}$ is the normal distribution and γ is the gamma probability distributions:

$$\mathcal{N}(\mu, \sigma^2) = p(t|\mu, \sigma^2) = \frac{1}{\sigma\sqrt{2\pi}} \exp\left(-\frac{(\mu - t)^2}{2\sigma^2}\right) \tag{4.29}$$
$$\gamma(\alpha, \beta) = p(t|\alpha, \beta) = \frac{\beta^\alpha}{\Gamma(\alpha)} t^{\alpha-1} e^{-\beta t} \tag{4.30}$$

Where $\Gamma(\alpha)$ is the gamma function.

4.3 The Improved Ramp Fitting Model

The model developed in this study are based on the previous model although the function for the true transition as well as priors are different. while being continuous as well , as the software calculates the gradient of the posterior distribution. The Sigmoid function is similar in appearance but have smooth corners compared to the step function. The equation for a Sigmoid is given as:

$$S(t) = \frac{t}{(1 + |t|^p)^{1/p}} \tag{4.31}$$

The exponent p changes how smooth the Sigmoid is. For this study $p = 10$ is used. The equation can then be rewritten in terms of the 4 parameters t_{mid}, Δt, y_0, and Δy:

$$R(t) = \left(y_0 + \frac{\Delta y}{2}\right) + \frac{\frac{\Delta y}{2} \cdot t'}{(1 + t'^{10})^{1/10}}, \quad t' = (t - t_{mid})\frac{2}{\Delta t} \tag{4.32}$$

The model is much more complex but now has the added benefit of being continous. Notice that compared to the previous RFM the timing parameter has changed to

be the midpoint instead of the onset. The addition of slopes was also done utilizing the Sigmoid function. Each slope is its own Sigmoid function, with a duration of 1 year and midpoint at $t_{mid} - \frac{\Delta t}{2} - 0.1 \cdot \Delta t$ and $t_{mid} + \frac{\Delta t}{2} + 0.1 \cdot \Delta t$:

$$S1(t) = \left(s1 - \frac{s1}{2}\right) - \frac{\frac{s1}{2} \cdot t'}{(1 + t'^{10})^{1/10}}, \quad t' = \left(t - t_{mid} + \frac{\Delta t}{2} + 0.1 \cdot \Delta t\right) \cdot 2 \tag{4.33}$$

$$S2(t) = \left(0 + \frac{s2}{2}\right) + \frac{\frac{s2}{2} \cdot t'}{(1 + t'^{10})^{1/10}}, \quad t' = \left(t - t_{mid} - \frac{\Delta t}{2} - 0.1 \cdot \Delta t\right) \cdot 2 \tag{4.34}$$

As the Sigmoid function are smooth the function does not reach the value of y_0 and Δy at $t = t_{mid} \pm \frac{\Delta t}{2}$. If $S1(t)$ and $S2(t)$ are not shifted, the function will therefore not reach the actual fitted levels of y_0 and Δy and would cause a misfit. This is prevented by shifting the midpoint for $S1$ and $S2$ by 10% of the duration Δt.

The noise model is identical to the original RFM and the changes made does not affect it. The prior probabilities now involves calculations based on the input data (t_n, y_n) for $n = 1..N$ and also uses different distributions. The priors have been changed to the following:

$$P(\sigma) = \mathcal{U}(0.1, 5) \tag{4.35}$$

$$P(\tau) = \mathcal{U}(0.001, 0.1) \quad \text{(changed to } \mathcal{H}(0.02^2) \text{ after subsection 5.3.7)} \tag{4.36}$$

$$P(t_{mid}) = \mathcal{U}(t_2, t_{N-1}) \tag{4.37}$$

$$P(\Delta t) = \mathcal{U}(0.001, (t_N - t_0)/3) \tag{4.38}$$

$$P(y_0) = \mathcal{N}(y_1, \text{var}(y)) \tag{4.39}$$

$$P(\Delta y) = \mathcal{N}(y_N - y_1 \text{var}(y)) \tag{4.40}$$

$$P(s1) = \mathcal{N}(0, 6^2) \tag{4.41}$$

$$P(s2) = \mathcal{N}(06^2) \tag{4.42}$$

$$\tag{4.43}$$

where $\mathcal{H}$ is the half-normal distribution, $\mathcal{U}$ is the uniform distribution, and $\mathcal{N}$ is

again the normal distribution:

$$\mathcal{N}(\mu, \sigma^2) = p(t|\mu, \sigma^2) = \frac{1}{\sigma\sqrt{2\pi}} \exp\left(-\frac{(\mu - t)^2}{2\sigma^2}\right) \tag{4.44}$$

$$\mathcal{H}(\sigma^2) = p(t|\sigma^2) = \frac{1}{\sigma\sqrt{2\pi}} \exp\left(-\frac{t^2}{2\sigma^2}\right) \quad for\ t \geq 0 \tag{4.45}$$

$$\mathcal{U}(a, b) = p(t|a, b) = \begin{cases} \frac{1}{b-a} & a \leq t \leq b \\ 0 & x \leq a \vee x \geq b \end{cases} \tag{4.46}$$

The likelihood of the model is defined from the noise model. As such the Likelihood distribution is equal to the probability of stochastic variable ϵ. For a drawn set of parameters θ the residuals res are calculated as:

$$res = y - m(t, \theta) \tag{4.47}$$

and then the likelihood is calculated as the probability that the residuals res are the output from $p(\epsilon_i) = \mathcal{N}\left(\epsilon_{i-1} \cdot e^{-\delta t_i/\tau}, \sigma_\epsilon^2\right)$ (equation (4.18)).

4.3.1 Implementation in PyMC3

The availability of all kinds of packages for programming languages such as python has made it very easy to find effective code for most problems. Probabilistic programming is not excluded and thus the *PyMC3* (J Salvatier, 2016) package is introduced. This package offers a simple yet powerful framework for setting up a Monte Carlo Model and running it. The *PyMC3* package uses c++ based libraries optimizing the code. Figure 4.3 shows how the main function is coded.

The *MCMC_Hammer* function requires three input parameters: A list containing the x-values and y-values for the observed data, the number of tuning steps defining the burn-in period where the parameter space is searched, and the number of posterior samples where the distributions are not updated anymore but just sampled from to get an estimate for the probability density for the optimal parameters. The function also has the option to change the power of the sigmoid, however this study only uses one value $p = 10$. The last input parameter is for switching between the previous model and the improved model.

One iteration of the function takes $\backsim$ 1 minute of run time with 14000 sample draws ($2 \times (6000 + 1000)$ draws). The sampling itself takes about 45 seconds and the last 15 seconds are added from the code being compiled into the underlying c++ code.

The package is installed in a new python environment together with the different package dependencies. The code has been run on Denmark's National Life Science Supercomputing Center, Computerome. The supercomputer have 31,600 CPU cores, with 220 terabytes of memory available, providing an aggregate peak performance in excess of 1,000 TeraFLOPS.

```python
def MCMC_Hammer(time_signal, sampling, tuning, chains=2, p=10, sloped_flat=0):
    """
        Takes a list of time_axis and signal_axis and calculates the best fitting sigmoid.

        The sigmoid model is with slopes and p = 8 default.

        ## Input
        #
        # time_signal: list[ time, signal].
        #
        # sampling: Number of samples drawn from posterior.
        #
        # tuning: Number of tuning steps before sampling posterior.
        #
        # chains: Number of sampling chains.
        #
        # p: The power factor of the sigmoid.
        #
        # sloped_flat: Boolean, choosing sloped or flat model

    """
    # Calculate step-size and Standard deviation
    delta_t = np.abs(time_signal[0][1:]-time_signal[0][:-1])
    SD = np.std(time_signal[1])
        with pm.Model() as model:
            ## Defining priors and model to sample from ##
            # Noise parameters
            sigma = pm.Uniform("sigma", lower=0.1, upper=5)
            tau =  pm.HalfNormal("tau", sigma=0.020)

            # Model parameters
            tmid = pm.Uniform("tmid", lower=time_signal[0][1], upper=time_signal[0][-2])
            dt = pm.Uniform("dt", lower=0.001, upper=(time_signal[0][-1]-time_signal[0][0])/3)
            y0 = pm.Normal("y0", mu=time_signal[1][0], sigma=SD)
            dy = pm.Normal("dy", mu=(time_signal[1][-1]-time_signal[1][0]), sigma=SD)

            ## Sampled Model ##
            if sloped_flat:
                y_model = sigmoid(time_signal[0], [tmid, y0, dt, dy])
            else:
                s1 = pm.Normal("s1", mu=0, sigma=6)
                s2 = pm.Normal("s2", mu=0, sigma=6)
                y_model = sloped_sigmoid(time_signal[0], [tmid, y0, dt, dy, s1, s2])

            ## Calculate the residuals from the sampled model to our data
            res = y_model - time_signal[1]

            ## Calculate likelihood of the residuals, based on sampled noise parameters
            e0 = pm.Normal("e0", mu=0, sigma=sigma, observed=res[0])
            sigma_e = np.sqrt(sigma**2*(1-np.exp(-2*delta_t/tau)))
            Error = pm.Normal("err", mu=res[:-1]*np.exp(-delta_t/tau), sigma=sigma_e, observed=res[1:])

            ## Sample options ##
            idata = pm.sample(sampling, tune=tuning, chains=chains, return_inferencedata=True, progressbar=True)

        return idata
```

Figure 4.3: This figure shows the *PyMC3* code used to program the Monte Carlo Method used in this study. The model is defined within the *with* environment following the approach described by *PyMC3*.

Chapter 5

Model Performance

Before applying the model to real data, it is important to test the models limitations and requirements to the data. The goal is to test how robust the IRFM is when applied to data of various quality in order to enhance the credibility of its results. In this chapter, the model is tested on surrogate data that reflects the complications of the measured paleoclimatic records with a goal to identify when the model fails to be able to determine the location of the transitions with sufficient precision.

Previous studies which have used the model (Capron et al., 2021; Erhardt et al., 2019), are mostly comparing results to archives such as Rasmussen et al. (2014) to discuss the temporal differences in the timing of DO events across various ice core records. In Capron et al. (2021) an analysis of surrogate data from a climate model (CCSM5) which can reproduce DO events is used to further their discussion of lead and lag relationships, and not to test the RFM capabilities.

In order to conduct a proper test of the model it has to be done on data with known characteristics. This study will use surrogate data that replicates the characteristics of ice-core and speleothem data, which allows for testing the model with respect to sample resolution, signal to noise ratio, etc. The next sections will cover experiments that aims to replicate the measured paleoclimatic records, allowing for the perfect environment to test different hypothesis and tune the priors and settings for the IRFM.

First, the sensitivity of the model to the resolution of data is investigated. Then

the following tests are conducted on two set-ups, one with high and low resolution, which reflects typical ice-core and speleothem data properties, respectively.

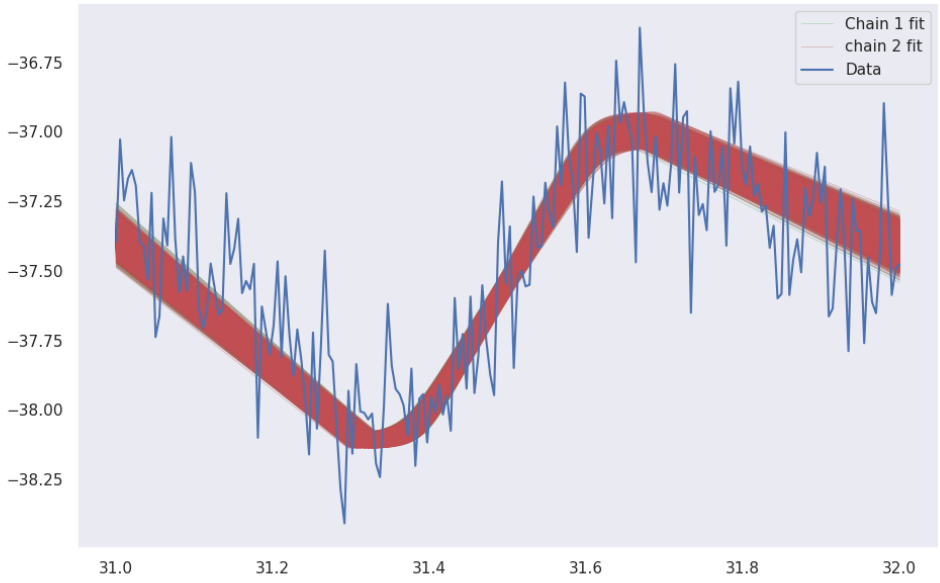

Figure 5.1: The plot shows the posterior solutions that lies within 1σ of the mean posterior solution inferred from an example transition created as surrogate data. This illustrates how the posterior samples can be combined into proposed solutions.

5.1 Surrogate Data

All surrogate data presented are created from the model given in equation (4.16) by first calculating the true model from the four parameters t_{mid}, Δt, y_0 and Δy, then adding the red noise which is constructed with known values of τ and σ. The sample rate is set accordingly to each experiment. In all tests, the surrogate data are constructed from the sloped signal model (equation (4.32)) and the AR1 noise model (equation (4.18)).

The units for the different parameters are omitted on the plots as for the model parameters σ, y_0, Δy, $s1$ and $s2$ the units vary depending on the ice core parameter measured, e.g. $\delta^{18}O$ and Na^{+}. However, for the time related parameters, the units

are the same in all cases, i.e. t_{mid} [kyr], Δt [kyr] and τ [kyr]. Although the unit for the slopes changes, they will always be referred to in rates pr kyr.

When constructing the surrogate data and choosing a resolution, even though it is not a model parameter, the AR1 coefficient $AR1 = e^{-\delta t_i/\tau}$ is dependent on the step size δ_i, meaning the resolution will determine the effective auto-correlation together with τ. All of the surrogate data used in this study will be evenly distributed to have a constant resolution, although the IRFM is not limited by this feature, as when it is applied on the paleoclimatic records, they have varying resolution as shown on figure 5.2. All model parameter values used for the surrogate data

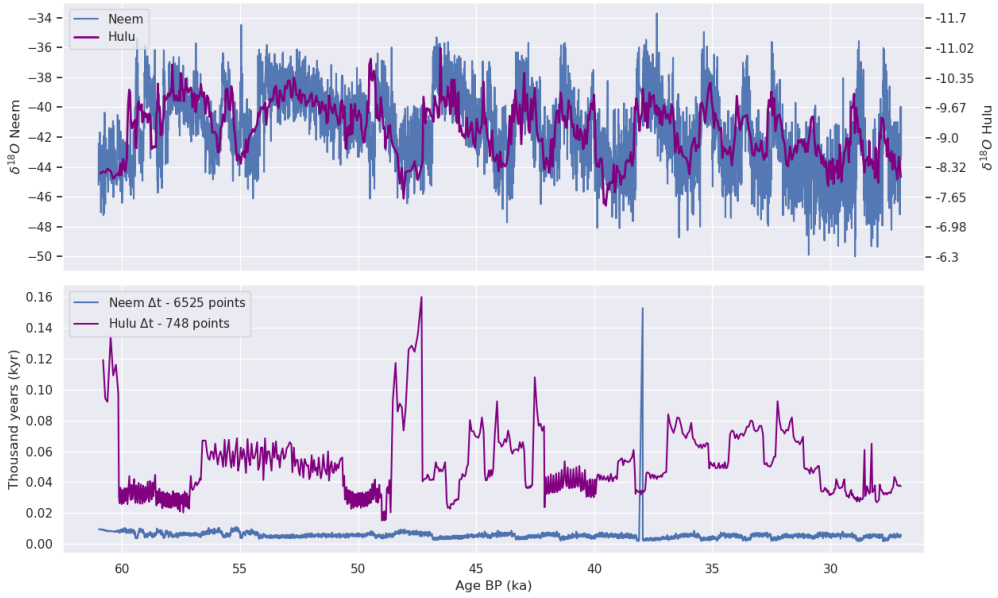

Figure 5.2: The figure shows the two $\delta^{18}O$ records from Hulu and NEEM. The top panel shows the two records. The bottom panel shows the resolution calculated as the step size for each measurement $\Delta t = t_i - t_{i-1}$ (not to be confused with the duration of the transition). There is one outlier in the resolution for NEEM where there is a gap in the record.

5.2 The Error Model

The Monte Carlo algorithm is trying to fit $y_i = \hat{y}_i + \epsilon_i$. Figure 5.3 shows a plot and histogram of two surrogate data sets of 500 points constructed from a constant model ($\hat{y}_i = 0$), with normal white noise (cyan) and correlated red noise (magenta). In this section the signal is assumed to be dimensionless. The noise model parameters are set to be $\tau = 6$ and $\sigma = 1$. As seen from the right pane on figure 5.3, the standard deviation is larger for the red noise data set. This can be explained by the correlation allowing the noise process to travel further from the true signal. When calculating the standard deviation of the red noise, it is found to be 1.75 which is about twice as large as the white noise with a correlation coefficient, $AR1$, that is:

$$Cor(\epsilon_{red}) = AR1 = e^{(-\delta t/\tau)} = e^{(-1/6)} = 0.846 \tag{5.1}$$

This means that about 85% of the previous value is transferred to the next value (for $\delta t = 1$). This amount then decreases or increase as Δt or τ increases.

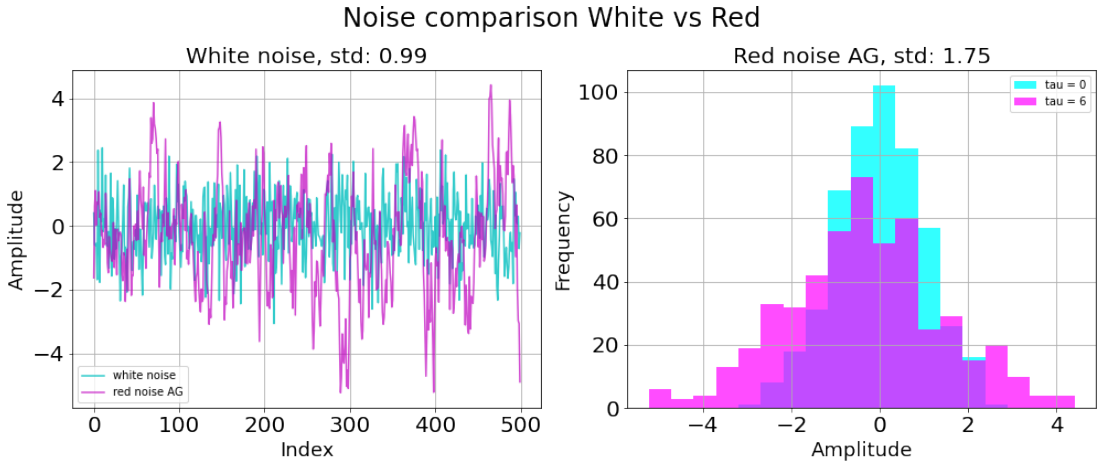

Figure 5.3: The plots shows the difference in white and red-noise with a constant model $Y = 0$. The first plot shows the red and white noise plotted together and the left plot shows a histogram of them which clearly illustrates how the red noise distribution is wider than the white noise distribution.

It is desired to find σ_ϵ, as described in equation (4.20), from the surrogate data as this is the value being fed to the noise model. The standard deviation associated

with the red noise, σ, can be thought of as a scaling of σ_ϵ and is what the model fits. Recall equation (4.20) that describes how to calculate σ_ϵ from σ. It can be rewritten to:

$$\sigma_W = \sigma_R \cdot \sqrt{\left(1 - \exp\left(\frac{-2 \cdot \delta t}{\tau}\right)\right)} = \sigma_R \cdot \sqrt{(1 - AR1^2)} \tag{5.2}$$

Using the values that the red noise in figure 5.3 was constructed from ($\tau = 6$, $\delta t = 1$), it is possible to go from $\sigma = 1.75$ to $\sigma_\epsilon = 0.93$ with equation (5.2). $\sigma = 1.75$ is calculated analytically. In comparison the IRFM is used for a constant model $y_i = 0$ and 4000 tuning and sample draws, the method finds $\sigma = 1.82$ and $\tau = 5.67$. Calculating σ_ϵ with these values gives $\sigma_\epsilon = 0.99$. This yields a difference in the σ_ϵ values analytically and numerically determined, that can be explained by the stochastic nature of the process. Rerunning the code that constructs the surrogate data, a variation can be observed in the standard deviation for the red noise ranging from approximately 1.63 to 2.02 giving a mean around 1.83. In comparison the theoretical value for σ can be calculated using equation (5.2) which gives:

$$\sigma = \sigma_\epsilon \cdot \left(1 - \exp\left(\frac{-2 \cdot \delta t}{\tau}\right)\right)^{-1/2} = 1 \cdot \left(1 - \exp\left(\frac{-2 \cdot 1}{6}\right)\right)^{-1/2} = 1.82 \tag{5.3}$$

The theoretical value for σ is within the range of the experimentally estimated value of σ, and very close to the mean. Table 5.1 shows the result of further tests of how well the method finds σ and τ for various model parameters.

5.3 Tests

The following section contains 6 tests conducted with the IRFM (and RFM) on surrogate data. The tests and their goals will be presented together with concluding remarks of the gained knowledge from each test. For all but one of the tests two chains are used to sample from with a standard of 6000 tuning sample draws and 1000 posterior sample draws. Unless mentioned the surrogate data is constructed from over a time window equivalent to a thousand years, from 31 to

true values		mean sampling estimate	
σ	τ	σ	τ
1	6	1.01	5.80
2	6	1.96	5.09
3	6	3.05	6.08
5	6	4.76	5.65
10	6	10.01	5.44
1	10	0.98	15.25
1	5	0.99	5.94
1	5	1.03	5.31
1	5	0.99	5.72
1	3	1.01	3.17
1	1	1.00	0.97

Table 5.1: The table shows results from runs with noise applied to a constant model $Y = 0$ of size 500, with 4000 tuning draws and 4000 sampling draws.

32, with model parameters: $t_{mid} = 31.5$, $y_0 = -38$, $\Delta t = 0.1$, $\Delta y = 2$, $s1 = -1.2$, $s2 = -1.5$, $\tau = 0.003$, $\sigma = 0.4$ (note that σ here refers to the white noise sigma $\sigma_epsilon$).

5.3.1 Test 1a: Sampling Rate

Figure 5.4 shows the result for test 1. Test 1 wishes to test the model sensitivity to teh data sampling rate. The surrogate data used in test 1 is made with varying numbers of samples, keeping all other values constant. Recall the equation for the AR1 coefficient:

$$AR1 = e^{-\delta t_i/\tau} \tag{5.4}$$

It is important to note that tau, and not the AR1 coefficient, is kept constant. The AR1 coefficient is dependent on the resolution which means with a constant τ the auto correlation between neighbouring points goes down as the resolution goes down, resulting in the noise converging to white noise as the resolution gets more coarse. Each data point on figure 5.4 is an average over 50 realisations of the same process. All the error bars shown is calculated as the mean of one standard deviation (1σ) across the 50 iterations. A general trend for each parameter is that

they converge when the resolution goes up, and all parameters appear to have converged at a sampling rate about 100 or 150 samples/kyr. The same thing can be observed for the errors. τ, σ and Δt does not converge to their true values. Note that the uncertainties for τ reaches negative values.

For τ the mean value does not seem to converge towards the true value, but rather a smaller value. This is problematic when the error bars becomes so tiny, that the true value is not in the 2-3 σ range. This could be a systematic error in the model that the AR1 coefficient converges to white noise when the correlation time τ is smaller than the step size. Thus if all sampled τ equal to or smaller than the step size δt are accepted, this means that the mean value for τ will converge towards $\frac{\delta t}{2}$ as the posterior distribution would be $\mathcal{U}(0.001, \delta t)$.

The σ shown is the white-noise σ, which means it is dependant on τ. Since the two noise parameters are correlated, it is expected that the σ values converge to a mean value above the true value, when τ converges to a mean value below the true value. The 1σ uncertainties for τ are calculated for the entire posterior set and then added and subtracted from the mean value on the plot. This results in the uncertainties reaching negative values. This should be disregarded as τ only can take positive values. The ideal error bars would be asymmetric showing the 95 % and 5 % values for the posterior distribution.

As the uncertainties displayed on the figure is the 1σ standard deviation, the true value for τ is still not inside the 2σ range for the last point with a sample rate of 250 samples/kyr. As mentioned in the investigation of the error model (section 5.2), the IRFM does not necessarily fit the true value of sigma and tau in order to find the best line. In the study by Erhardt et al. (2019) they do not consider the inferred posterior result for σ and τ, but rather treat them as nuisance parameters as they are used to define the likelihood of the model (as mentioned in section 4.3).

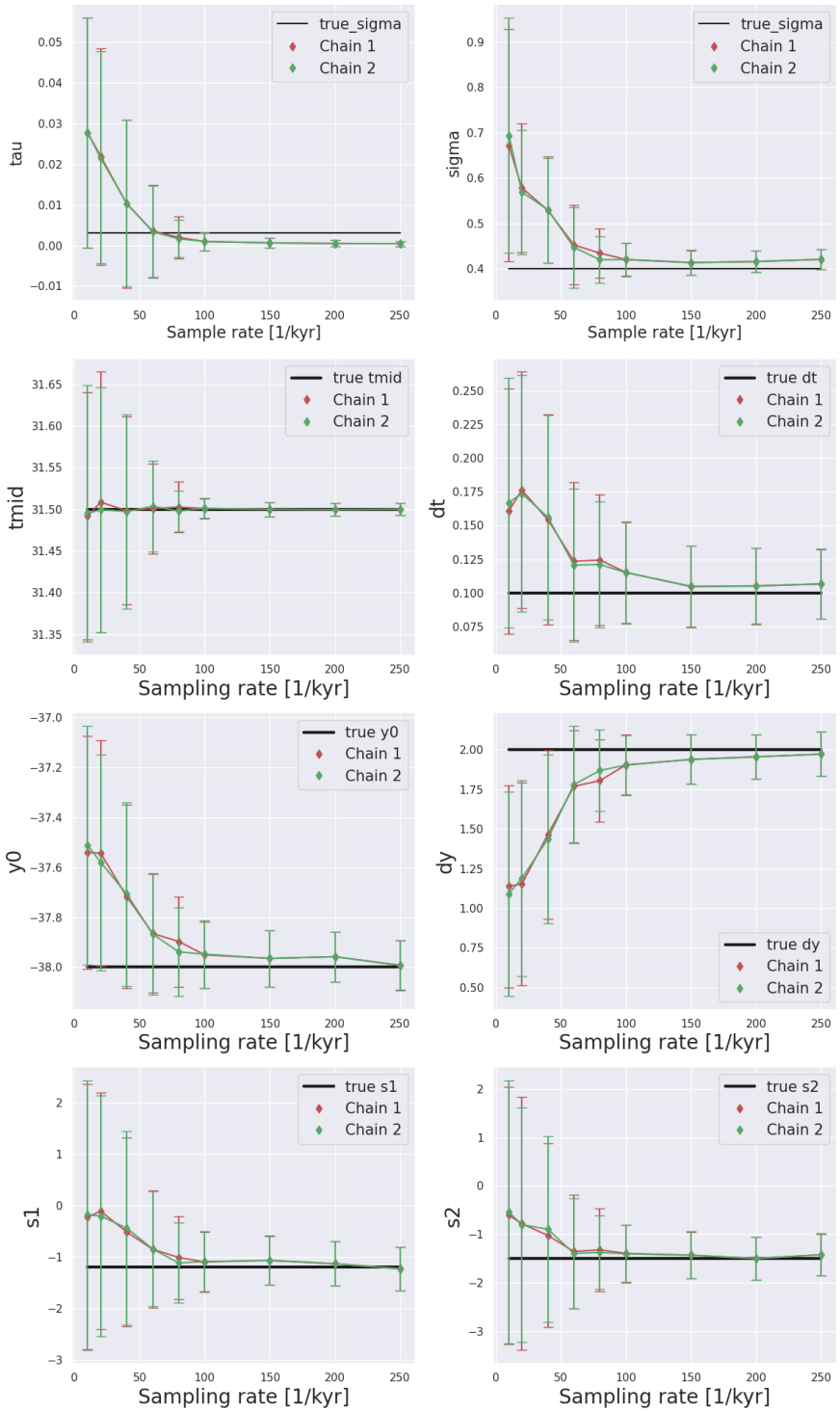

Figure 5.4: This plots shows the result of test 1, investigating the sampling rate. The error bars are calculated from an ensemble of 50 transitions with identical parameters but different realisations of the noise added.

5.3.2 Test 1b: Correlation

This subsection will investigate how the posterior distributions of the inferred model parameters correlate. Figure 5.6 shows scatter plots between all parameters for the slope model for a single run with the IRFM method. There are three groups of correlated relations. The first group is between y_0, Δy, $s1$, and $s2$. The next group is between $s1$, $s2$, t_{mid}, and Δt. The third group is between the noise parameters τ and σ. When referred to as a group, this means the mentioned parameters are all inter-correlated directly or indirectly.

All three groups displays logical correlations. As an example, for the first group, it makes sense that changes in the initial level y_0 affects the value of the initial slope $s1$. If y_0 is estimated larger than the signal $s1$ will increase to shift the line down. A similar relationship exists for Δy and $s2$. As the final level is defined as $y_0 + \Delta y$ it is only logical that these two parameters are correlated. The arguments for group one are illustrated in figure 5.5 with some random data. The figure shows the best fit for two fixed values of y_0. The two other groups follow a similar logical connection, where the correlation balances out if one model parameter is too large a negatively correlated model parameter would be too small.

None of the correlations display anything unusual that should be considered when interpreting the results. If two of the model parameters are misfitted and does not match the input values, it might be a result of the model struggling to find one model parameter and the correlation between the two acting as a correction. Thus it is important to be aware of the correlation groups.

5.3.3 Test 2: No Slopes

Figure 5.7 shows the result of test 2. Test 2 showcases difference of the original RFM to the new model with slopes. In test 2 a similar approach to test 1 was used. Test 2 uses the exact same data as test 1, meaning the same realisation of the noise model, and the same parameters for the true model. The performance is expected to be worse, as the true model and the sample model differs. It is immediately noticed that y_0 and Δy are not converging towards the true values. y_0 is estimated too large, and Δy estimated to small. The result for τ is unchanged compared to test 1, however σ converge towards a larger value than the true value. t_{mid} is the only parameter which fits perfectly without any problems. Again the method draws 6000 tuning samples and 1000 posterior samples.

The misfit in Δt, Δy, and y_0 stems from the different model used for the data and the sampling. Both slopes are negative, meaning the value of y_0 and Δy are increased and decreased respectively. This will then also affect the transition length Δt to be shorter, just as observed. The observed changes has no effect on the mid point of the transition, which is also perfectly found in both tests. The general success for t_{mid} owes to the relatively high step compared to the noise amplitude, even after the scaling of the standard deviation.

It should also be mentioned that the difference in results for test 1 and 2 are observed to be larger in the ice-core region, and smaller in the speleothem region. However, this appears to be a result of the resolution being low, as the model finds slopes closer to 0, making it equal to the flat model, in the speleothem region, then converging towards the true value in the ice-core region.

With the systematic misfit by the flat model, figure 5.7 shows that the IRFM is necessary for reliable results in cases where the records have strong slopes before and after the transitions of the DO events. However, the method is consistent in this test for finding the midpoint. This means that the new results are not expected to demonstrate significant divergence from the previous results.

5.3.4 Test 3: No variations

Test 3 investigates the resolution as well as test 1 and 2, however in test 3, only a single data set is used where data points are removed systematically from the data set to emulate the ice-core and speleothem regions for the resolution. It should be mentioned that 4 chains was used, which can be seen on figure 5.8. Additionally, this method had less variations, thus the number of tuning samples were increased to 10000 samples but still the 1000 samples for the posterior distribution. Similar results as the previous tests is observed. t_{mid} fits perfectly and δt, Δy, and y_0 again are misfitted in the speleo region, and found in the ice-core region. When there is a large variation between each chain as seen at resolution 66 and 50, the chains have either found several solutions or the sampler is not fully converged yet.

The way the noise is removed changes how it is applied to the relevant data set, meaning that the noise which is propagating from the previous data point to the next is lost when removed. However, this should only have an effect similarly to test 1, where the noise becomes white, when the correlation time exceeds the average spacing between points.

This test was mostly to investigate if different methods of changing the sample rate would yield distinct results. There is some minor variations compared to test 2, but generally the two test produces similar results.

5.3.5 Test 4: Tuning samples

Test 4 investigates the number of burn in or tuning samples that are drawn, before sampling from the posterior samples. Here, two data sets are created with the same parameters but different temporal resolutions. One dataset is created with a resolution of 25 samples/kyr, which is typical for the Hulu speleothem record, and 200 samples/kyr, which is typical for the Ice core records. The analysis is again run on 50 different realisations of the noise for each data point. The hypothesis is that the speleothem data needs more tuning for the posterior distributions to converge. However, it can be observed on all the plots in figure 5.9, that the tested values for the tuning sample size appears to have no influence on the result.

Assuming there exists a lower limit for the number of tuning samples required to converge, and the tests show no change in the posterior solutions for the investigated values, this suggest that the limit for the number of tuning samples is outside the investigated region. Furthermore, if the number of tuning samples can be dramatically reduced, this pose as a computational advantage, compared to the earlier methods, which would require a significantly larger number of tuning samples.

When applying the method on the paleoclimatic records a set-up of 6000 tuning draws and 1000 posterior draw will continue to be used as the standard for this study.

5.3.6 Test 5: Signal to noise ratio

Figure 5.10 shows the resulting posterior estimates for tests 5. This tests seeks to determine a limit for the model with respect to the inverse signal to noise ratio, SNR^{-1}, where the model fails to find the known model parameters. Testing for various values of σ the inverse signal to noise ratio is here defined as the fraction between the input or white standard deviation $\sigma_\epsilon = \sigma_W$ and the step size Δy:

$$SNR^{-1} = \frac{\sigma_W}{\Delta y} \tag{5.5}$$

The chosen range covers extreme values for both small and large σ in order to exhaust all possible scenarios in observed data:

$$\sigma = \{0.1, 0.2, 0.3, 0.4, 0.5, 0.6, 0.7, 0.8, 0.9, 1.0\} \tag{5.6}$$

The upper left panel on figure 5.10 shows the linear correlation between the noise and inverse signal to noise ratio. Here the σ values are from the analysis with the IRFM. In the second panel containing the correlation time τ, it appears relatively constant for all values of σ with uncertainties around ± 1 year. T_{mid} starts to diverge and give uncertain results for $\sigma = 0.9, 1$. The parameter y_0 share the same behaviour diverging after $\sigma \geq 0.9$, with uncertainties around 0.2. The mean value for the two slopes $s1$ and $s2$ are relatively constant for all values of σ, with uncertainties reaching 1.3 to 1.5. The only parameter that appears to be strongly affected by σ is the duration, Δt. The values for Δt starts to significantly diverge around $\sigma = 0.7$.

Most of the parameters are relatively stable during the entire test. Parameters such as y_0 and Δy show a clear bias already around $\sigma = 0.4$. Increasing σ and thereby the noise have a similar effect to lowering the step size as the SNR^{-1} becomes smaller. The most valuable parameter to find is the midpoint or the onset, in which case the estimate for a max value of the SNR^{-1} should be based off the behaviour of t_{mid} and Δt. For the largest value of $\sigma = 1$ the standard deviation for the midpoint is on the order of half the duration of the transition (± 50 years). The duration shows large uncertainties and the mean starts to diverge with more than 20 % of the true for $\sigma = 0.7$, meaning a sensible limit would be for $\sigma = 0.6$ meaning $SNR^{-1} = 0.3$.

5.3.7 Test 6: Prior

For test 6, the prior for τ was changed from a uniform distribution to a half-normal distribution. The uniform distribution was defined with an upper limit at 100 years, which were much larger than the input values of τ, at around 3 years, as well as the expected values for the observed data of 3 to 8 years. Thus the hypothesis for the change in prior was that the consistent overestimate of tau for smaller sampling rates would be immproved. Additionally it would also improve cases where the model sees the transition as red noise with a large τ and instead fits the ramp as a line with large variations in the noise. The resulting plots on figure 5.11 for test 6 is in general similar to the result of test 1 on figure 5.4. Only the plot for τ displays a significant difference. For the low sample rates $(10, 20, 40, 60, 80)$ the mean value for *tau* starts at 10 years and converges to around 1 year at sample rate 100 samples/kyr.

Compared to test 1 where τ starts at a value of about 30 years and converges to a value around 1 year at sample rate 100 samples/kyr, similarly to test 1. Thus the new prior improved the values for τ but did not have any other particular effect on the remaining model parameters. The test does not show if the new prior eliminates the case for when the model misses the transition and fits it as noise.

Figure 5.5: This plots shows some random data with two manually set posterior solutions. The yellow and red lines illustrates how a different value of Δy affects the slope of $s1$.

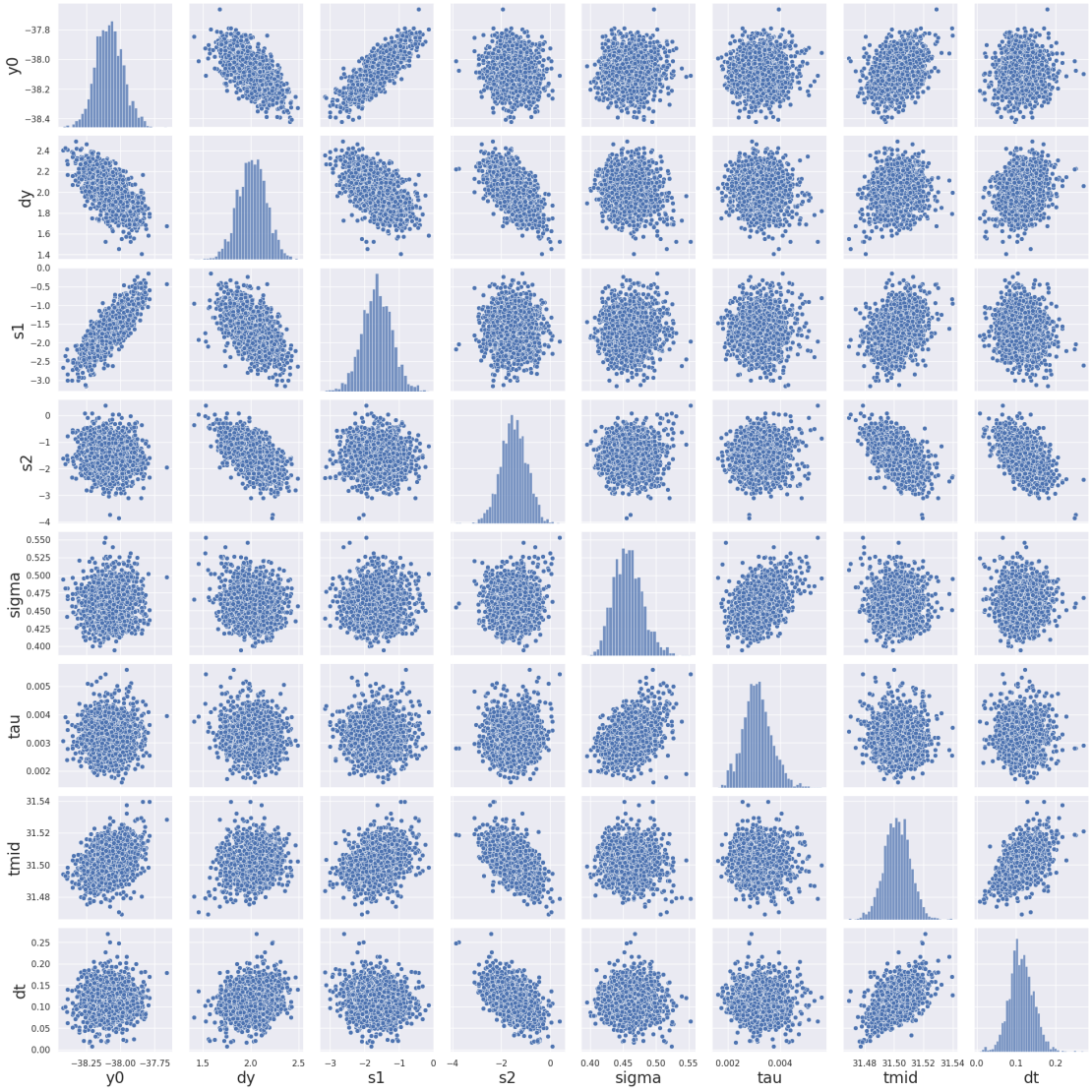

Figure 5.6: This plots shows the correlation in the posterior distributions between the parameters sampled in test 1. Especially $s1$ and $s2$ have strong correlations to y_0, Δy, t_{mid}, Δt. However this is expected since the location of the onset and the end of the transition tunes the slope to be more or less steep.

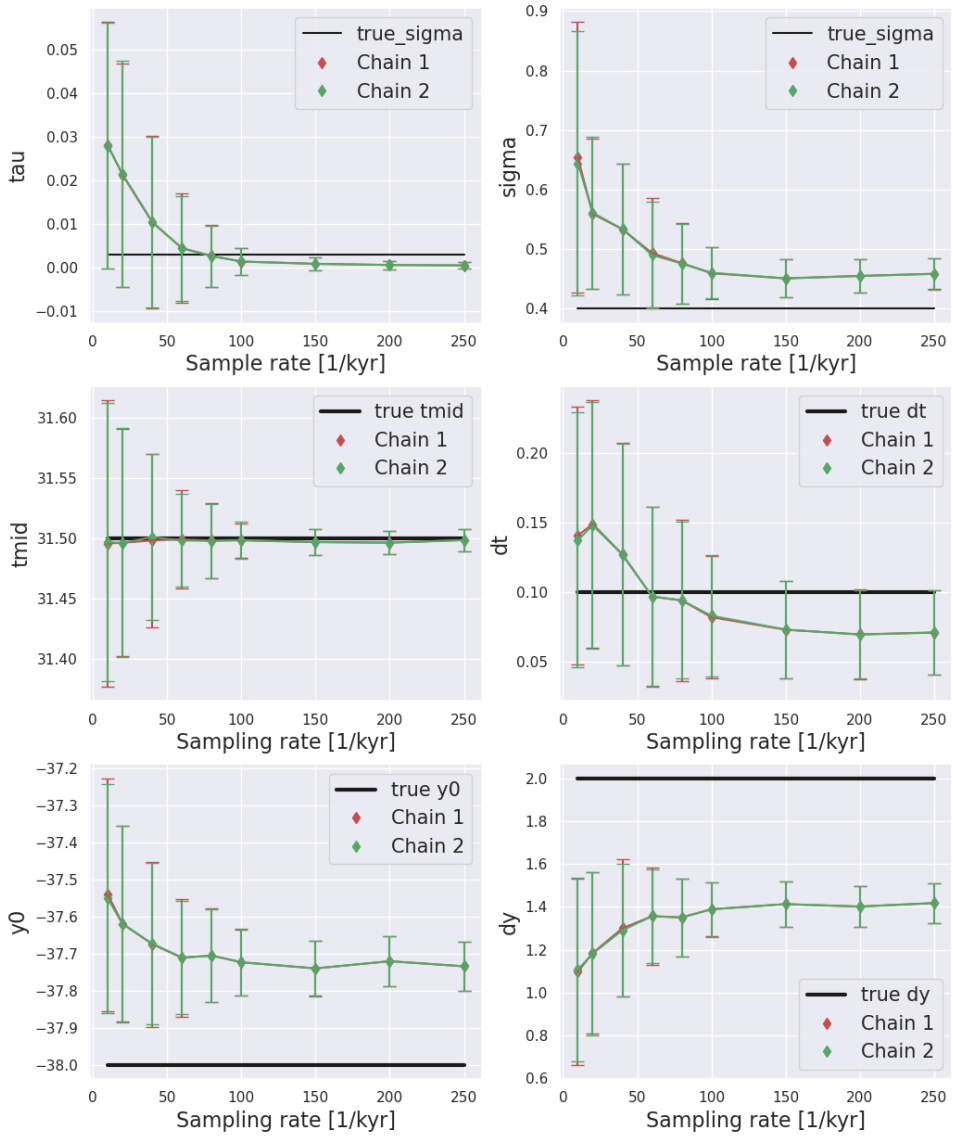

Figure 5.7: This plots shows the result of test 2, investigating the sampling rate on the same data as in test 1. A similar approach as in test 1 is used, however instead of the IRFM, the initial flat RFM is used. There are clear differences between the two results.

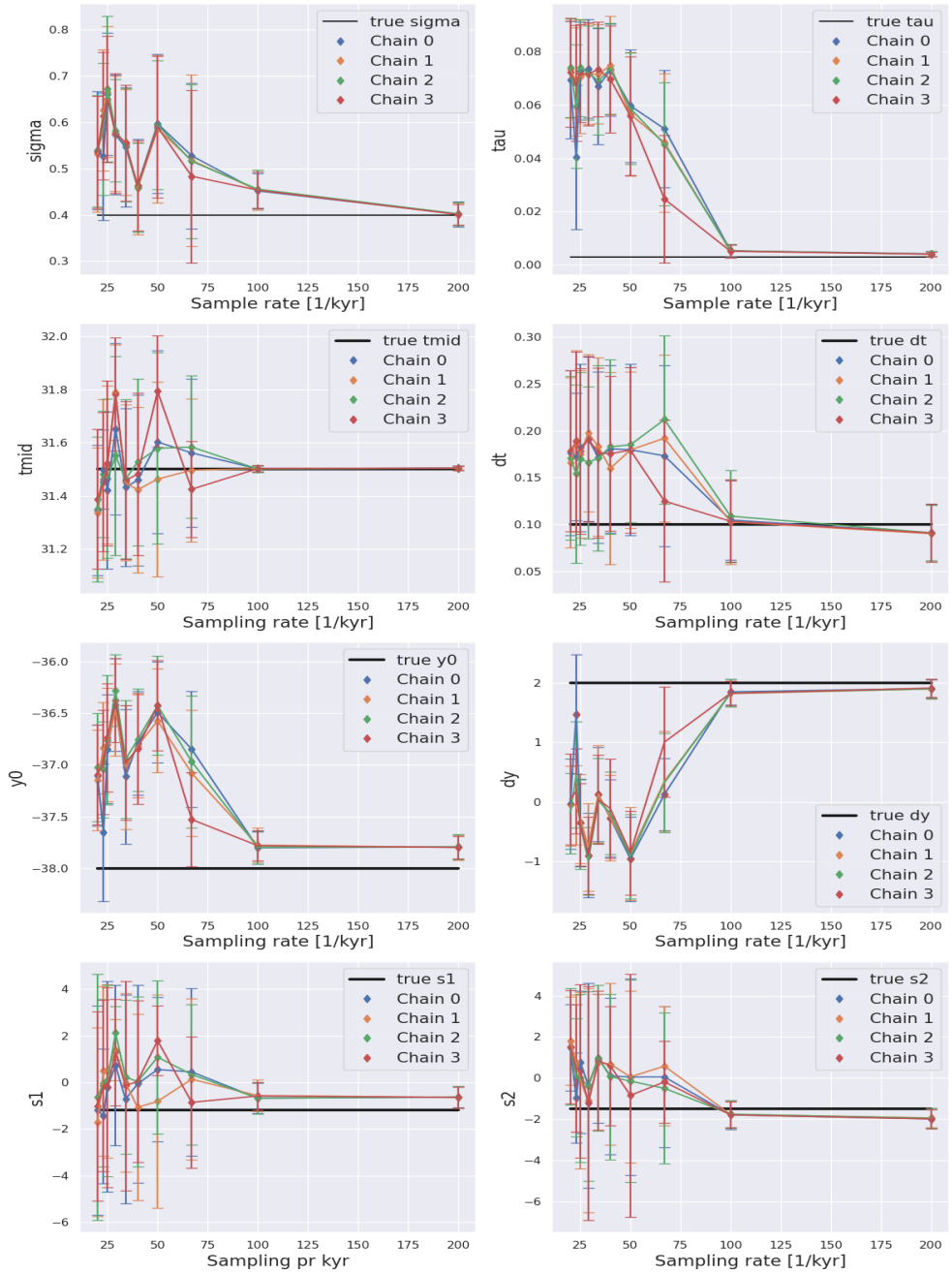

Figure 5.8: This plots shows the result of test 3, investigating the sampling rate on 1 data set with 200 samples over 1000 years. For each point on the x-axis we take every i'th data point and redo the test. Here we use four chains instead of the previous two and it is important to mention that since we are not reapplying the noise for each subset, we only run the method once with the four chains.

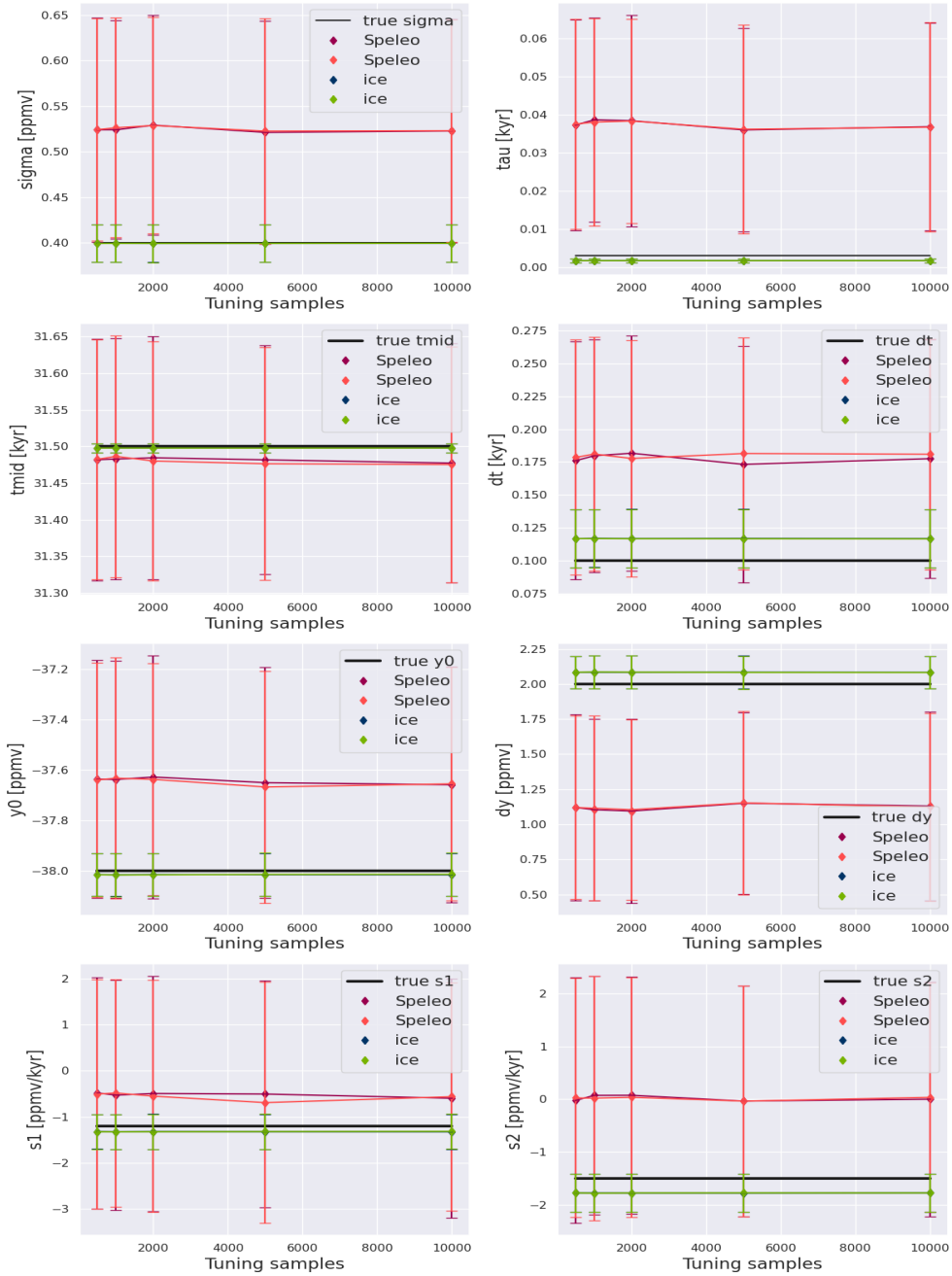

Figure 5.9: This plots shows the result of test 4, investigating the number of burn in samples needed for the posterior distributions to properly converge. Each point on the x-axis shows the number of tuning samples drawn. Here we use two chains on two different datasets. One with a resolution in the speleothem region (20 samples pr kyr) and one in the ice-core region (200 samples pr kyr).

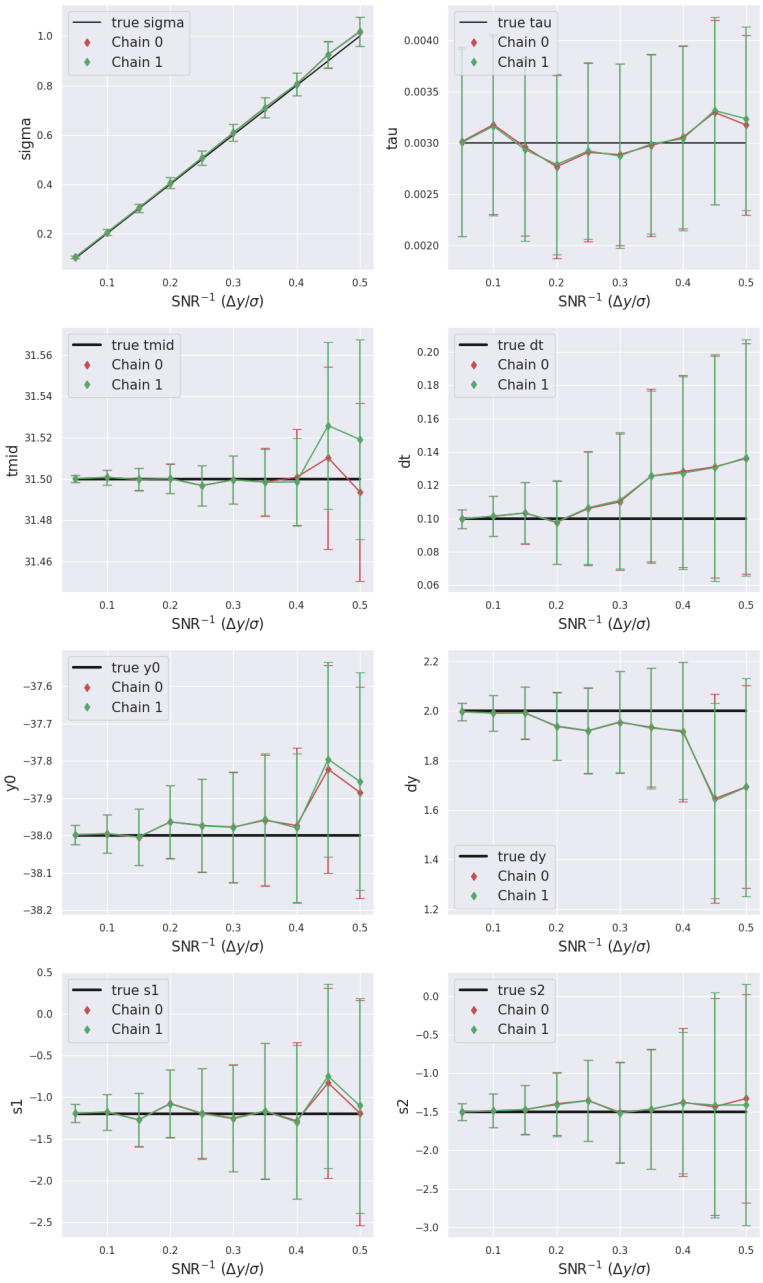

Figure 5.10: This plots shows the result of test 5, investigating the influence of signal to noise ratio on the model result. Each point on the x-axis shows ratio of the standard deviation and step size of the data, here referred to as signal to noise ratio. Here we use two chains and 50 iterations pr variation of sigma.

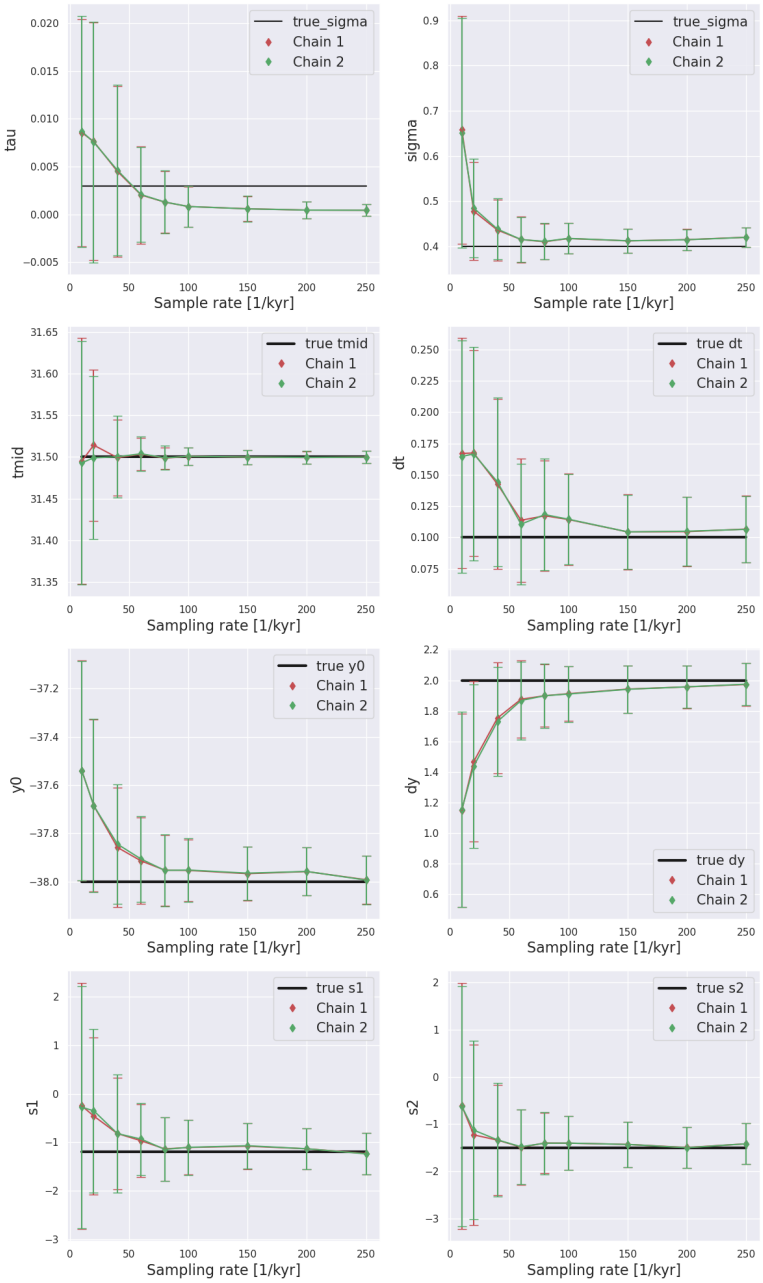

Figure 5.11: This plots shows the result of test 6. The input model parameters used to construct the data is identical to test1, however the prior of τ, has been tuned to be a half normal that favors smaller values. (And the prior for t_{mid} is)

Chapter 6

Results

After testing the Improved Ramp Fitting Method (IRFM) on surrogate data, the precision and effectiveness of the model has been proven against known parameters. The IRFM can now be applied to real data and compared to other studies using the RMF method, to see if the added modification have improved the results.

A list of fifteen DO events have been selected for the analysis here. The analysis covers the age range from 27 to 60 thousand years ago from Marine Isotope Stage 3 during the last glacial period. This period contains 19 DO events from DO-event 3 to 17.2 (Erhardt et al., 2019). Four DO events are not included in the analysis (14, 15.1, 15.2, 16.1), as they are poorly represented in the Hulu record, following the study by Buizert et al. (2015).

This chapter will present the results of the IRFM analysis in ice-core and speleothem records as well as a technical discussion of the results. A more broad analysis that puts the results in to perspective is reserved for chapter 7. Firstly, the investigation of lead and lag in different ice core measured parameters is presented. The Ice core records have high resolution and well defined transitions which allows for a detailed comparison to other studies. A short summary commenting on the results will be given after the presentation of the result. Secondly, the analysis of the anatomy and lag between Ice Core and Speleothem records using the RFM will be presented. Again it will be followed by a technical discussion of the presented results.

6.1 Age of DO events in Ice Cores

Figure 6.1 shows the six measured records from the two different ice cores analyzed here, $\delta^{18}O$, Ca^{2+}, Na^{+}, and D-excess from NEEM and $\delta^{18}O$ and Ca^{2+} from NorthGRIP.

On the figure the 15 selected DO events are marked. All records are plotted on the GICCO5 timescale. In table 6.1 the MCMC inferred results of the age of the DO-transitions using the IRFM are listed with their uncertainties together with the reference dates and uncertainties from the study by Rasmussen et al. (2014).

The uncertainties for the MCMC inferred midpoint ages are visualized in figure 6.2 in comparison to the reference ages in Rasmussen et al. (2014) and compared accross the two ice cores.

The figure clearly shows how the DO events influences each proxy, thus each DO transition are seen in all records and occurs almost at the same time. It should be noted that the concentrations of impurities (Na, Ca) are higher during the GSs and lower during the GIs. This means that the impurities display a negative ramp step, compared to $\delta^{18}O$ which displays a positive ramp step over the transition of a DO-event. The DO events are also reflected in the D-excess record, which shows different features as the impurities, but they are both defined by a negative ramp step for each transition.

6.1.1 NEEM

The next four figures (figures 6.3, 6.4, 6.5, 6.6) show the results of the analysis for each individual record from the NEEM ice core. Each figure contains the 15 events and the selected time windows. Each time window covers the age determined in Rasmussen et al. (2014) $\pm$250 years. For each run two MCMC chains are used with 6000 tuning sample draws and 1000 posterior sample draws. The priors are given in chapter 5.

On figure 6.3 the analysis of the $\delta^{18}O$ record from NEEM is shown. Each panel contains the fitted data, an ensemble of the posterior 1 σ solutions for two chains indicated by thin red and green lines, respectively, a mean fit solution for each chain indicated by thick lines of similar colors, and three vertical cyan lines, where

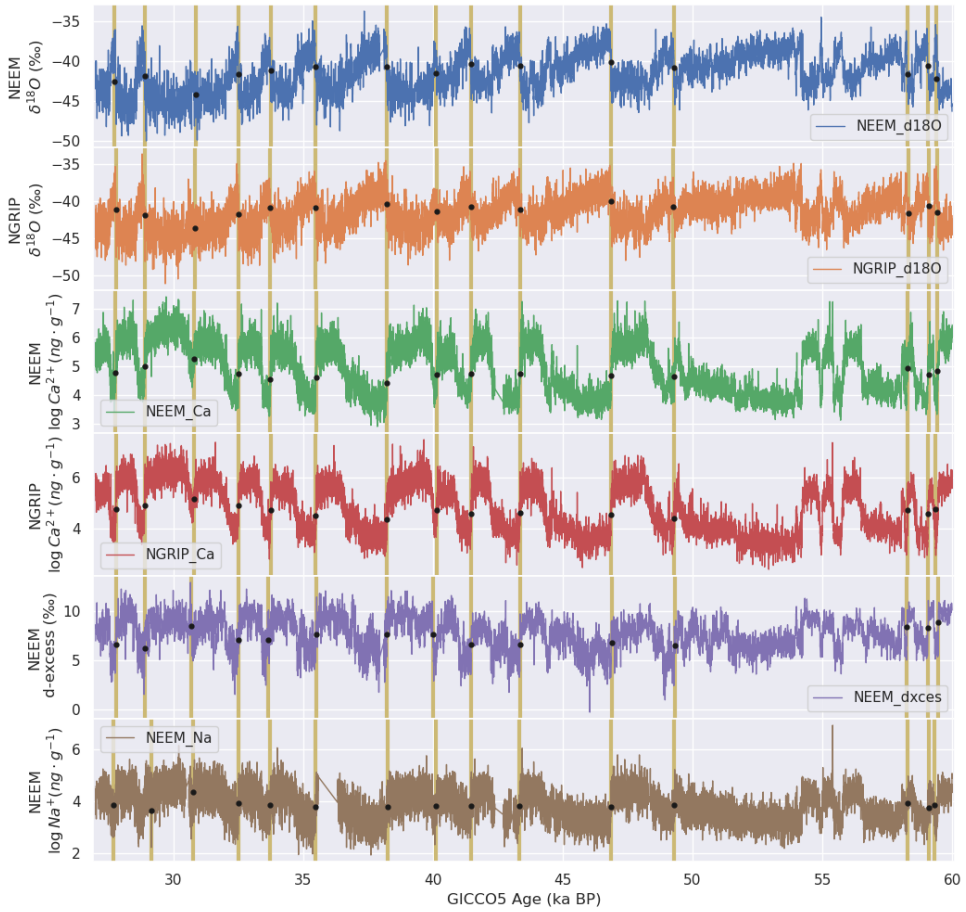

Figure 6.1: This plot shows six ice-core records from NEEM and NGRIP. From NEEM: $\delta^{18}O$ (Blue), Ca^{2+} (Green), D-excess (Purple), Na^{+} (Brown), and from NorthGRIP: $\delta^{18}O$ (Orange), Ca^{2+} (Red). The vertical yellow lines shows the fitted midpoints for each of the investigated transitions. The black dots are also placed at the fitted midpoint with the inferred height $y_0 + \frac{\Delta y}{2}$.

DO-event	This Study						Rasmussen
	NEEM				NGRIP		NGRIP
	$\delta^{18}O$	Ca	D-excess	Na	$\delta^{18}O$	Ca	$\delta^{18}O$
no.	ka	ka	ka	ka	ka	ka	ka
3	27.737 ±0.273	27.776 ±0.007	27.771 ±0.009	27.779 ±0.006	27.775 ±0.011	27.672 ±0.182	27.78 ±0.832
4	28.9 ±0.088	28.888 ±0.02	28.899 ±0.012	28.889 ±0.005	28.894 ±0.016	29.143 ±0.007	28.9 ±0.898
5.1	30.849 ±0.26	30.81 ±0.381	30.774 ±0.019	30.795 ±0.027	30.688 ±0.092	30.772 ±0.301	30.84 ±1.024
5.2	32.502 ±0.024	32.507 ±0.02	32.501 ±0.004	32.51 ±0.013	32.499 ±0.023	32.5 ±0.022	32.5 ±1.132
6	33.738 ±0.019	33.723 ±0.147	33.734 ±0.006	33.75 ±0.031	33.653 ±0.171	33.734 ±0.016	33.74 ±1.212
7	35.478 ±0.026	35.483 ±0.025	35.486 ±0.009	35.483 ±0.008	35.486 ±0.028	35.481 ±0.027	35.48 ±1.321
8	38.217 ±0.053	38.215 ±0.02	38.21 ±0.011	38.217 ±0.007	38.216 ±0.012	38.244 ±0.149	38.22 ±1.449
9	40.098 ±0.24	40.15 ±0.067	40.144 ±0.018	40.149 ±0.014	39.998 ±0.139	40.104 ±0.094	40.16 ±1.58
10	41.449 ±0.018	41.459 ±0.017	41.463 ±0.019	41.464 ±0.009	41.467 ±0.016	41.455 ±0.028	41.46 ±1.633
11	43.347 ±0.027	43.358 ±0.087	43.345 ±0.017	43.345 ±0.014	43.347 ±0.006	43.335 ±0.025	43.34 ±1.736
12	46.854 ±0.01	46.851 ±0.02	46.861 ±0.014	46.859 ±0.011	46.884 ±0.151	46.847 ±0.017	46.86 ±1.912
13	49.282 ±0.022	49.232 ±0.163	49.292 ±0.008	49.289 ±0.033	49.31 ±0.108	49.283 ±0.049	49.28 ±2.031
16.2	58.28 ±0.185	58.307 ±0.178	58.276 ±0.115	58.276 ±0.135	58.261 ±0.233	58.272 ±0.213	58.28 ±2.511
17.1	59.072 ±0.099	59.084 ±0.105	59.089 ±0.124	59.079 ±0.093	59.065 ±0.026	59.092 ±0.205	59.08 ±2.557
17.2	59.397 ±0.258	59.413 ±0.191	59.413 ±0.154	59.365 ±0.177	59.448 ±0.189	59.331 ±0.227	59.44 ±2.573

Table 6.1: This table shows the resulting midpoint age and 2σ uncertainty analyzed in six ice core records for the 15 DO events. The last column shows the results from Rasmussen et al. (2014).

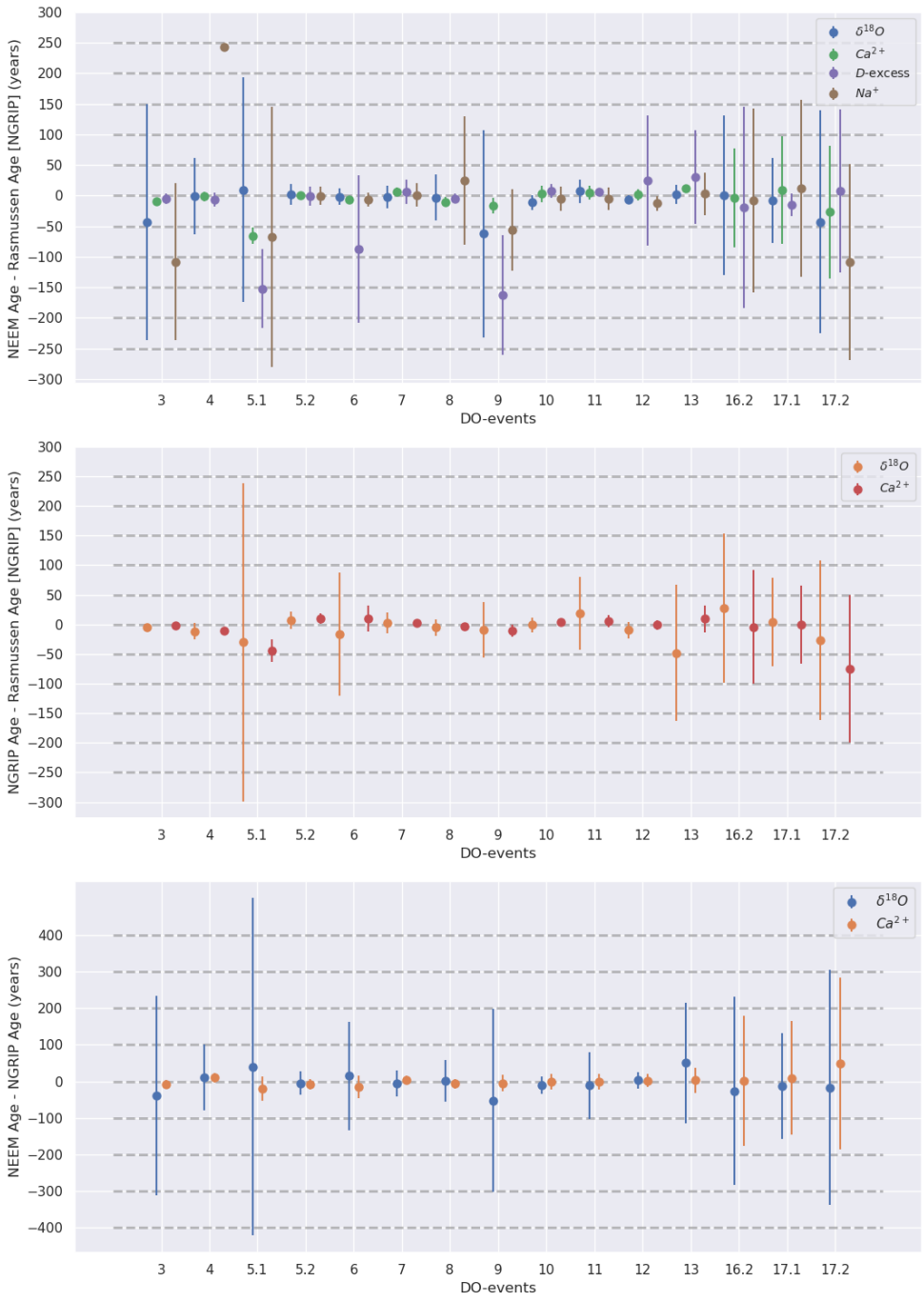

Figure 6.2: The figure shows the difference between the midpoints found with the IRMF and the reference ages from Rasmussen et al. (2014) for NEEM (top), NorthGRIP (middle), and the difference between the two cores (bottom). The uncertainties shown are the 2σ standard deviation in the posterior samples.

the two dotted lines show the inferred midpoints for the two chains, and the full line shows the reference age determined in Rasmussen et al. (2014). Some of the events are well defined, and the model finds the midpoint with only small variations in the posterior solutions. This is the case for events 3, 4, 5.2, 6, 7, 8, 10, 11, 12, 13, and 17.1, and common for all these events, the inferred midpoint is located close to the reference age determined in Rasmussen et al., 2014. Event 5.1 has a very subtle transition and the result is a very flat ramp, and the reference age is outside the inferred uncertainty of the midpoint (see figure 6.2). DO events 3, 9, 17.2 are all misfitted meaning the method does not capture the transition. All three of these transitions are characterised by a short GI, where the search interval covers the entire GI period. This results in a decrease in the signal and a new baseline after the transition, making it difficult for the method to find the transition correctly.

Figure 6.4 shows the Ca analysis, with the results presented as described above for figure 6.3. Most of the transitions are determined successfully with very small variations in the posterior solutions. On figure 6.2 this is also visible as the Ca midpoint ages have the smallest uncertainties of the analyzed parameters. The last three events (16.2, 17.1, 17.2) fits the data less accurately. They all have short GIs as described above, but (16.2, 17.1) find midpoints that still are close to the reference age in Rasmussen et al. (2014).

Figure 6.5 shows the D-excess analysis. Noticeable for this figure is that all of the dashed lines are placed very nicely even for the poorly visible transitions in (6, 16.2, 17.2). For DO events (5.1, 6, 9) the fitted midpoints deviate from the reference age, and the differences for event (5.1, 9) are larger than the 2σ uncertainties. The model misfits the two transitions (5.1, 9) as it finds the backside of the transition instead of the initial change, resulting in a positive value for the inferred Δy.

Figure 6.6 shows the Na analysis. DO-event (4, 5.1, 8) are the first cases where the two chains converge to two significantly different values. Event 4 clearly misfits the transition, and it can immediately be identified on figure 6.2 as an outlier, despite the low uncertainty. Event 5.1 is very subtle, similarly to what was seen in the $\delta^{18}O$ record and display the largest uncertainty (see figure 6.2). Event (16.2, 17.1) are fitted in agreement with the reference age, but display large uncertainties. DO-event (3, 17.2) are both not in agreement with the reference age, and their

uncertainties are both large, however still covereing the reference age.

For all the four records the three last events (16.2, 17.1, 17.2) are the most difficult to fit and generally display larger uncertainties than the rest.

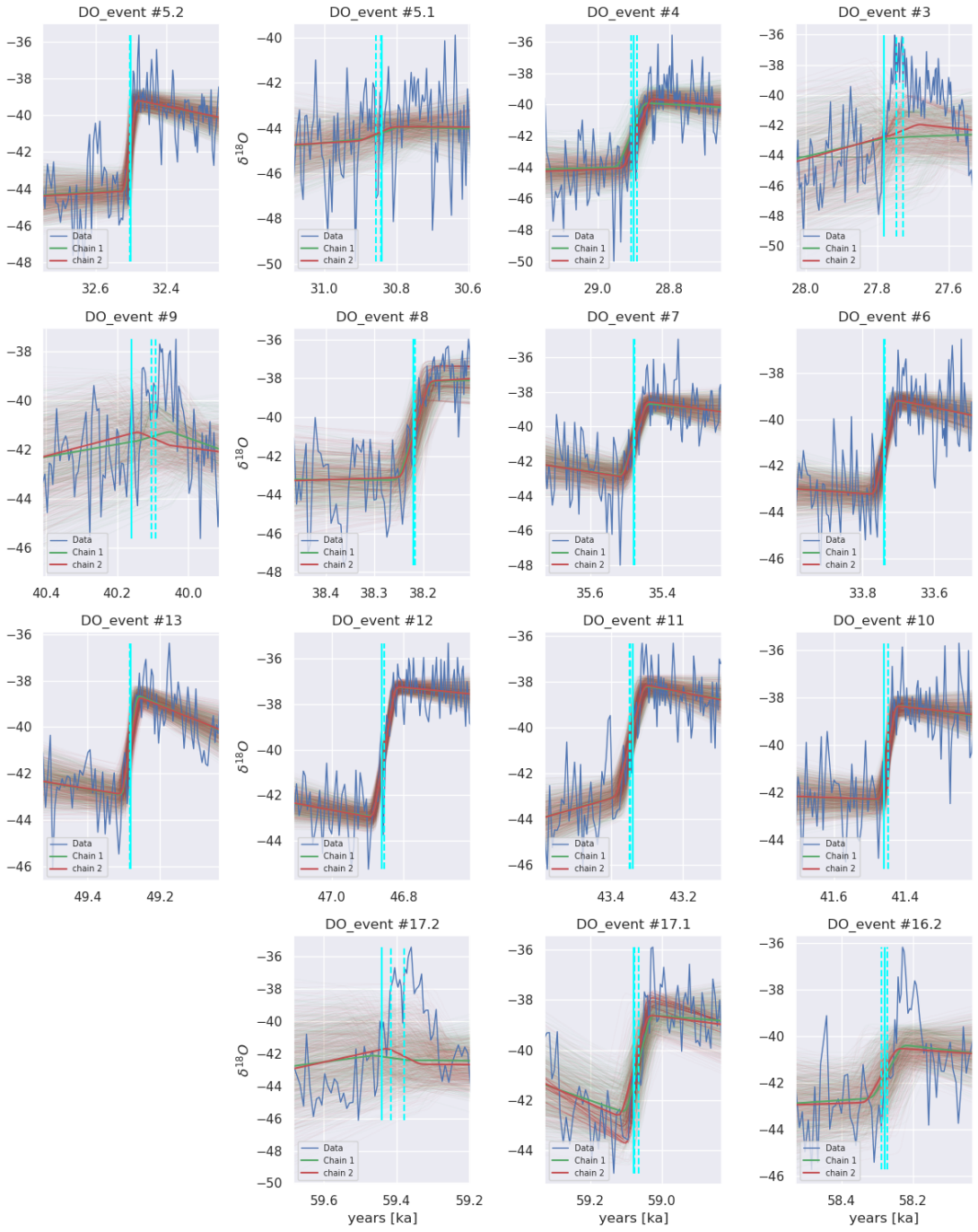

Figure 6.3: The plot shows the result of the IRFM for the $\delta^{18}O$ NEEM record. The posterior fits (transparent) as well as a mean fit (bright color) are displayed as the red and green lines for the two chains, respectively. The cyan lines are the mean midpoint for each chain (dashed) and the ages from Rasmussen et al. (2014) (full).

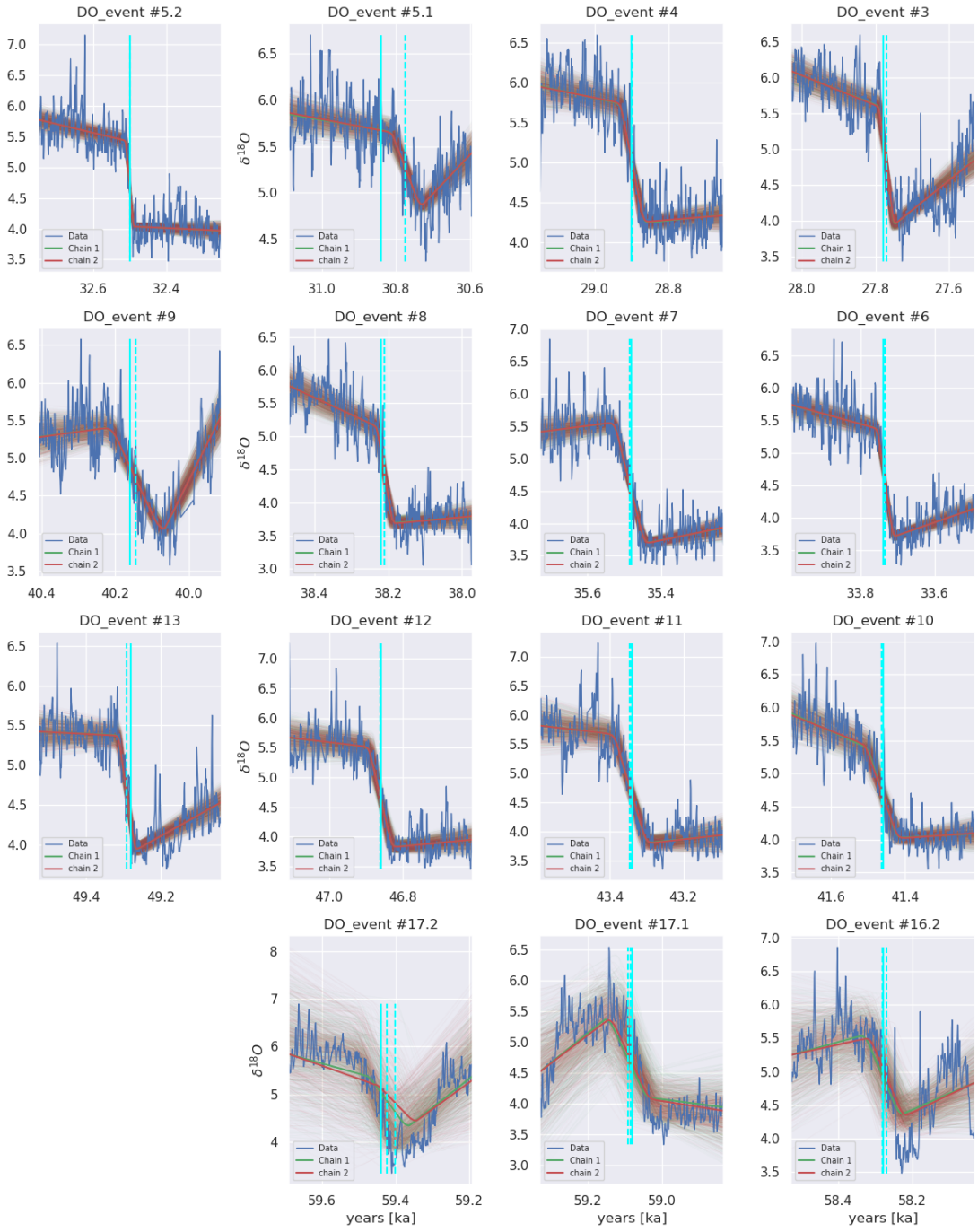

Figure 6.4: The plot shows the result of the IRFM for the Ca^{2+} NEEM record. The posterior fits (transparent) as well as a mean fit (bright color) are displayed as the red and green lines for the two chains, respectively. The cyan lines are the mean midpoint for each chain (dashed) and the ages from Rasmussen et al. (2014) (full).

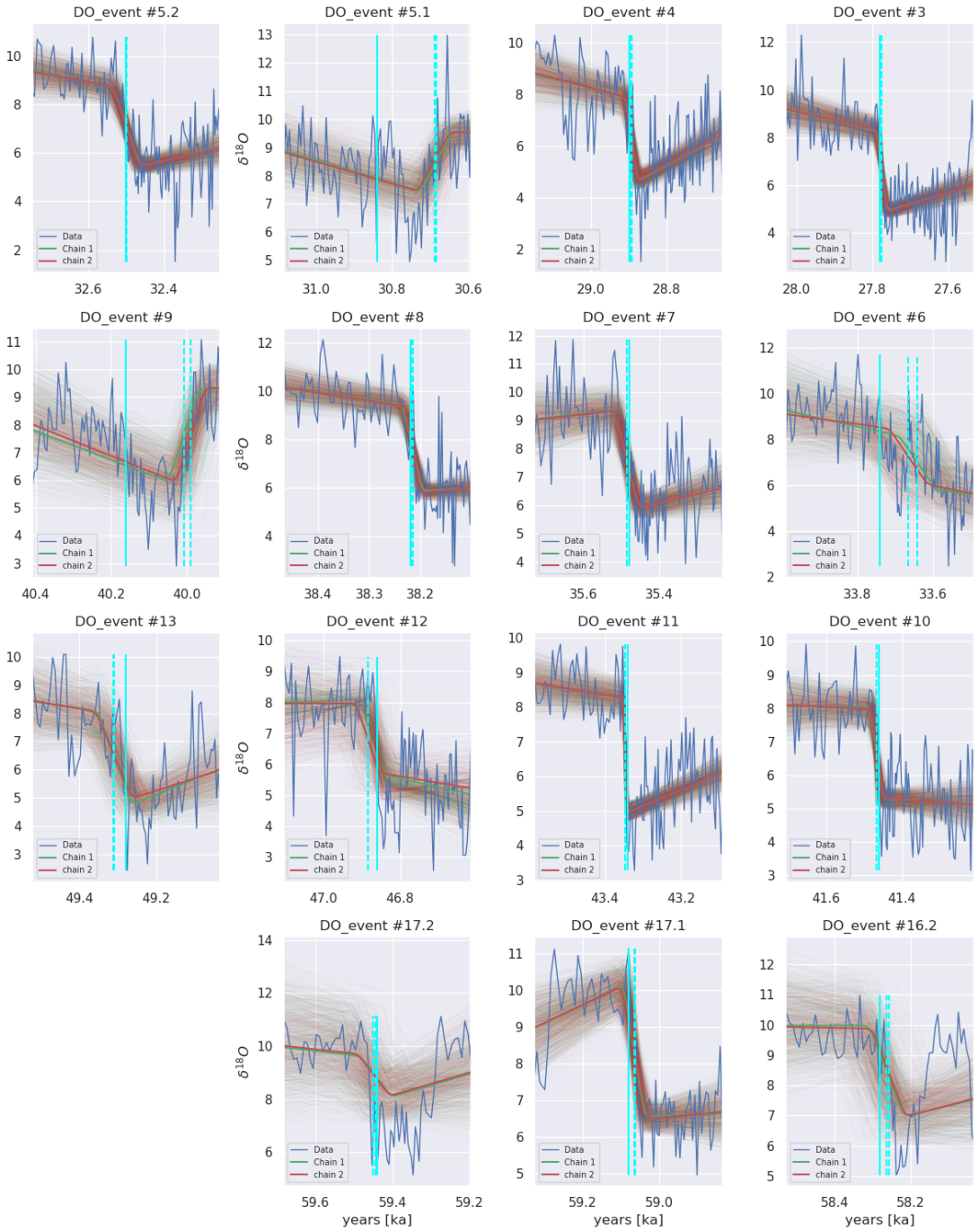

Figure 6.5: The plot shows the result of the IRFM for the *D*-excess NEEM record. The posterior fits (transparent) as well as a mean fit (bright color) are displayed as the red and green lines for the two chains, respectively. The cyan lines are the mean midpoint for each chain (dashed) and the ages from Rasmussen et al. (2014) (full).

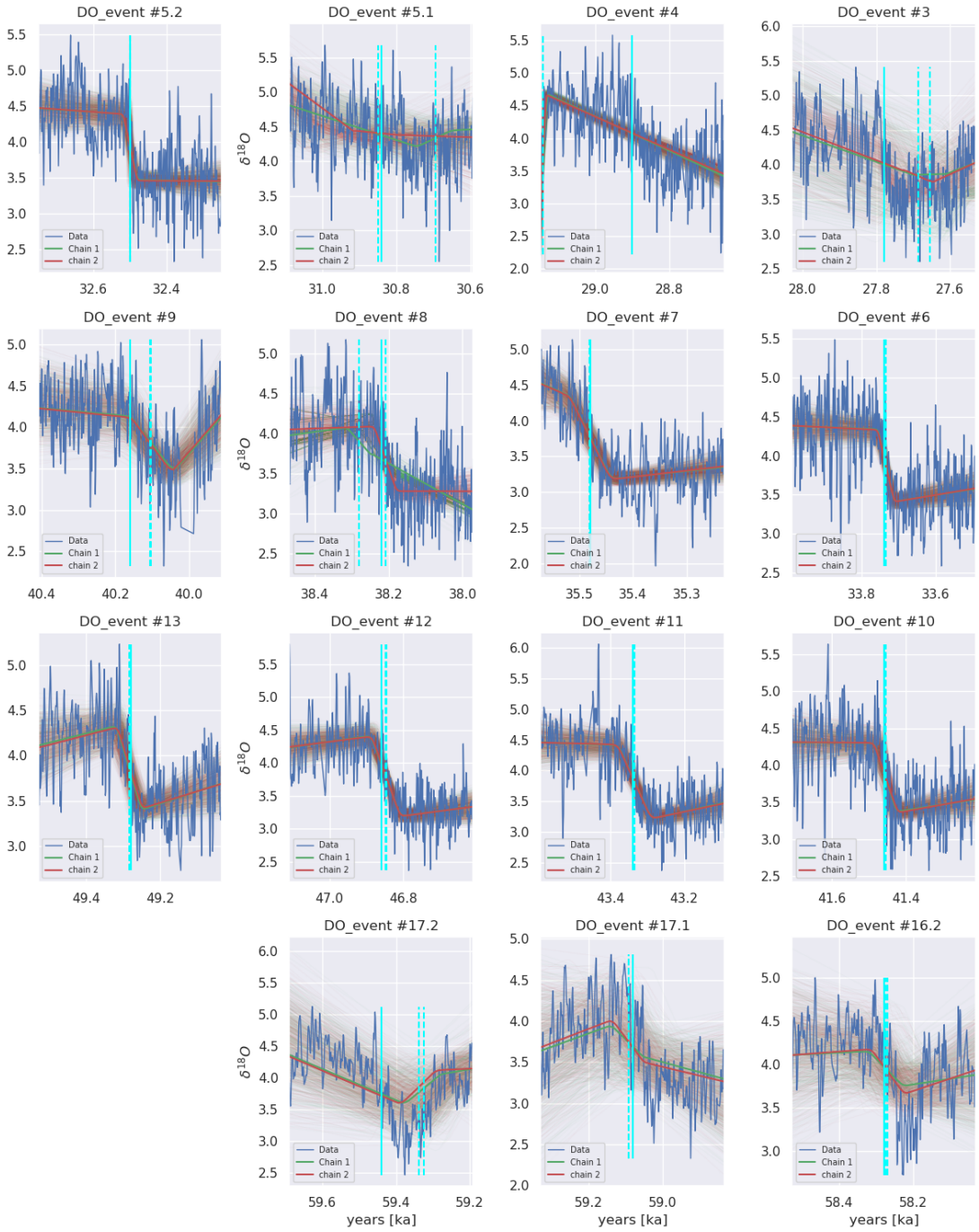

Figure 6.6: The plot shows the result of the IRFM for the Na^+ NEEM record. The posterior fits (transparent) as well as a mean fit (bright color) are displayed as the red and green lines for the two chains, respectively. The cyan lines are the mean midpoint for each chain (dashed) and the ages from Rasmussen et al. (2014) (full).

6.1.2 NGRIP

The next two figures (figures 6.7, 6.8) show the results of the analysis for the NGRIP ice core. Again, each figure contains the 15 events and the selected time windows. Each time window covers the age determined in Rasmussen et al., 2014 ±250 years. For each run two MCMC chains are used with 6000 tuning sample draws and 1000 posterior sample draws. The priors are given in chapter 5.

On figure 6.3 the analysis of the $\delta^{18}O$ record from NorthGRIP is shown. The figures has the same layout as the previous figures with the red and green lines being the inferred lines for each data window and the cyan lines being the midpoints and reference age. DO-event 5.1 has no distinct features in the signal, similarly to in the NEEM core (see figure 6.3). DO-event 13 is only fitted correctly by one of the chains (Green). For DO-event (16.2, 17.2) the inferred midpoints are close to the reference age, however the lines poorly describe the signal. Generally the data and anatomy of the events are similar to the data from NEEM.

Figure 6.4 shows the Ca analysis. The Ca data consistently has smaller variations, better defined transitions, and have significantly smaller uncertainties than the $\delta^{18}O$ data (see figure 6.2). As mentioned, this also applies to the NEEM ice core. DO-event (16.2, 17.1, 17.2) in general have larger uncertainties compared to the other events, which is reflected in the posterior solutions on figure 6.4. Event 17.2 is the only transition where the inferred model poorly matches the signal and reference date in this analysis.

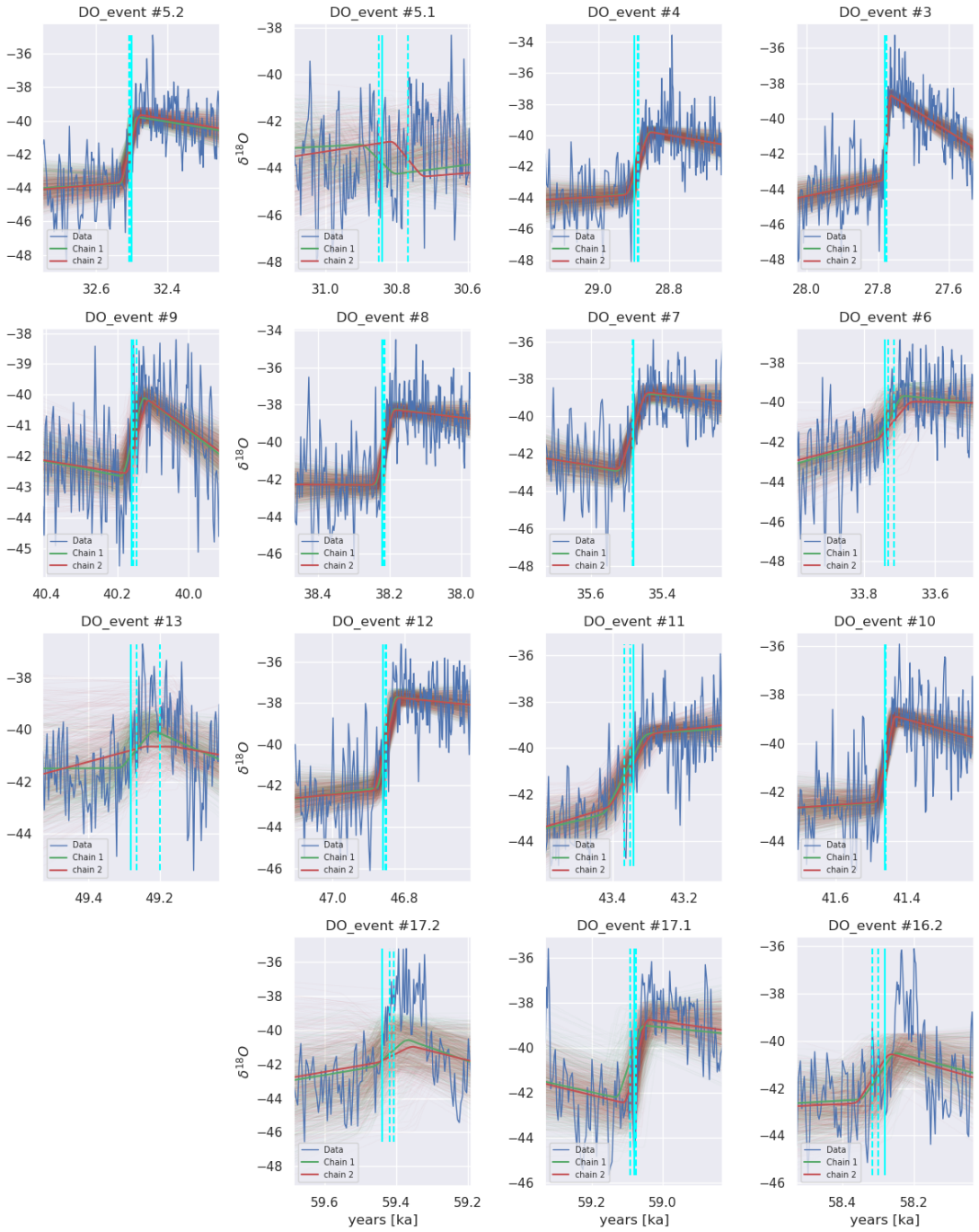

Figure 6.7: The plot shows the result of the IRFM for the $\delta^{18}O$ NorthGRIP record. The posterior fits (transparent) as well as a mean fit (bright color) are displayed as the red and green lines for the two chains, respectively. The cyan lines are the mean midpoint for each chain (dashed) and the ages from Rasmussen et al. (2014) (full).

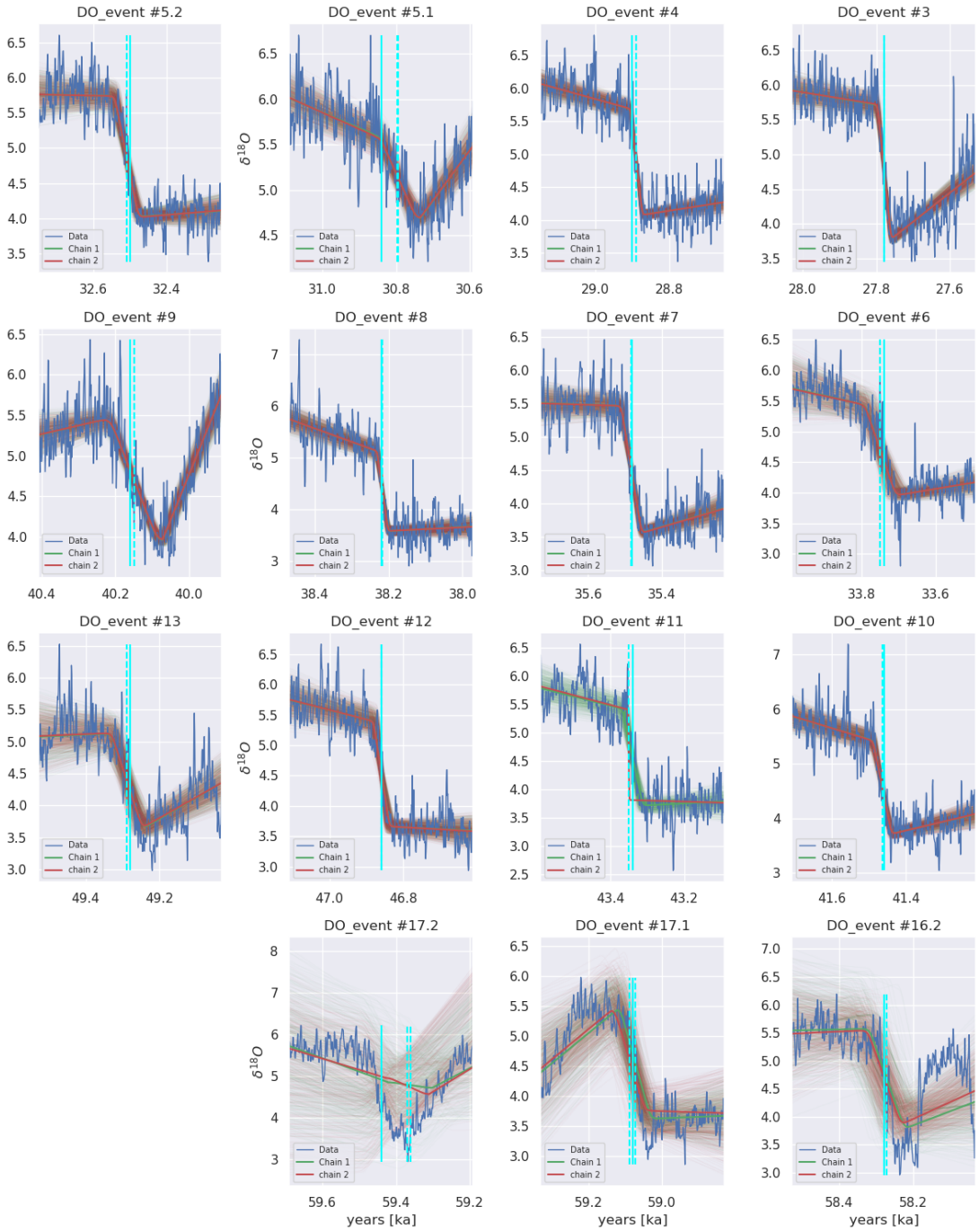

Figure 6.8: The plot shows the result of the IRFM for the Ca^{2+} NorthGRIP record. The posterior fits (transparent) as well as a mean fit (bright color) are displayed as the red and green lines for the two chains, respectively. The cyan lines are the mean midpoint for each chain (dashed) and the ages from Rasmussen et al. (2014) (full).

6.1.3 Anatomy of DO events

In order to get a better overview and to compare the inferred results across the 6 records, the previously shown results are investigated in detail in the following figures.

Figure 6.9 shows scatter plots for different sets of model parameters or their 1σ standard deviation. The parameters are chosen to highlight the observations made in the previous section and to characterize the anatomy of DO events across different parameters. The black dots denotes the transitions that are mentioned above where the inferred model poorly describes the data or where the model had problems to find the right parameters.

Figure 6.9 panel A shows no distinct correlation between the values of the slopes before and after the transitions. On panel B Δy is organised into levels depending on the record and regardless of Δt, except for the poorly fitted black dotted points.

Panel C and D shows that the signal noise σ is organises into two distinct levels, one for $\Delta^{18}O$ and D-excess and one for the aerosol parameters Ca and Na.

Panel E shows that there is no general correlation between the value of tau and $sigma$, but τ generally display smaller values for the well fitted transitions. In panel F all the black dotted events are generally placed towards smaller values of Δy, and have the highest values for τ. Additionally, the the black dotted events also have larger values of τ. For the remaining DO events τ is relatively constant, regardless of the value of Δy with values around 4 years.

Panel G and H both shows a linear relationship between the 1σ standard deviation for Δt and t_{mid} as well as Δy and y_0. This shows that when one parameters is well defined, this applies to both parameters. On panel G the black dotted lines appear to fall outside of the linear relationship when the standard deviation for t_{mid} is large.

Figure 6.10 illustrates differences in the ages of DO events between the different records from NEEM and NorthGRIP with respect to onset, midpoint, and endpoint. The three columns on the left, shows the inferred ages for the NEEM records and the three columns on the right shows the NorthGRIP records. All ages are given relative to the corresponding age in the respective Ca record for that

ice core, hence all dots fro the Ca records are placed at $\delta t_{mid} = 0$. These three values are derived from the inferred midpoint t_{mid} and inferred transition duration Δt. Positive values corresponds to a lag compared to the Ca ages, meaning the transition happened after the Ca transition.

The distributions on the bottom panels represents the dots in the panel above and show the general lead and lag relationships between the records. The Na age for DO-event 4 is an outlier, and is out of the range shown on the figure. As the area below the curve is normalized, the taller the distribution is, the smaller the general variation is for the record in question. This indicates that as the distribution for $\delta^{18}O$ gets smaller, the variation of the onset is smaller than the variations of the endpoint compared to the Ca ages.

Figure 6.11 is two zoom-ins of figure 6.10. The panels shows the onset, midpoint and endpoint of the four parameters: $\delta^{18}O$, D-excess, Na from NEEM and $\delta^{18}O$ from NorthGRIP. In the top panels the above-mentioned outlier can be seen. This outlier corresponds to DO-event 4 which was misfitted for the Na record.

The bottom panel shows a full zoom for the distributions. The two $\delta^{18}O$ records appear to have slightly different timings compared to Ca, with the NorthGRIP ages having a lag of 10 years. The Na record have on average a lag of 10 years and the D-excess have a lead of 10 years relative to the Ca record, respectively. The study by Erhardt et al. (2019) also estimates that the Ca record shows a lead of 10 years to Na and $\delta^{18}O$. The distributions found in this study however are much broader than what was found in Erhardt et al. (2019).

6.1.4 Summarizing remarks

For most of the transitions that the models fails to identify, the signal has several changes in slope over the search interval, e.g. due to a short GI. It is very possible that the model falsely recognises the short GI's as longer term variability in the signal with high values of τ, i.e. the transition is hidden as red noise.

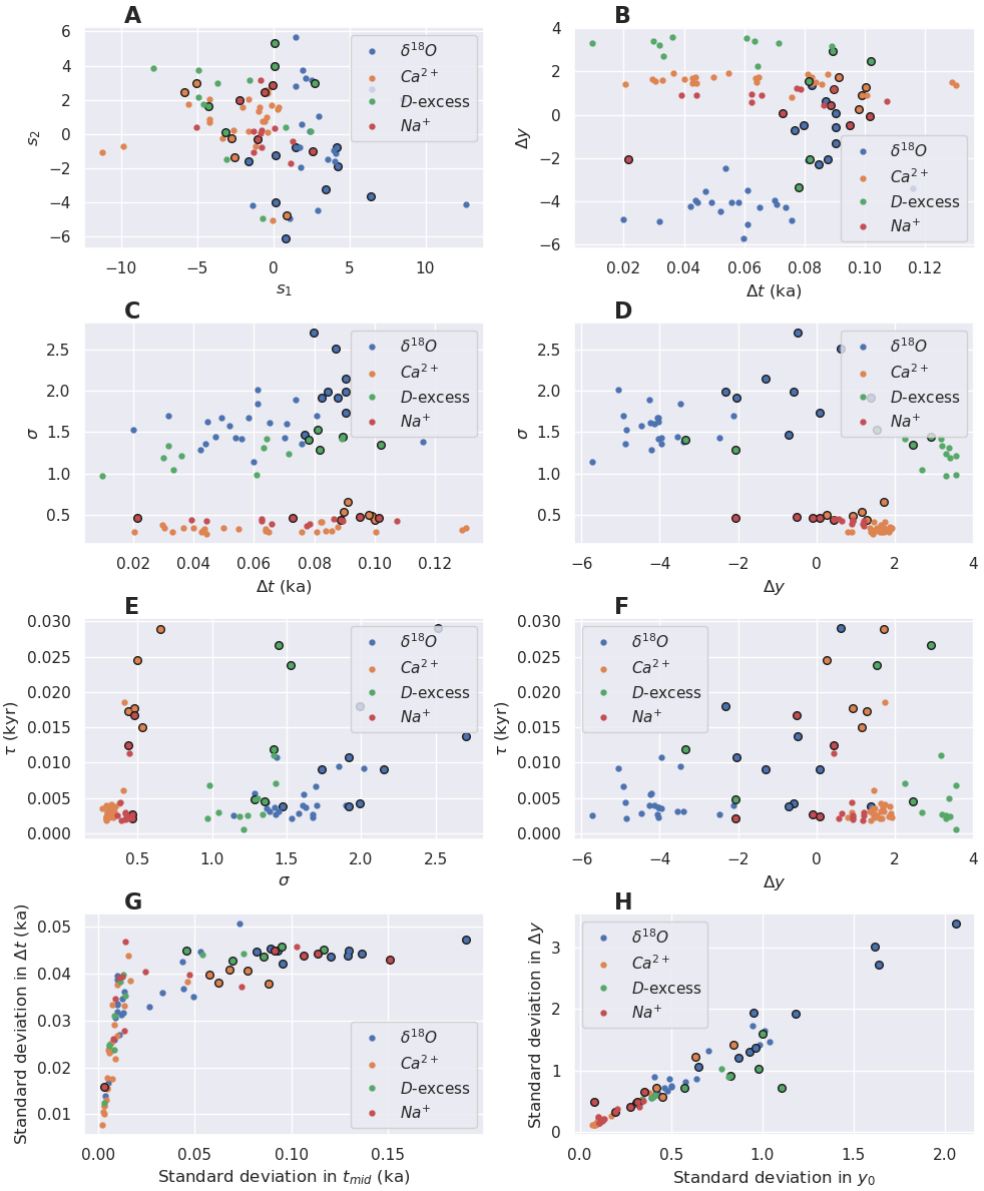

Figure 6.9: This figure shows the inferred model parameters for all ice core records and DO events studied. The dots are grouped together after parameters across records, i.e. the blue dots contain NorthGRIP and NEEM $\delta^{18}O$ values. The model parameters plotted are chosen to highlight the anatomy in the the different records, found with the IRFM. The black dots denote results from DO events where the posterior solutions poorly describes the signal (see text for details).

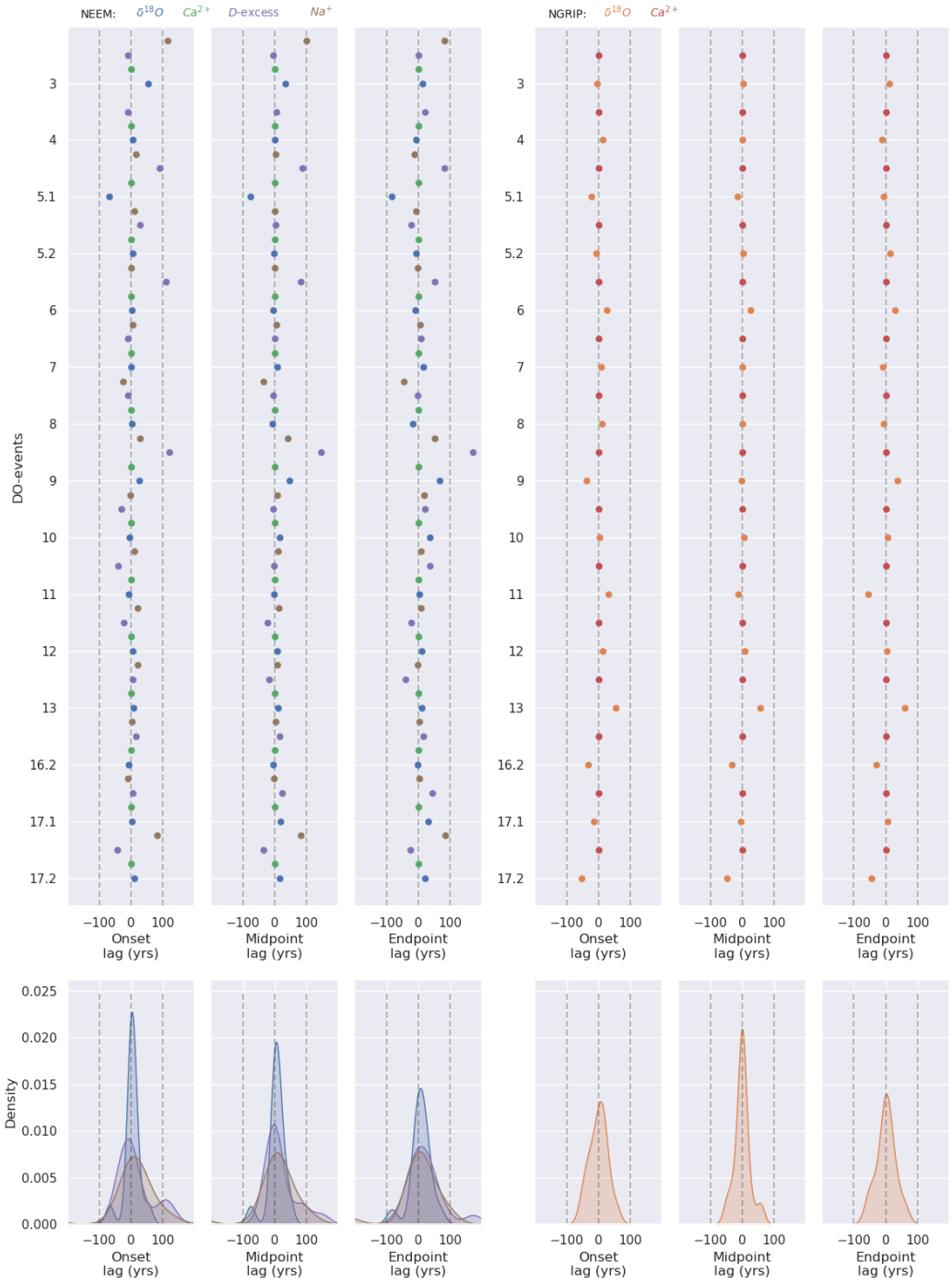

Figure 6.10: This figure shows the result for the inferred midpoint t_{mid} and transition duration Δt from the analysis of the NEEM and NorthGRIP ice cores. Each dot is plotted as age difference to the midpoint in the Ca records. Thus, the green and red points are all placed at $\delta t_{mid} = 0$, and have no distribution on the bottom panels.

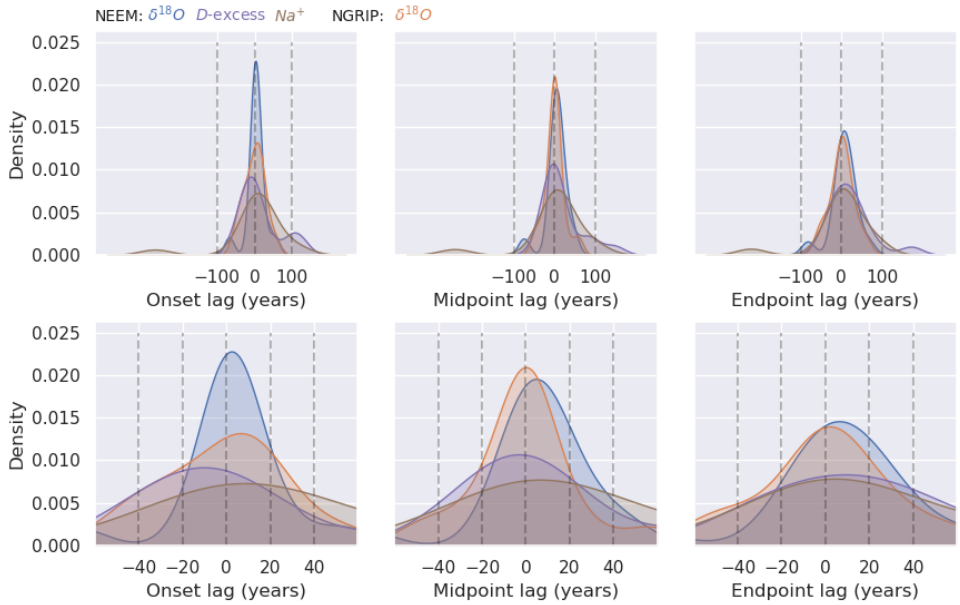

Figure 6.11: This figure is two different zooms for the bottom panels of figure 6.10. The distributions shows the lead and lag relationship to the respective ages in the Ca^{2+} record.

6.2 Age of DO events in Speleothems

Now the analysis of the $\delta^{18}O$ speleothem record from Hulu cave will be presented in comparison with the two $\delta^{18}O$ records from NEEM and NorthGRIP already presented. Table 6.2 shows the inferred midpoint ages for the Hulu record, found in this study, together with reference ages from Buizert et al. (2015). The table also includes the slopes for the linear fits in figure 6.14.

Figure 6.12 shows the three $\delta^{18}O$ records from three different locations. The yellow lines and the black dots corresponds to the inferred midpoints and half height signal value $y_0 + \frac{\Delta y}{2}$, similarly to figure 6.1. The midpoint ages of the transitions in the two ice cores are very close together, however they do not align with several of the Hulu midpoint ages. The four DO events (14, 15.1, 15.2, 16.1) are not included as they display unclear features in the speleothem record.

The inferred parameters in the ice cores are the same values presented in the previous section and will not be reintroduced here.

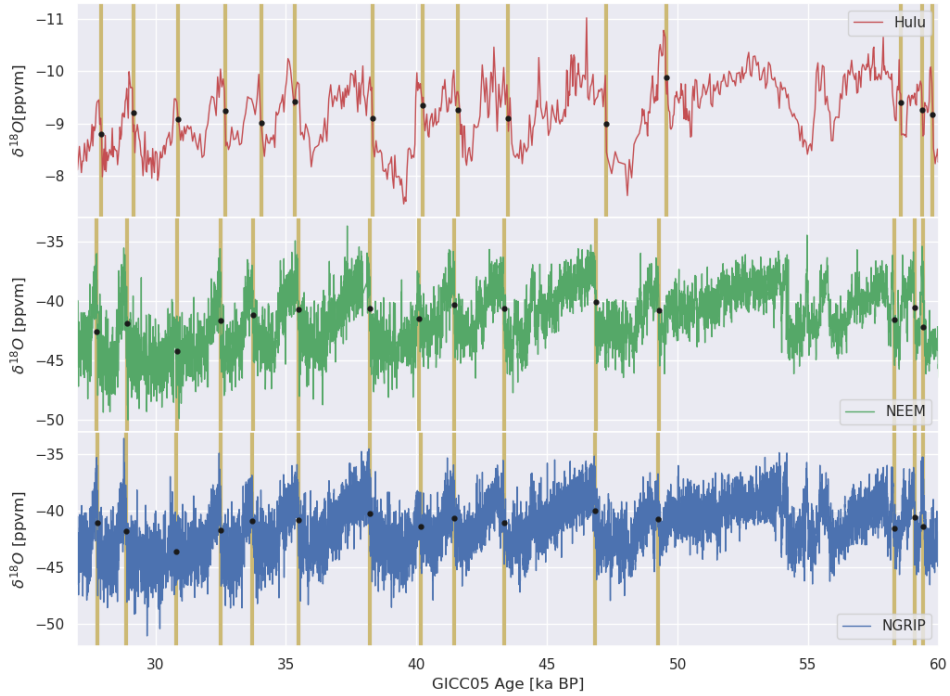

Figure 6.12: The plot shows the three $\delta^{18}O$ records analyzed in this thesis from Hulu (Red), NEEM (Green), and NorthGRIP (Blue). The vertical yellow lines shows the fitted midpoints for each of the investigated transitions. The black dots are also placed at the fitted midpoint with the inferred height $y_0 + \frac{\Delta y}{2}$.

6.2.1 Hulu

The next figure shows an analysis similar to that introduced in section 6.1, but for the Hulu speleothem data set. This analysis uses the same setup as the one used in the ice-core analysis. Each run uses two MCMC chains with 6000 draws during tuning and a 1000 draws for the posterior distributions. The figure shows the 15 events in separate panels with a time window covering manually selected for each event. The priors are given in chapter 5.

Figure 6.13 shows the analysis of the $\delta^{18}O$ Hulu record. Each panel contains the fitted data, an ensemble of the posterior 1σ solutions for two chains indicated by thin red and green lines, respectively, a mean fit solution for each chain indicated by thick lines of similar colors, and three vertical cyan lines, where the two dotted

DO-event	This Study	Buizert
	Hulu $\delta^{18}O$	Hulu $\delta^{18}O$
no.	ka	ka
3	27.916±0.056	27.922±0.078
4	29.15±0.138	29.134±0.042
5.1	30.883±0.097	30.876±0.074
5.2	32.663±0.058	32.667±0.042
6	34.068±0.144	34.034±0.072
7	35.331±0.468	35.532±0.04
8	38.311±0.032	38.307±0.038
9	40.244±0.14	40.264±0.084
10	41.593±0.255	41.664±0.054
11	43.499±0.533	43.634±0.052
12	47.258±0.023	47.264±0.04
13	49.566±0.065	49.562±0.104
16.2	58.54±0.034	58.545±0.044
17.1	59.367±0.02	59.364±0.036
17.2	59.768±0.014	59.772±0.046

Slope		
This Study		Buizert
NEEM	NGRIP	NGRIP
0.0048	0.0047	0.0063

Table 6.2: The upper table shows the resulting midpoint age and 2σ uncertainty analyzed in the Hulu speleothem record for the 15 DO events. The last column shows the results from Buizert et al. (2015). The lower table shows the slopes for the linear fits in figure 6.14.

lines show the fitted midpoints for the two chains, and the full line shows the reference age determined in Buizert et al. (2015). The data signal has a noticeably smaller resolution than the ice-core records analyzed above. All records appear to successfully find and describe the respective transitions, and the posterior solutions all appear representative of the data signal.

The inferred midpoint ages are all in agreement with the reference ages in Buizert et al., 2015. DO-event 7 is the transition with largest difference between the inferred midpoint age and reference age.

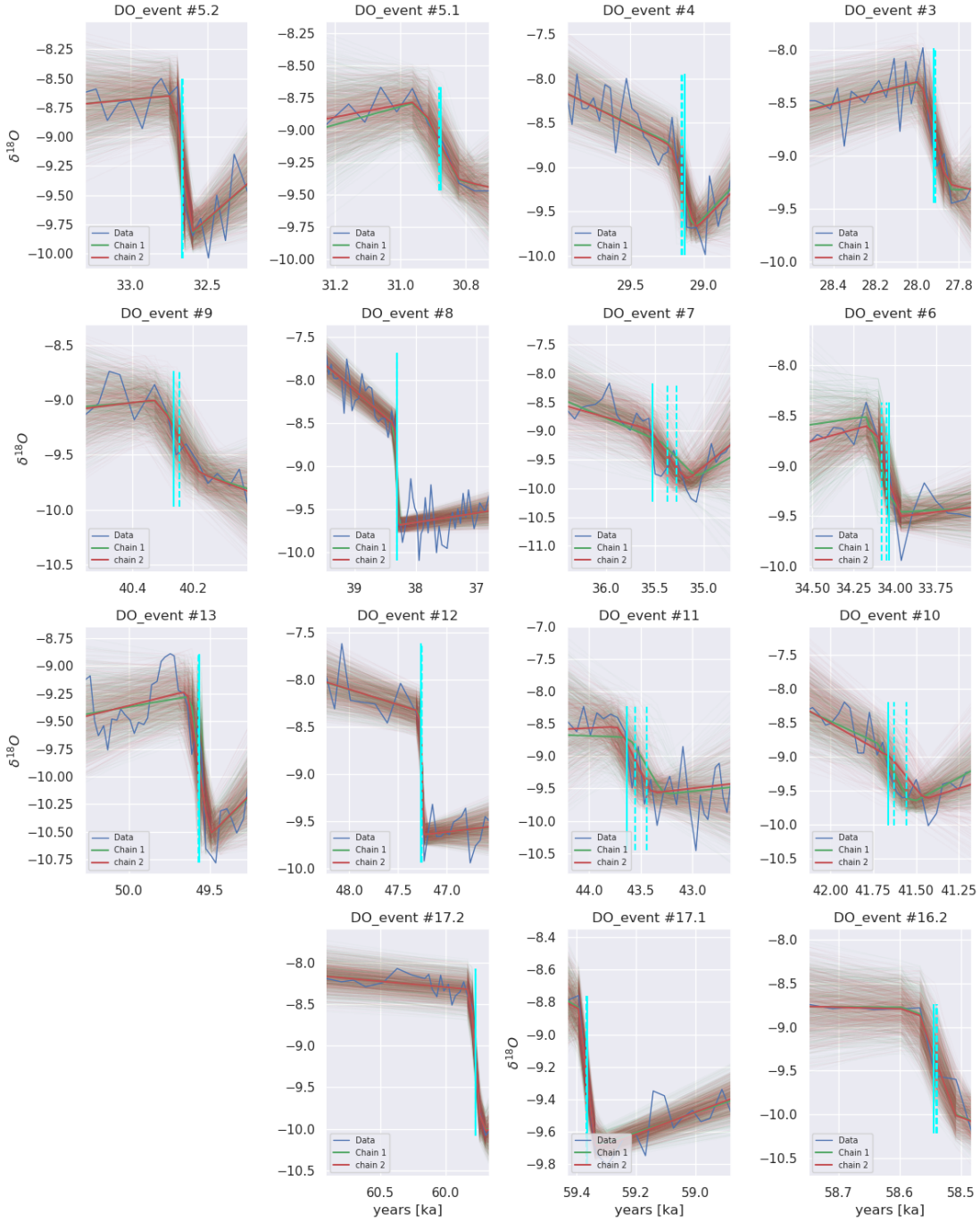

Figure 6.13: The plot shows the result of the IRFM for the $\delta^{18}O$ Hulu record. The posterior fits (transparent) as well as a mean posterior fit (bright color) are displayed as the red and green lines for the two chains, respectively. The cyan lines are the mean midpoint for each chain (dashed) and the ages from Rasmussen et al. (2014) (full).

6.2.2 Comparing Hulu, NEEM and NGRIP

The analysis of the Hulu speleothem record is now compared to the analysis of the two ice cores from NEEM and NorthGRIP. In the study by Buizert et al. (2015) the Hulu midpoint ages were compared to the NorthGRIP midpoint ages in order to synchronize the two records. The study found a scaling factor of 1.0063 between the NorthGRIP ages and the Hulu ages.

Figure 6.14 shows a comparison of the midpoint ages between the three $\delta^{18}O$ records. Each point is plotted as the age in the ice-core record versus the difference in age between the respective ice-core record and the Hulu record. Following Buizert et al. (2015), a linear fit is made through the data points, forced to intersect the origin, thus the lines are of the form:

$$y - x = a \cdot x \Rightarrow y = (a + 1) \cdot x \tag{6.1}$$

The red dots and line are the results of the analysis by Buizert et al. (2015), where the slope of the line is 0.0063 and the ice-core ages are calculated from the NorthGRIP ice core. The uncertainties are calculated as the root sum square of the NorthGRIP and Hulu midpoint age uncertainty (Buizert et al., 2015). The analysis and results of this study are plotted with the orange and blue points which corresponds to NEEM and NorthGRIP, respectively.

The orange and blue line are almost similar with slope values of 0.0048 for NEEM and 0.0047 for NorthGRIP. The uncertainties of Buizert et al. (2015) are generally smaller than the uncertainties inferred from the analysis in this study.

For all except two of the DO events, the red, yellow, and blue points fall inside the uncertainties. The exception is DO-event 12 where the uncertainty for all three ages are relatively small and DO-event 8 where the blue and red points fall outside of the uncertainties. The largest uncertainties is for DO-event (7, 11) which is consistent for both NEEM and NorthGRIP.

As noted by Buizert et al. (2015) the age difference between the NEEM and NorthGRIP ice cores and the Hulu record is smaller than the ice core counting error (which ranges from 832 to 2573 years) (Rasmussen et al., 2006; Svensson et al., 2006; Wolff et al., 2010) and larger than the Hulu age uncertainty (92 to 366 years)

(Wang et al., 2001) for the specific age range we are investigating. They suggested that the difference in age is caused by missing years in the GICC05 annual layer counting (missing 6.3 out of every 1000 layers).

On figure 6.15 a visualization of the inferred midpoint ages and transition lengths for the three $\delta^{18}O$ records is shown relative to the inferred midpoint ages from NorthGRIP, with the distribution for the inferred points in the bottom panels. For the two middle columns, the ice-core ages are scaled linearly by the respective slopes determined by the linear fits in figure 6.14 and listed in table 6.2. In the two rightmost columns the ice core ages are shifted uniformly by a constant value equal to the mean of the age differences to Hulu from NEEM and NorthGRIP, respectively, i.e. the distribution of the midpoint age difference between Hulu and NorthGRIP is shifted to align around zero. The shifts are calculated as the gray dashed lines in figure 6.14, which represents the mean y-values for the NEEM and NorthGRIP age differences to Hulu. Note that the uniform scalar shift does not change the transition durations.

Figure 6.16 shows the two corrections for all three records plotted together. In the top figure the ice core records are corrected by the linear scaling, and in the bottom figure the ice core records are corrected by a uniform shift.

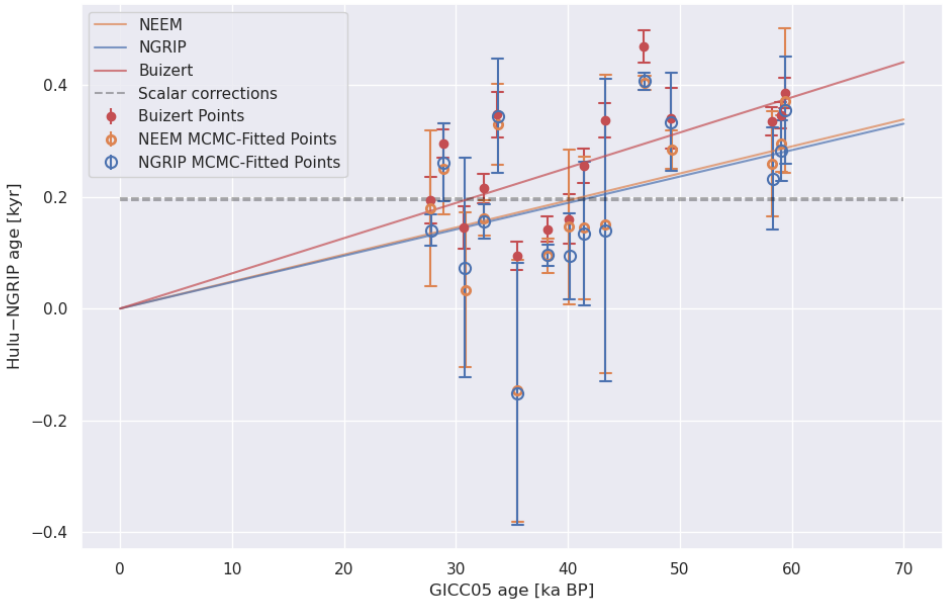

Figure 6.14: The plot shows a comparison between the ice-core ages and the Hulu ages of the transitions. The orange and blue points are from this study and the red points are from Buizert et al., 2015. The lines are linear fits forced to go through origin. The grey lines are the mean of the differences between Hulu, and NorthGRIP and NEEM respectively.

6.2.3 Summarising remarks

Figure 6.15 shows two different corrections for the inferred ice-core midpoint ages and transitions. Both correction methods shifts the distribution of the midpoint lag for the Hulu record relative to NorthGRIP to be distributed around zero.

The uniform shift does not change the shape of the distribution for the Hulu midpoint lag but the scaling correction changes the distribution to be sharper. This could suggest that the scaling correction works better. It can also be seen on figure 6.15 that there is a trend in the midpoint lag between the younger and older events for the uniformly shifted correction. Furthermore, figure 6.14 also shows that the linearly scaling correction better captures the age differences of the midpoints between ice cores and Hulu, compared to the uniformly scaling method. A linear scaling factor suggest that the annual layer counting consequently misses

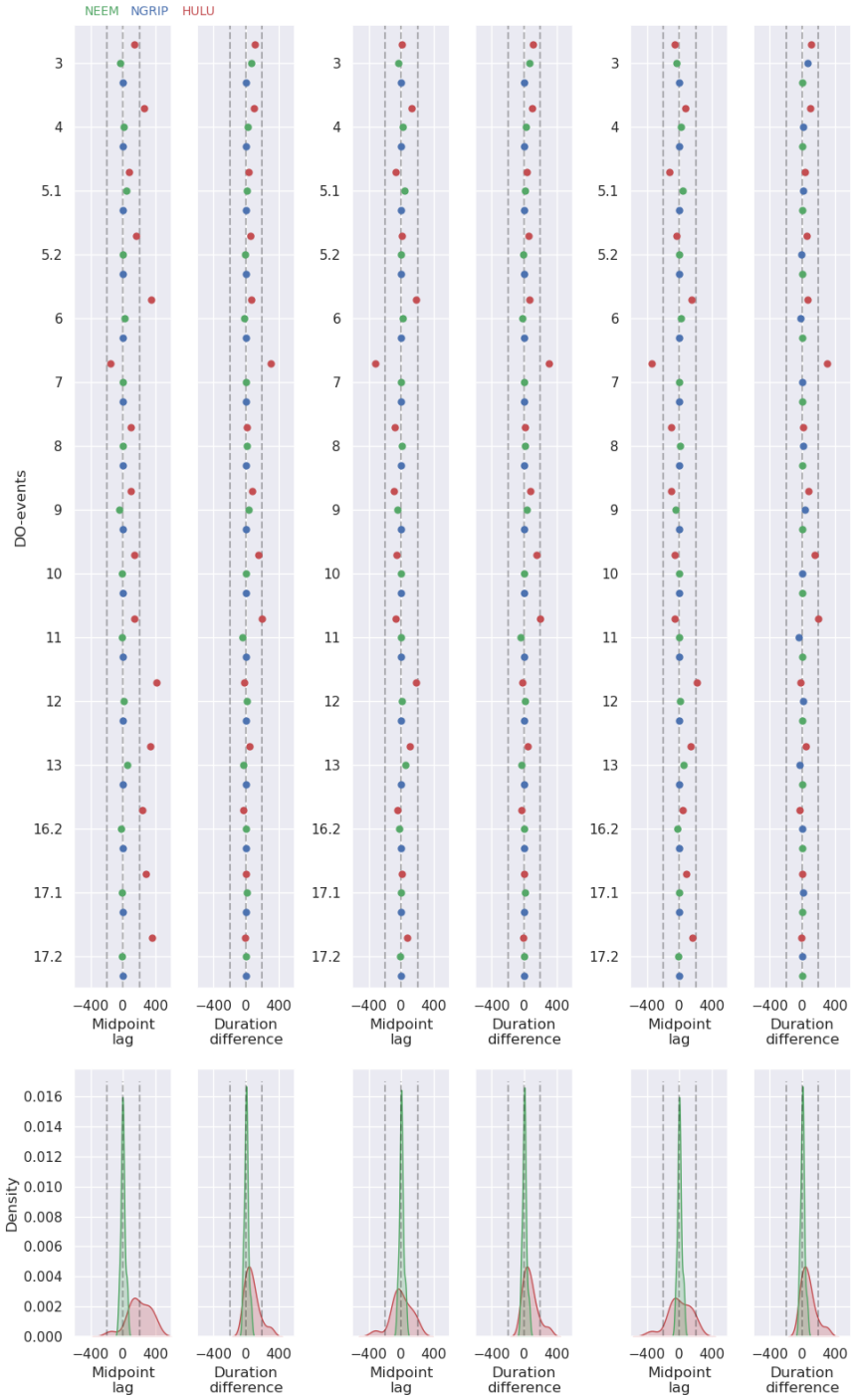

Figure 6.15: The plot shows the midpoints and transitions length for each DO-event in the three $\delta^{18}O$ records. The two left columns are the unchanged results, the two middle columns are scaled for the ice-core ages with the respective slopes from 6.2, and the two rightmost columns show a scalar correction of the ice-core ages. The dashed lines are placed at ±200 years.

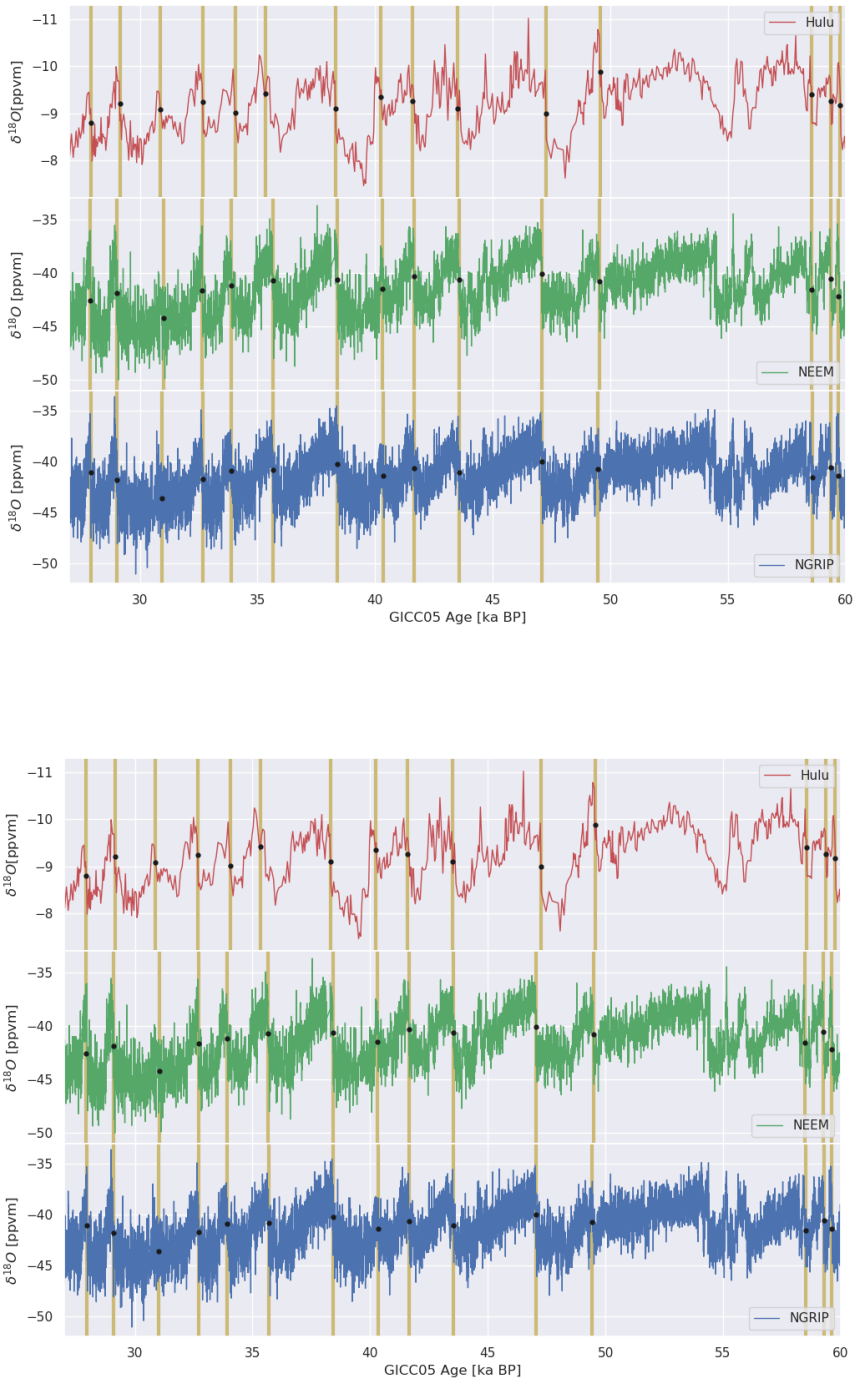

Figure 6.16: shows the two corrections for all three records plotted together. In the top figure the ice-core records are corrected by the linear scaling, and in the bottom figure the ice-core records are corrected by a uniform shift.

years with a constant error rate. A uniform shift could suggest that an interval, younger than investigated in this study, misses some years in the counting, but that there are no further errors accumulating. This was discussed by Adolphi et al. (2018) and Sinnl et al. (2022), see discussion.

Chapter 7

Discussion

This chapter will discuss the different results in order to answer the three research questions listed in the introduction. Each research question is discussed in the separate sections below.

7.1 Model stability

The IRFM is tested against surrogate data. Based on the tests conducted in this thesis, the IRFM appears to have no problem fitting the surrogate data with sampling rates similar to ice core records. In test 2 where the original RFM was used, the results for the midpoint were not affected, but it is clear that the model struggles to find the proper anatomy of the ramp in regards to height and duration. As the test does not investigate the window size, it is unknown if the mid point or duration would significantly change, as reported in Capron et al. (2021), when narrowing or widening the search window.

With the new sampling method and signal model the IRFM only uses 6000 draws to converge, and then sampled 1000 samples per chain resulting in 14000 total samples drawn. The RFM used in Erhardt et al. (2019) used 60000 iterations and saved every 600th sample for the posterior. With 60 chains this result in a larger posterior but also requires a much larger total sample size of 3.6 million draws. This corresponds to a 99.62% reduction in sample size per transition when using the IRFM. For the RFM used by Capron et al. (2021), where they used a total

of 1 million sample per chain and 3 chains, there is a reduction of 99.54% per transition.

With regards to research question 3, the general results of the tests shows that for sampling rates $\leq$ 30 samples/kyear, some of the model parameters display a general bias towards larger values (σ, τ, Δt, y_0, $s1$, $s2$) or smaller values (Δy). Although this bias is not present in the midpoint, the duration is affected, meaning the resulting onset is affected. The 1σ uncertainties is, however, on the order of 90 years for a sample rate of 20 samples/kyear, rivaling the duration of the transition of 100 years. Although the uncertainties seems large, this means that the onset of the duration can be determined with uncertainty $\pm 2\delta t$ compared to the resolution, and the method can be accepted with regard to the low sampling rate.

Looking at the mean posterior solution plotted in the results for Hulu cave (figure 6.13), it is clear that there are larger variations for the accepted 1σ posterior samples in Hulu compared to the ice cores, with the spread visible for the levels y_0 and Δy. However, the mean solution does not appear wrong with regards to the duration Δt. The reason for the model to do worse when tested on surrogate data, might suggest that the constructed surrogate data representing the speleothem records could be improved.

When updating the priors, it had no effect for the surrogate data with ice core like sampling rate, but drastically improved the estimation for τ for the data with the speleothem like sampling rate. Even though the noise model parameters should be treated as nuisance parameters, as mentioned by Erhardt et al. (2019), a better (smaller) estimate for τ can have a large impact for the fit, as it has a huge impact on the allowed variations for the posterior results. The model subtracts the proposed signal from the data and then test the residuals ($y - data$) against the error model (line 45-50 in the code on figure 4.3). Thus a large τ will allow the noise model to have sinus like oscillations, as illustrated in the red noise on figure 5.3. It is definitely the most common case, when the model misfits, that τ is estimated to be too large. This is also supported from figure 6.9, panel E.

7.2 Phasing of Abrupt Change

The IRFM works well for ice core records, and it is clear that several DO events show features corresponding to non-zero slopes for both $s1$ and $s2$ (see DO event 11 on figure 6.5; 5.1, 13 on figure 6.4; 3, 9 on figure 6.7. The aerosol records (Na^+, Ca^{2+}) have smaller variations and more well defined transitions, which result in the clear grouping of water isotope records (blue, green) and aerosol records (red, orange) on figure 6.9, panel C-E.

The fitted mean posterior solutions shows some outlier events related to misfits where the search window for the transition is too large, meaning for DO events that features from two DO events in rapid succession are present in the search window. Ultimately, this changes the fundamental structure of the signal (from two to three breakpoints) and thus the model is poorly represented. Modifying these search windows should eliminate all misfits, and is a natural next step in the analysis. In the study by Capron et al. (2021) they mention that some DO events are disregarded due to large variations in the result when changing the search window. This does not refer to the above mentioned problem in this study, but refers to DO events with large slopes.

The study by Capron et al. (2021) reports no systematical patterns between the anatomy of different DO events. The results in this study supports that claim, as there exist no linear relationship for the tested (figure 6.9, panel A-F), meaning they are different samples originating from the same stochastic process or mechanism. There is a strong correlation in the uncertainties for the model parameters (t_{mid} and δt, y_0 and Δy, see figure 6.9, panel G-H), however this only refers to the correlations discussed in test 1b (subsection 5.3.2, figure 5.5). If any extra comparison should be added to figure 6.9, it should be a comparison between the midpoint t_mid and either the duration Δt, the initial level y_0, or the ramp height Δy to reveal if there are any general evolution over the course of the ice age.

The analysis of lead and lag relationships (figure 6.1, 6.11) between the different ice core records are compared to the result in Erhardt et al. (2019), shown on figure 7.1. The λ record and D-excess records are not accounted for in the comparison, and will be addressed afterwards. In general the two Ca^{2+} records are synchronised within a few years as they both display small differences to the age determined

in Rasmussen et al. (2014) (figure 6.2), which is in agreement with Erhardt et al. (2019) that shows around 1 year lead in NEEM. For the onset of the transition Erhardt et al. (2019) finds that on average the Ca^{2+} records have a 10 year lead to the Na^{+} and $\delta^{18}O$ records, which are synchronized. Although it is not as clear with the more wide distributions on figure 6.11, on average the Ca^{2+} records also have a lead of 10 years to the NEEM Na^{+} and NorthGRIP $\delta^{18}O$ records. However, the average lead to the NEEM $\delta^{18}O$ record is only 5 years. Notice here, that Erhardt et al. (2019) directly fits the onset in the original RFM, where the IRFM has to calculate the onset from the inferred midpoint and duration, and the uncertainty in the duration is significantly larger than the uncertainty in the midpoint (figure 6.9, panel G) (however, these plots do not show the uncertainty in the posterior distributions). The densities in this study are larger around the mean values in this study, meaning the wider distributions arise from the outliers and misfits mentioned in chapter 6.

For the midpoint, Erhardt et al. (2019) finds the same pattern as with the onset, but the NorthGRIP $\delta^{18}O$ midpoints show a slight lead of 2 years to the Na^{+} record. In this study, the NEEM Na^{+} and $\delta^{18}O$ records display a 5 year lag in the midpoint to the Ca^{2+} record and the NorthGRIP $\delta^{18}O$ record show no lag to Ca^{2+} record. Here, the results diverge slightly. Notice again, that in this case the original RFM has to calculate the midpoint from the inferred onset and duration, where the IRFM finds it directly. As shown in test 2 on figure 5.7, the duration converges to a value lower than the true value using the RFM. This means that depending on the search window chosen in Erhardt et al. (2019), the duration might have a bias towards smaller values, leading to younger midpoints. However, as the figures compare relative timings, this bias is not visible in the distributions.

For the endpoint, Erhardt et al. (2019) finds Ca^{2+} and $\delta^{18}O$ to be close to synchronous with a lead of 5 and 4 years, respectively, to the Na^{+} endpoint. This study finds that the endpoints for NEEM $\delta^{18}O$ and Na^{+} show a 5 year lag to NorthGRIP $\delta^{18}O$ and both Ca^{2+} records. The small lead-lag relationships of $\leq$ 10 years between the aerosol and water isotope records suggests a tight coupling between the Asian and North Atlantic climate.

The λ record show a large relative lead of 10, 16, and 12 years for the onset, midpoint and endpoint respectively to the Na^{2+} records. Similarly, the D-excess

records shows 10 years lead, synchronicity, and 10 years lag for the onset, midpoint and endpoint, respectively, to the Ca^{2+}. These relatively large leads for λ and D-excess suggests a significant change in the sub-tropical source region, leading to increased amounts of precipitation preceding the DO event. The lag for D-excess at the endpoint means the transition is longer and the sub-tropical changes continues after the DO event ends in the North Atlantic.

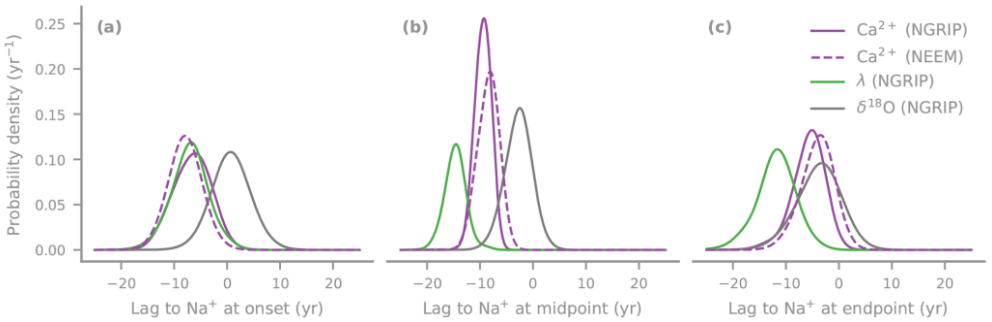

Figure 7.1: This figure and figure text is from Erhardt et al. (2019). Combined probability density estimates of the lag of the Ca^{2+}, layer thickness and $\delta^{18}O$ transitions relative to the respective point in the Na^{+} records for the onset (a), midpoint (b) and end (c) of all transitions from stadial to interstadial for the two cores.

The study by Capron et al. (2021) warns against drawing conclusions based on a stacking of the DO events, as they display large variations from event to event. The variations in the distributions in this study are quite large (possibly due to outliers) to support stacking the events. However, the densities are larger around the mean values, further suggesting that the outliers are widening the distribution, but the majority of transitions are grouped together.

With respect to research question 1, results for the onset of the transitions regarding lead and lag is found, supporting the idea of a sequence in the onset age for the ice core parameters at DO events. The largest leads and lags observed is for D-excess which unfortunately cannot be compared to the study by Erhardt et al. (2019). The leads and lags can only be obtained by stacking the DO events.

7.3 Synchronous Abrupt Events

The IRFM works well for the speleothem data set, finding all transitions with no misfits. The search window here is carefully selected as there are large variations in the stadial and interstadial duration compared to the Greenland ice cores. In most cases the ages agree with the study by Buizert et al. (2015), the largest difference in the methods is the duration of the events. The method in Buizert et al. (2015) determines the level before and after the event from a 50 years and a 150 years window, respectively. The midpoint is then found as the age of where the signal reaches half of the ramp height. The duration is defined much smaller than the one inferred by the IRFM for all transitions, where the ages disagree. Additionally, the ramps where the age disagree, are all characterised by large variations on the ramp resulting in a two step ramp. Here Buizert et al. (2015) chooses the last of the two ramps, where the IRFM see the two steps as one ramp with large variations in the noise.

The study by Buizert et al. (2015) suggests a linear correction of 0.0063 for the GICCO5 timescale based on age differences between DO events in the NorthGRIP and Hulu $\delta^{18}O$ records. This study also finds significant differences in the ages between the two records, and additionally between the Hulu and NEEM $\delta^{18}O$ records. The ages in the NEEM and NorthGRIP records agree, and thus the two linear corrections are almost identical at 0.0048 and 0.0047 for NEEM and NorthGRIP, respectively. The linear correction can be supported as a systematic miscounting error of 6.3 years per 1000 layers counted. The reason for changing the GICCO5 scale and not the U/Th is due to the absolute dating error for Hulu being significantly smaller than the maximum counting error (MCE) of the ice core dating. On the contrary, two independent studies suggests the GICCO5 timescale misses layers over two different ranges. The study by Adolphi et al. (2018) suggests that the GICCO5 has a growing error compared to the U/Th timescale, peaking at around 22 ka BP with a difference of 500 years. The more recent study by Sinnl et al. (2022) suggests that the GICCO5 timescale is missing about 13 years 3.8 ka BP. This would suggest, that a scalar correction corresponding to a miscounting in a specific age interval, would be a better correction. The scalar correction found here is estimated to be about 200 years, which is close to the suggested correction in Adolphi et al. (2018) for the 27-60 ka BP range.

In respect to research question 2, the correction of the GICCO5 timescale is only necessary assuming that DO events in ice cores and speleothems are synchronous. Otherwise, this would suggests a 200 year lag between ages for DO events in ice cores compared to speleothems. However, the resulting lead and lags of only about 10 years for the aerosols record in the ice core contradicts a lag of 200 years for the Asian atmospheric climate. Thus, the results suggest that the GICCO5 timescale have to be corrected to match the U/Th timescale.

Chapter 8

Conclusion

This chapter will summarise the conclusions drawn from the analysis and discussion, including climatic perspectives of the results.

In this thesis, the Improved Ramp Fitting Method has been developed, tested, and applied to paleoclimatic records from ice cores and speleothems in order to investigate abrupt DO transitions during the last glacial period (27-60 ka BP).

Tt has been shown that the Improved Ramp Fitting Method is a computational and methodological improvement compared to the original Ramp Fitting Method. The method works well for ice core records as well as speleothem records, with regards to desired parameters (t_{mid}, Δt) that are used to characterize the age of abrupt climate transitions. The computational improvements are on the order of 99%, while the inferred model parameters give consistent results compared to the original model.

The method is tested and is concluded to be sensitive to changes in the prior for the auto-correlation time τ, as well as the sampling rate δt of the data set. The lower limit for the sampling rate is 20 samples/year, as lower sample rates result in large uncertainties, that render the results inconclusive.

In this thesis a multi-tracer study of four different proxy records ($\delta^{18}O$, D-excess, Na^{+}, Ca^{2+}) from the two Greenland deep ice cores NEEM and NorthGRIP was conducted in order to date DO events from the last glacial period. The resulting analysis revealed a chronological order for the four ice core parameters measured,

when stacking the DO events to calculate average lead and lags between the transition onsets, midpoints, and endpoints. The analysis found leads and lags of up to 10 years, and for the onset of the transitions, D-excess shows a lead of 10 years to Ca^{2+}, which in turn shows a lead of 5 years to NEEM $\delta^{18}O$, and 10 years to NorthGRIP $\delta^{18}O$ and NEEM Na^{+}. The IRFM fails to fit events where the search window are poorly chosen resulting in outliers. Better chosen search windows would improve these results, and would be a natural next step in the analysis.

Furthermore, A $\delta^{18}O$ speleothem record from the Hulu cave located in China was analyzed in this thesis. Here, the IRFM was again applied to find DO ages in the speleothem record. The resulting analysis find an age difference of 200 years on average between the DO event ages determined in the Hulu, NEEM and NorthGRIP $\delta^{18}O$ records. Using the gained knowledge from the ice core analysis, the 200 year age difference was estimated to be a dating error between the U/Th and GICCO5 timescales. This resulted in two possible proposed corrections: a linear scaling correction of the GICCO5 timescale by 1.0048 and 1.0047 for NEEM and NorthGRIP, respectively, or a uniform shift of 200 years. The uniform shift was supported by recent studies, but the magnitude of the shift may vary depending on the age range investigated. Thus the timing differences between ice cores and speleothems are due to errors in the timescale(s),as there is most evidence for the speleothem and ice-core records being synchronous with up to a 10 year lead of the speleothems.

Bibliography

Adolphi, F., Bronk Ramsey, C., Erhardt, T., Edwards, R. L., Cheng, H., Turney, C. S. M., Cooper, A., Svensson, A., Rasmussen, S. O., Fischer, H., & Muscheler, R. (2018). Connecting the greenland ice-core and u/th timescales via cosmogenic radionuclides: Testing the synchroneity of dansgaard–oeschger events. *Climate of the past*, *14*(11), 1755–1781.

Andersen, Azuma, N., Barnola, J., Bigler, M., Biscaye, P., Caillon, N., Chappellaz, J., Clausen, H., DahlJensen, D., Fischer, H., Fluckiger, J., Fritzsche, D., Fujii, Y., Goto-Azuma, K., Gronvold, K., Gundestrup, N., Hansson, M., Huber, C., Hvidberg, C., ... Project, N. G. I. C. (2004). High-resolution record of northern hemisphere climate extending into the last interglacial period. *NATURE*, *431*(7005), 147–151. https://doi.org/10.1038/nature02805

Andersen, K. K., Svensson, A., Johnsen, S. J., Rasmussen, S. O., Bigler, M., Röthlisberger, R., Ruth, U., Siggaard-Andersen, M.-L., Peder Steffensen, J., Dahl-Jensen, D., Vinther, B. M., & Clausen, H. B. (2006). The greenland ice core chronology 2005, 15–42 ka. part 1: Constructing the time scale. *Quaternary science reviews*, *25*(23), 3246–3257.

Betancourt, M. (2017). A conceptual introduction to hamiltonian monte carlo. http://arxiv.org/licenses/nonexclusive-distrib/1.0

Blunier, T., & Brook, E. (2001). Timing of millennial-scale climate change in antarctica and greenland during the last glacial period. *SCIENCE*, *291*(5501), 109–112. https://doi.org/10.1126/science.291.5501.109

Blunier, T., Chappellaz, J., Schwander, J., Dallenbach, A., Stauffer, B., Stocker, T., Raynaud, D., Jouzel, J., Clausen, H., Hammer, C., & Johnsen, S. (1998). Asynchrony of antarctic and greenland climate change during the

last glacial period. *NATURE*, *394*(6695), 739–743. https://doi.org/10.1038/29447

Boers, N. (2021). Observation-based early-warning signals for a collapse of the atlantic meridional overturning circulation. *NATURE CLIMATE CHANGE*, *11*(8), 680+. https://doi.org/10.1038/s41558-021-01097-4

Bond, G., Heinrich, H., Broecker, W., Labeyrie, L., McManus, J., Andrews, J., Huon, S., Jantschik, R., Clasen, S., Simet, C., Tedesco, K., Klas, M., Bonani, G., & Ivy, S. (1992). Evidence for massive discharges of icebergs into the north atlantic ocean during the last glacial period. *Nature (London)*, *360*(6401), 245–249.

Brauer, A., Hajdas, I., Blockley, S. P. E., Ramsey, C. B., Christl, M., Ivy-Ochs, S., Moseley, G. E., Nowaczyk, N. N., Rasmussen, S. O., Roberts, H. M., Spoetl, C., Staff, R. A., & Svensson, A. (2014). The importance of independent chronology in integrating records of past climate change for the 60-8 ka intimate time interval. *QUATERNARY SCIENCE REVIEWS*, *106*(SI), 47–66. https://doi.org/10.1016/j.quascirev.2014.07.006

Buizert, C., Cuffey, K. M., Severinghaus, J. P., Baggenstos, D., Fudge, T. J., Steig, E. J., Markle, B. R., Winstrup, M., Rhodes, R. H., Brook, E. J., Sowers, T. A., Clow, G. D., Cheng, H., Edwards, R. L., Sigl, M., McConnell, J. R., & Taylor, K. C. (2015). The wais divide deep ice core wd2014 chronology – part 1: Methane synchronization (68–31 ka bp) and the gas age–ice age difference. *Climate of the past*, *11*(2), 153–173.

Capron, E., Rasmussen, S. O., Popp, T. J., Erhardt, T., Fischer, H., Landais, A., Pedro, J. B., Vettoretti, G., Grinsted, A., Gkinis, V., Vaughn, B., Svensson, A., Vinther, B. M., & White, J. W. C. (2021). The anatomy of past abrupt warmings recorded in greenland ice. *Nature communications*, *12*(1), 2106–2106.

Cheng, H., Edwards, R. L., Sinha, A., Spotl, C., Yi, L., Chen, S., Kelly, M., Kathayat, G., Wang, X., Li, X., Kong, X., Wang, Y., Ning, Y., & Zhang, H. (2016). The asian monsoon over the past 640,000 years and ice age terminations. *NATURE*, *534*(7609), 640+. https://doi.org/10.1038/nature18591

Corrick, E. C., Drysdale, R. N., Hellstrom, J. C., Capron, E., Rasmussen, S. O., Zhang, X., Fleitmann, D., & Couchoud, I. (2020). Synchronous timing of

abrupt climate changes during the last glacial period. *Science (American Association for the Advancement of Science)*, *369*(6506), 963–969.

Cuffey, K., & Paterson, W. (2010). *The physics of glaciers* (4. ed.). Butterworth-Heinemann/Elsevier.

Dahl-Jensen, D., Albert, M. R., Aldahan, A., Azuma, N., Balslev-Clausen, D., Baumgartner, M., Berggren, A. .-M., Bigler, M., Binder, T., Blunier, T., Bourgeois, J. C., Brook, E. J., Buchardt, S. L., Buizert, C., Capron, E., Chappellaz, J., Chung, J., Clausen, H. B., Cvijanovic, I., ... Community, N. (2013). Eemian interglacial reconstructed from a greenland folded ice core. *NATURE*, *493*(7433), 489–494. https://doi.org/10.1038/nature11789

Dansgaard, W. (1964). Stable isotopes in precipitation. *TELLUS*, *16*(4), 436–468.

Dansgaard, W., Clausen, H. B., Gundestrup, N., Hammer, C. U., Johnsen, S. F., Kristinsdottir, P. M., & Reeh, N. (1982). A new greenland deep ice core. *Science (American Association for the Advancement of Science)*, *218*(4579), 1273–1277.

Dansgaard, W., JOHNSEN, S., CLAUSEN, H., DAHLJENSEN, D., GUNDESTRUP, N., HAMMER, C., HVIDBERG, C., STEFFENSEN, J., SVEINBJORNSDOTTIR, A., JOUZEL, J., & BOND, G. (1993). Evidence for general instability of past climate from a 250-kyr ice-core record. *NATURE*, *364*(6434), 218–220. https://doi.org/10.1038/364218a0

Dansgaard, W., JOHNSEN, S., MOLLER, J., & LANGWAY, C. (1969). One thousand centuries of climatic record from camp century on greenland ice sheet. *SCIENCE*, *166*(3903), 377+. https://doi.org/10.1126/science.166.3903.377

Dima, M., Lohmann, G., Ionita, M., Knorr, G., & Scholz, P. (2022). Amoc modes linked with distinct north atlantic deep water formation sites. *CLIMATE DYNAMICS*, *59*(3-4), 837–849. https://doi.org/10.1007/s00382-022-06156-w

Erhardt, T., Capron, E., Rasmussen, S. O., Schüpbach, S., Bigler, M., Adolphi, F., & Fischer, H. (2019). Decadal-scale progression of the onset of dansgaard–oeschger warming events. *Climate of the past*, *15*(2), 811–825.

Gkinis, V., Simonsen, S., Buchardt, S., White, J., & Vinther, B. (2014). Water isotope diffusion rates from the northgrip ice core for the last 16,000 years – glaciological and paleoclimatic implications. *Earth and planetary science letters*, *405*, 132–141.

Goosse, H. (2015). *Climate system dynamics and modeling*. Cambridge University Press.

Gulev, S., Thorne, P., Ahn, J., Dentener, F., Domingues, C., Gerland, S., Gong, D., Kaufman, D., Nnamchi, H., Quaas, J., Rivera, J., Sathyendranath, S., Smith, S., Trewin, B., von Schuckmann, K., & Vose, R. (2021). Changing state of the climate system. In V. Masson-Delmotte, P. Zhai, A. Pirani, S. Connors, C. Péan, S. Berger, N. Caud, Y. Chen, L. Goldfarb, M. Gomis, M. Huang, K. Leitzell, E. Lonnoy, J. Matthews, T. Maycock, T. Waterfield, O. Yelekci, R. Yu, & B. Zhou (Eds.), *Climate change 2021: The physical science basis. contribution of working group i to the sixth assessment report of the intergovernmental panel on climate change* (pp. 287–422). Cambridge University Press. https://doi.org/10.1017/9781009157896.004

Hawkins, E., Smith, R. S., Allison, L. C., Gregory, J. M., Woollings, T. J., Pohlmann, H., & de Cuevas, B. (2011). Bistability of the atlantic overturning circulation in a global climate model and links to ocean freshwater transport. *GEOPHYSICAL RESEARCH LETTERS*, *38*. https://doi.org/10.1029/2011GL047208

Hoffman, M. D., & Gelman, A. (2014). The no-u-turn sampler: Adaptively setting path lengths in hamiltonian monte carlo. *Journal of machine learning research*, *15*, 1593–1623.

IPCC. (2021). *Climate change 2021: The physical science basis. contribution of working group i to the sixth assessment report of the intergovernmental panel on climate change* (Vol. In Press). Cambridge University Press. https://doi.org/10.1017/9781009157896

J Salvatier, C. F., TV Wiecki. (2016). Probabilistic programming in python using pymc3. *PeerJ Computer Science*, *2*(55), 22–46. https://doi.org/https://doi.org/10.7717/peerj-cs.55

Johnsen, S. J., Clausen, H. B., Dansgaard, W., Fuhrer, K., Gundestrup, N., Hammer, C. U., Iversen, P., Jouzel, J., Stauffer, B., & steffensen, J. P. (1992). Irregular glacial interstadials recorded in a new greenland ice core. *Nature (London)*, *359*(6393), 311–313.

Jouzel, J., Masson-Delmotte, V., Cattani, O., Dreyfus, G., Falourd, S., Hoffmann, G., Minster, B., Nouet, J., Barnola, J. M., Chappellaz, J., Fischer, H., Gallet, J. C., Johnsen, S., Leuenberger, M., Loulergue, L., Luethi, D., Oerter,

H., Parrenin, F., Raisbeck, G., ... Wolff, E. W. (2007). Orbital and millennial antarctic climate variability over the past 800,000 years. *Science (American Association for the Advancement of Science)*, *317*(5839), 793–796.

Lohmann, J., & Svensson, A. (2022). Ice core evidence for major volcanic eruptions at the onset of dansgaard–oeschger warming events. *Climate of the Past*, *18*(9), 2021–2043. https://doi.org/10.5194/cp-18-2021-2022

Markle, B. R., Steig, E. J., Buizert, C., Schoenemann, S. W., Bitz, C. M., Fudge, T. J., Pedro, J. B., Ding, Q., Jones, T. R., White, J. C., & Sowers, T. (2017). Global atmospheric teleconnections during dansgaard-oeschger events. *NATURE GEOSCIENCE*, *10*(1), 36–40. https://doi.org/10.1038/NGEO2848

Pedro, J. B., Andersson, C., Vettoretti, G., Voelker, A. H. L., Waelbroeck, C., Dokken, T. M., Jensen, M. F., Rasmussen, S. O., Sessford, E. G., Jochum, M., & Nisancioglu, K. H. (2022). Dansgaard-oeschger and heinrich event temperature anomalies in the north atlantic set by sea ice, frontal position and thermocline structure. *QUATERNARY SCIENCE REVIEWS*, *289*. https://doi.org/10.1016/j.quascirev.2022.107599

Pedro, J. B., Jochum, M., Buizert, C., He, F., Barker, S., & Rasmussen, S. O. (2018). Beyond the bipolar seesaw: Toward a process understanding of interhemispheric coupling. *QUATERNARY SCIENCE REVIEWS*, *192*, 27–46. https://doi.org/10.1016/j.quascirev.2018.05.005

Rahmstorf, S. (2002). Ocean circulation and climate during the past 120,000 years. *Nature (London)*, *419*(6903), 207–214.

Rasmussen, S. O., Andersen, K. K., Svensson, A. M., Steffensen, J. P., Vinther, B. M., Clausen, H. B., Siggaard-Andersen, M.-L., Johnsen, S. J., Larsen, L. B., Dahl-Jensen, D., Bigler, M., Röthlisberger, R., Fischer, H., Goto-Azuma, K., Hansson, M. E., & Ruth, U. (2006). A new greenland ice core chronology for the last glacial termination (Rasmussen, S. O., and et. al. (2006), A new Greenland ice core chronology for the last glacial termination, J. Geophys. Res., 111, D06102, doi:10.1029/2005JD006079.). *Journal of Geophysical Research*, *111*(D6), D06102–n/a.

Rasmussen, S. O., Bigler, M., Blockley, S. P., Blunier, T., Buchardt, S. L., Clausen, H. B., Cvijanovic, I., Dahl-Jensen, D., Johnsen, S. J., Fischer, H., Gkinis, V., Guillevic, M., Hoek, W. Z., Lowe, J. J., Pedro, J. B., Popp, T., Seier-

stad, I. K., Steffensen, J. P., Svensson, A. M., ... Winstrup, M. (2014). A stratigraphic framework for abrupt climatic changes during the last glacial period based on three synchronized greenland ice-core records: Refining and extending the intimate event stratigraphy. *Quaternary science reviews*, *106*, 14–28.

Rogers, S. (2017). *A first course in machine learning*. Chapman & Hall /CRC Press.

Ruddiman, W. F. (F. (2014). *Earth's climate : Past and future* (Third edition.). W.H. Freeman; Company.

Schmittner, A. (2021). *Introduction to climate science*. Oregon State University. https://books.google.dk/books?id=F8K1zQEACAAJ

Seierstad, I. K., Abbott, P. M., Bigler, M., Blunier, T., Bourne, A. J., Brook, E., Buchardt, S. L., Buizert, C., Clausen, H. B., Cook, E., Dahl-Jensen, D., Davies, S. M., Guillevic, M., Johnsen, S. J., Pedersen, D. S., Popp, T. J., Rasmussen, S. O., Severinghaus, J. P., Svensson, A., & Vinther, B. M. (2014). Consistently dated records from the greenland grip, gisp2 and ngrip ice cores for the past 104 ka reveal regional millennial-scale delta o-18 gradients with possible heinrich event imprint. *QUATERNARY SCIENCE REVIEWS*, *106*(SI), 29–46. https://doi.org/10.1016/j.quascirev.2014.10.032

Sinnl, G., Winstrup, M., Erhardt, T., Cook, E., Jensen, C. M., Svensson, A., Vinther, B. M., Muscheler, R., & Rasmussen, S. O. (2022). A multi-ice-core, annual-layer-counted greenland ice-core chronology for the last 3800 years: Gicc21. *Climate of the past*, *18*(5), 1125–1150.

Southon, J., Noronha, A. L., Cheng, H., Edwards, R. L., & Wang, Y. (2012). A high-resolution record of atmospheric 14c based on hulu cave speleothem h82. *Quaternary Science Reviews*, *33*, 32–41. https://doi.org/https://doi.org/10.1016/j.quascirev.2011.11.022

Steffensen, J. P., Andersen, K. K., Bigler, M., Clausen, H. B., Dahl-Jensen, D., Fischer, H., Goto-Azuma, K., Hansson, M., Johnsen, S. J., Jouzel, J., Masson-Delmotte, V., Popp, T., Rasmussen, S. O., Röthlisberger, R., Ruth, U., Stauffer, B., Siggaard-Andersen, M.-L., Sveinbjörnsdóttir, A. E., Svensson, A., & White, J. W. C. (2008). High-resolution greenland ice core data show

abrupt climate change happens in few years. *Science (American Association for the Advancement of Science)*, *321*(5889), 680–684.

Stocker, T. F., & Johnsen, S. J. (2003). A minimum thermodynamic model for the bipolar seesaw. *Paleoceanography*, *18*(4). https://doi.org/https://doi.org/10.1029/2003PA000920

Svensson, A., Andersen, K. K., Bigler, M., Clausen, H. B., Dahl-Jensen, D., Davies, S. M., Johnsen, S. J., Muscheler, R., Parrenin, F., Rasmussen, S. O., Röthlisberger, R., Seierstad, I., Steffensen, J. P., & Vinther, B. M. (2008). A 60 000 year greenland stratigraphic ice core chronology. *Climate of the Past*, *4*(1), 47–57. https://doi.org/10.5194/cp-4-47-2008

Svensson, A., Andersen, K. K., Bigler, M., Clausen, H. B., Dahl-Jensen, D., Davies, S. M., Johnsen, S. J., Muscheler, R., Rasmussen, S. O., Röthlisberger, R., Peder Steffensen, J., & Vinther, B. (2006). The greenland ice core chronology 2005, 15–42 ka. part 2: Comparison to other records. *Quaternary science reviews*, *25*(23), 3258–3267.

Vasileios, G., Vinther, B., Quistgaard, T., Popp, T., Faber, A., Holme, C., et al. (2020). Neem ice core high resolution (0.05m) water isotope ratios (18o/16o, 2h/1h) covering 8-129 ky b2k. https://doi.org/10.1594/PANGAEA.925552

Vettoretti, G., Ditlevsen, P., Jochum, M., & Rasmussen, S. O. (2022). Atmospheric co2 control of spontaneous millennial-scale ice age climate oscillations. *NATURE GEOSCIENCE*, *15*(4), 300+. https://doi.org/10.1038/s41561-022-00920-7

Wang, Y., Cheng, H., Edwards, R., An, Z., Wu, J., Shen, C., & Dorale, J. (2001). A high-resolution absolute-dated late pleistocene monsoon record from hulu cave, china. *SCIENCE*, *294*(5550), 2345–2348. https://doi.org/10.1126/science.1064618

Wolff, E., Chappellaz, J., Blunier, T., Rasmussen, S., & Svensson, A. (2010). Millennial-scale variability during the last glacial: The ice core record [Vegetation Response to Millennial-scale Variability during the Last Glacial]. *Quaternary Science Reviews*, *29*(21), 2828–2838. https://doi.org/https://doi.org/10.1016/j.quascirev.2009.10.013